

**ISTANBUL TECHNICAL UNIVERSITY ★ GRADUATE SCHOOL OF SCIENCE**  
**ENGINEERING AND TECHNOLOGY**

**SYNTHESIS OF NANOCOMPOSITES THIN FILMS AND  
CHARACTERIZATION OF MECHANICAL PROPERTIES**

**M.Sc. THESIS**

**İsmail Hakkı Cengizhan KARBAY**

**Department of Nano Science & Nano Engineering**

**Nano Science & Nano Engineering Programme**

**MAY 2014**



**ISTANBUL TECHNICAL UNIVERSITY ★ GRADUATE SCHOOL OF SCIENCE**  
**ENGINEERING AND TECHNOLOGY**

**SYNTHESIS OF NANOCOMPOSITES THIN FILMS AND  
CHARACTERIZATION OF MECHANICAL PROPERTIES**

**M.Sc. THESIS**

**İsmail Hakkı Cengizhan KARBAY  
(513121002)**

**Department of Nano Science & Nano Engineering**

**Nano Science & Nano Engineering Programme**

**Thesis Advisor: Assoc. Prof. Dr. Esra Özkan ZAYİM**

**MAY 2014**



**İSTANBUL TEKNİK ÜNİVERSİTESİ ★ FEN BİLİMLERİ ENSTİTÜSÜ**

**NANOKOMPOZİT İNCE FİLMLERİN SENTEZİ  
VE MEKANİK ÖZELLİKLERİNİN KARAKTERİZASYONU**

**YÜKSEK LİSANS TEZİ**

**İsmail Hakkı Cengizhan KARBAY  
(513121002)**

**Nano Bilim ve Nano Mühendislik Anabilim Dalı**

**Nano Bilim ve Nano Mühendislik Programı**

**Tez Danışmanı: Doç. Dr. Esra Özkan ZAYİM**

**MAYIS 2014**



**İsmail Hakkı Cengizhan KARBAY**, a **M.Sc.** student of **ITU Graduate School of Science Engineering and Technology** student ID **513121002**, successfully defended the thesis entitled “**SYNTHESIS OF NANOCOMPOSITES THIN FILMS AND CHARACTERIZATION OF MECHANICAL PROPERTIES**”, which he prepared after fulfilling the requirements specified in the associated legislations, before the jury whose signatures are below.

**Thesis Advisor :**     **Assoc. Prof. Dr. Esra Özkan ZAYİM**     .....  
Istanbul Technical University

**Jury Members :**     **Assist. Dr. Mehmet Şeref SÖNMEZ**     .....  
Istanbul Technical University

**Prof. Dr. Deniz Değer ULUTAŞ**     .....  
Istanbul University

**Date of Submission :**    **5 May 2014**  
**Date of Defense**        **: 29 May 2014**





*To my family and professors,*



## **FOREWORD**

I would like to express my gratitude to my advisor, Assoc. Prof. Dr. Esra Özkan Zayim, whose expertise, understanding and patience, helped my work in this thesis.

My gratitude also goes to all members of research groups in the laboratory, for their personal, scientific and technical assistance during our work together.

I want to thank Dr. Refika Budakoğlu and all my other colleagues in Şişecam Company for their kind companionship and generous help.

This thesis research work would not have been possible without the financial assistance from Istanbul Technical University, as well as collaboration and help from a number of people who I did not mention by name. Herein, I would like to thank all of them.

May 2014

İsmail Hakkı Cengizhan KARBAY  
(Mechanical Engineer)



## TABLE OF CONTENTS

	<u>Page</u>
<b>FOREWORD.....</b>	<b>ix</b>
<b>TABLE OF CONTENTS.....</b>	<b>xi</b>
<b>ABBREVIATIONS .....</b>	<b>xiii</b>
<b>LIST OF TABLES .....</b>	<b>xv</b>
<b>LIST OF FIGURES .....</b>	<b>xvii</b>
<b>SUMMARY .....</b>	<b>xxi</b>
<b>ÖZET.....</b>	<b>xxiii</b>
<b>1. INTRODUCTION.....</b>	<b>1</b>
1.1. Microstructure .....	2
1.2. Thin Film Deposition .....	2
1.3. Sol-gel Process .....	4
1.3.1. Spin coating.....	7
1.3.2. Dip coating .....	8
1.4. Materials.....	8
1.4.1. $\text{TiO}_2 - \text{SiO}_2$ .....	9
1.4.2. $\text{Ta}_2\text{O}_5$ .....	11
1.4.3. Carbon nanotube .....	12
1.4.4. Cerium (IV) oxide nanoparticles.....	13
1.5. Measurement Systems.....	14
1.5.1. Mechanical tests .....	15
1.5.2. X-Ray diffractometer (XRD) .....	16
1.5.3. X-ray photoelectron spectroscopy (XPS).....	17
1.5.4. Scanning electron microscopy (SEM) .....	18
1.5.5. Ultraviolet-visible spectroscopy.....	18
1.5.6. NKD analyzer.....	19
1.5.7. Atomic force microscopy .....	19
1.5.8. Tensiometer.....	20
1.5.9. Finite element method.....	21
<b>2. MECHANICS OF MATERIALS, THIN FILMS AND SUBSTRATES ....</b>	<b>23</b>
2.2. Strain .....	24
2.3. Hooke's Law for Elastic Materials .....	25
2.4. Modulus of Elasticity (Young Modulus) .....	25
2.5. Poisson's Ratio.....	26
2.6. Mechanics of Nano Crystalline Materials.....	27
2.6.1. Density, pores and microcracks .....	27
2.7. Thin Films and Substrates Mechanics.....	27
2.7.1. Bending stresses .....	28
2.7.2. Curvature of radius.....	29
2.7.3. Curvature associated with a biaxial bending moment.....	29
2.7.4. Deflection associated with biaxial bending.....	30

2.7.5.	Thin Film Stresses .....	31
2.7.6.	Film stress - curvature relation .....	32
2.7.7.	Stresses in film and substrate (far from the edges of the film) .....	34
2.7.8.	Stress diagram .....	34
2.7.9.	Interfacial stresses .....	35
2.7.10.	Edge effects and interfacial shear stresses .....	37
2.7.11.	Theoretical analyses of multi layers with ring-on-ring test.....	40
<b>3.</b>	<b>THIN FILM OPTICS .....</b>	<b>47</b>
3.1.	Absorbing Mediums .....	47
3.2.	Transmittance and Reflectance in Permeable Medium.....	48
3.3.	Reflection at Surface of Absorbing Medium .....	52
3.4.	Transmittance and Reflectance of Single Layer .....	53
<b>4.</b>	<b>EXPERIMENTAL PROCEDURES.....</b>	<b>57</b>
4.1.	Cleaning Procedure of Glass Substrates.....	58
4.2.	Preparation of Sols .....	58
4.3.	Preparation of Films .....	60
<b>5.</b>	<b>RESULTS.....</b>	<b>61</b>
5.1.	Analytical Solution Results .....	61
5.2.	Finite Element Method (FEM) Results .....	63
5.3.	Experimental Results.....	67
5.4.	Optical Microscopy Results .....	70
5.5.	Scanning Electron Microscopy Results.....	71
5.6.	Atomic Force Microscopy Results .....	75
5.7.	Profilometer Results .....	77
5.8.	Tensiometer Results .....	78
5.9.	Ultraviolet-Visible Spectroscopy Results .....	79
5.10.	X-ray Photoelectron Spectroscopy Results .....	82
5.11.	X-ray Diffractometer Results .....	87
<b>6.</b>	<b>CONCLUSIONS .....</b>	<b>89</b>
	<b>REFERENCES .....</b>	<b>93</b>
	<b>CURRICULUM VITAE .....</b>	<b>99</b>

## **ABBREVIATIONS**

<b>AFM</b>	: Atomic Force Microscopy
<b>FEM</b>	: Finite Element Method
<b>PVB</b>	: Polyvinyl butyral
<b>SEM</b>	: Scanning Electron Microscope
<b>SWCNT</b>	: Single-walled Carbon Nanotube
<b>UV-vis</b>	: Ultraviolet visible spectroscopy
<b>XPS</b>	: X-Ray Photoelectron Spectroscopy
<b>XRD</b>	: X-Ray Diffraction





## LIST OF TABLES

	<u>Page</u>
<b>Table 1.1:</b> Mechanical properties of SiO <sub>2</sub> .....	10
<b>Table 1.2:</b> Mechanical properties of TiO <sub>2</sub> .....	11
<b>Table 1.3:</b> Mechanical properties of Ta <sub>2</sub> O <sub>5</sub> .....	12
<b>Table 1.4:</b> Mechanical Properties of SWCNTs .....	13
<b>Table 1.5:</b> Mechanical properties of CeO <sub>2</sub> .....	14
<b>Table 5.1:</b> Mechanical property of various oxide films and glass substrate. ....	61
<b>Table 5.2:</b> Interaction between P and $\sigma$ .....	62
<b>Table 5.3:</b> Ultimate forces for various materials .....	63
<b>Table 5.4:</b> FEM results of the samples .....	63
<b>Table 5.5:</b> Experimental results obtained from ring-on-ring and scratch tests. ....	68
<b>Table 5.6:</b> Comparing experimental and FEM results. ....	70
<b>Table 5.7:</b> AFM results of Ta <sub>2</sub> O <sub>5</sub> thin film. ....	76
<b>Table 5.8:</b> AFM results of TiO <sub>2</sub> - SiO <sub>2</sub> film .....	76
<b>Table 5.9:</b> Contact angle for different coatings .....	78
<b>Table 5.10:</b> Detailed XPS spectra of calcined TiO <sub>2</sub> - SiO <sub>2</sub> film at 450 °C .....	85
<b>Table 5.11:</b> Detailed XPS spectra of calcined Ta <sub>2</sub> O <sub>5</sub> film at 450 °C. ....	87



## LIST OF FIGURES

	<u>Page</u>
<b>Figure 1.1:</b> Simple schematic view of a thin film. ....	1
<b>Figure 1.2:</b> The growth model of the thin films. ....	3
<b>Figure 1.3:</b> Typical thin film deposition system in vacuum. ....	3
<b>Figure 1.4:</b> Typical deposition methods of thin films. ....	4
<b>Figure 1.5:</b> Sol-gel technology scheme. ....	5
<b>Figure 1.6:</b> Spin coating process ....	7
<b>Figure 1.7:</b> Schematic view of dip coating process. ....	8
<b>Figure 1.8:</b> Pure silicon dioxide. ....	9
<b>Figure 1.9:</b> Pure titanium dioxide. ....	10
<b>Figure 1.10:</b> Pure tantalum pentoxide. ....	11
<b>Figure 1.11:</b> Carbon nanotube types ....	13
<b>Figure 1.12:</b> Pure CeO <sub>2</sub> . ....	14
<b>Figure 1.13:</b> Application of ring-on-ring test to different glasses. ....	15
<b>Figure 1.14:</b> XRD working scheme. ....	16
<b>Figure 1.15:</b> XPS working scheme. ....	17
<b>Figure 1.16:</b> Working scheme of SEM. ....	18
<b>Figure 1.17:</b> UV-vis working scheme. ....	19
<b>Figure 1.18:</b> Schematic view of AFM. ....	20
<b>Figure 1.19:</b> Wetting types and contact angle. ....	20
<b>Figure 2.1:</b> (a) Object under tension, (b) object under compression. ....	23
<b>Figure 2.2:</b> Strain types for different directions. ....	24
<b>Figure 2.3:</b> Stress - strain curves. ....	26
<b>Figure 2.4:</b> Biaxial bending of a thin plate. ....	28
<b>Figure 2.5:</b> Bending moments and stress distribution. ....	28
<b>Figure 2.6:</b> Plate deflection. ....	30
<b>Figure 2.7:</b> Thin film on a substrate. ....	31
<b>Figure 2.8:</b> The film and substrate in a stress free state. ....	32
<b>Figure 2.9:</b> Stretching the film. ....	32
<b>Figure 2.10:</b> Substrate forces. ....	32
<b>Figure 2.11:</b> Film forces. ....	33
<b>Figure 2.12:</b> Substrate forces. ....	33
<b>Figure 2.13:</b> Moment effect due to external forces. ....	33
<b>Figure 2.14:</b> Calculation of stresses. ....	34
<b>Figure 2.15:</b> Stresses in film and substrate. ....	35
<b>Figure 2.16:</b> Stresses in film and substrate. ....	35
<b>Figure 2.17:</b> Force balance. ....	36
<b>Figure 2.18:</b> Misfit strain. ....	37
<b>Figure 2.19:</b> Film with external loading. ....	37
<b>Figure 2.20:</b> External edge loading. ....	37
<b>Figure 2.21:</b> Removal of edge forces. ....	38
<b>Figure 2.22:</b> Interfacial stress distribution. ....	38
<b>Figure 2.23:</b> Shear stress distribution for a rigid substrate. ....	39

<b>Figure 2.24:</b> Shear stress distribution for a compliant substrate. ....	40
<b>Figure 2.25:</b> Schematic of an axial symmetry of a thin elastic multilayered disc. ...	41
<b>Figure 2.26:</b> Schematic view of multilayered discs subjected to ring-on-ring test. ..	43
<b>Figure 2.27:</b> Schematic drawing on top view of ring-on-ring test. ....	44
<b>Figure 3.1:</b> Incident, transmitted and reflected wave. ....	49
<b>Figure 3.2:</b> Reflectivity values. ....	50
<b>Figure 3.3:</b> Light waves reflected and transmitted. ....	53
<b>Figure 4.1:</b> Uncoated glass substrates for the mechanical tests. ....	57
<b>Figure 4.2:</b> Ta <sub>2</sub> O <sub>5</sub> thin film coated Corning glass 2947 .....	57
<b>Figure 4.3:</b> Preparation of traditional TiO <sub>2</sub> sol.....	58
<b>Figure 4.4:</b> Preparation of SiO <sub>2</sub> sol. ....	59
<b>Figure 4.5:</b> Preparation of Ta <sub>2</sub> O <sub>5</sub> sol. ....	60
<b>Figure 5.1:</b> Stress distribution of glass substrate.....	64
<b>Figure 5.2:</b> Deflection of glass substrate.....	64
<b>Figure 5.3:</b> Stress distribution of TiO <sub>2</sub> - SiO <sub>2</sub> coated glass substrate.....	65
<b>Figure 5.4:</b> Deflection of TiO <sub>2</sub> - SiO <sub>2</sub> coated glass substrate.....	65
<b>Figure 5.5:</b> Stress distribution of Ta <sub>2</sub> O <sub>5</sub> coated glass substrate. ....	66
<b>Figure 5.6:</b> Deflection of Ta <sub>2</sub> O <sub>5</sub> coated glass substrate.....	66
<b>Figure 5.7:</b> Broken glasses with different coatings, three different failure types. ....	67
<b>Figure 5.8:</b> Comparison for ultimate strength. ....	69
<b>Figure 5.9:</b> Comparison for scratch resistance. ....	69
<b>Figure 5.10:</b> Microscopy image of TiO <sub>2</sub> - SiO <sub>2</sub> film with different magnification...	70
<b>Figure 5.11:</b> Optical microscopy image of Ta <sub>2</sub> O <sub>5</sub> thin film. ....	71
<b>Figure 5.12:</b> Microscopy image of TiO <sub>2</sub> - SiO <sub>2</sub> with CeO <sub>2</sub> nanoparticles. ....	71
<b>Figure 5.13:</b> SEM image of Ta <sub>2</sub> O <sub>5</sub> thin film (50X).....	72
<b>Figure 5.14:</b> SEM image of Ta <sub>2</sub> O <sub>5</sub> thin film (50X).....	72
<b>Figure 5.15:</b> SEM image of Ta <sub>2</sub> O <sub>5</sub> thin film (90X).....	73
<b>Figure 5.16:</b> SEM image of TiO <sub>2</sub> - SiO <sub>2</sub> film (20X). ....	73
<b>Figure 5.17:</b> SEM image of TiO <sub>2</sub> - SiO <sub>2</sub> film (50X). ....	74
<b>Figure 5.18:</b> SEM image of SWCNT (less) reinforced TiO <sub>2</sub> - SiO <sub>2</sub> . ....	74
<b>Figure 5.19:</b> SEM image of SWCNT (more) reinforced TiO <sub>2</sub> - SiO <sub>2</sub> . ....	75
<b>Figure 5.20:</b> AFM image of Ta <sub>2</sub> O <sub>5</sub> thin film.....	75
<b>Figure 5.21:</b> AFM images of TiO <sub>2</sub> - SiO <sub>2</sub> film.....	76
<b>Figure 5.22:</b> Profilometer result image of Ta <sub>2</sub> O <sub>5</sub> thin film. ....	77
<b>Figure 5.23:</b> Profilometer result image of TiO <sub>2</sub> - SiO <sub>2</sub> film.....	77
<b>Figure 5.24:</b> Tensiometer pictures of different coatings. ....	78
<b>Figure 5.25:</b> Transmittance for different coatings with respect to wavelength.....	79
<b>Figure 5.26:</b> Transmittance for different coatings with respect to energy. ....	79
<b>Figure 5.27:</b> First derivation of transmittance with respect to photon energy. ....	80
<b>Figure 5.28:</b> Transmittance of deposited films with respect to wavelength .....	81
<b>Figure 5.29:</b> Transmittance of deposited films with respect to wavelength .....	81
<b>Figure 5.30:</b> Reflectance of deposited films with respect to wavelength. ....	82
<b>Figure 5.31:</b> Reflectance of deposited films with respect to wavelength. ....	82
<b>Figure 5.32:</b> XPS survey scan spectra of calcined TiO <sub>2</sub> - SiO <sub>2</sub> film at 450 °C.....	83
<b>Figure 5.33:</b> XPS Si2p scan spectra of calcined TiO <sub>2</sub> - SiO <sub>2</sub> film at 450 °C. ....	83
<b>Figure 5.34:</b> XPS C1s scan spectra of calcined TiO <sub>2</sub> - SiO <sub>2</sub> film at 450 °C. ....	84
<b>Figure 5.35:</b> XPS Ti2p scan spectra of calcined TiO <sub>2</sub> - SiO <sub>2</sub> film at 450 °C.....	84
<b>Figure 5.36:</b> XPS O1s scan spectra of calcined TiO <sub>2</sub> - SiO <sub>2</sub> film at 450 °C. ....	85
<b>Figure 5.37:</b> XPS survey scan spectra of calcined Ta <sub>2</sub> O <sub>5</sub> film at 450 °C.....	85
<b>Figure 5.38:</b> XPS Ta4f scan spectra of calcined Ta <sub>2</sub> O <sub>5</sub> film at 450 °C.....	86

<b>Figure 5.39:</b> XPS O1s scan spectra of calcined Ta <sub>2</sub> O <sub>5</sub> film at 450 °C.....	86
<b>Figure 5.40:</b> XPS C1s scan spectra of calcined Ta <sub>2</sub> O <sub>5</sub> film at 450 °C.....	87
<b>Figure 5.41:</b> XRD pattern of Ta <sub>2</sub> O <sub>5</sub> film on glass substrate.....	88
<b>Figure 5.42:</b> XRD pattern of TiO <sub>2</sub> – SiO <sub>2</sub> film on glass substrate.....	88



## **SYNTHESIS OF NANOCOMPOSITES THIN FILMS AND CHARACTERIZATION OF MECHANICAL**

### **SUMMARY**

Thin film technology has been studied extensively because of its ease of use. Moreover, it is inexpensive way to synthesis composites materials. It consumes less material, thus it is more environmental solution for fabrication of advanced materials.

Mechanical strength is quite important feature for any material and any application area. Mechanical properties affect all design parameters. Therefore, it is important to know or predict behavior of materials before using them in our system.

Ultimate strength, wear resistance and chemical resistance are some features that can be improved via thin film technology. Also the optical properties such as transmittance, reflectance can be altered.

In principle, both inorganic and organic materials can be coated on different substrates. Toxicity is the biggest problem for various usages. Tantalum, titanium and their oxide forms are quite popular materials because of their compatibility with human body. The main reason is the chemical inertness of these materials. Titanium is used in surgeries since 1950s and it is not affected by body fluids. Besides, it withstands external forces very well.

Tantalum and tantalum oxide are well known as their great chemical stability and high refractive index but theirs superior mechanical properties have not drawn so much attention. Moreover, it is extremely transparent that is a necessary feature when working with glass. These incredible features make tantalum oxide a perfect coating material for glass substrates.

Improving mechanical strength of glass has been worked for many years. Many scientists have tried reinforcing glass with both inorganic and organic materials. Polyvinyl butyral (PVB) is the most popular organic material for both ultimate strength and toughness. Additionally, it holds glass particles together that provides extra safety. Thus, PVB is often used in many applications such as cars, buildings and household goods. However, the negative effects (degradation, etc.) of sunshine on organic materials are well known in the literature. Therefore, PVB may not be the best selection for materials in touch with human body like glasses, plates, etc. Inorganic materials are generally more stable in the rough environmental conditions. In this work, we tried to improve the mechanical properties of glass with inorganic materials.

All these properties mentioned above depend on the deposition techniques. Coating techniques should be cheap and compatible with batch processes. Sol-gel process offers an efficient platform to scientists to coat the glass, because of numerous reasons: it requires relatively simpler laboratory equipment and offers a large portfolio of starting materials and lastly. Moreover, it allows modification of

surfaces quite effortlessly. With the use of this process, the preparation of binary and ternary inorganic materials and nanostructures have been studied considerably to date. In this work, dip and spin coating were separately used to deposit the glass substrates and the results were compared. Mechanical properties change with different coating methods because it affects final film thickness directly. Firstly, the binary and ternary films were deposited by spin and dip coatings. Subsequently, detailed characterization of the films and the properties - especially the mechanical properties - of the sol-gel derived films are discussed aiming to improve mechanical properties with great potential in the glass technology.

There are huge number of organic and inorganic materials. The mechanical and optical properties are changed in nano scale and composite materials. Therefore, it is nearly impossible to try out every material with each other in nano or macro scales. Sometimes we need the analytical calculation and/or computer simulations to analyze final behavior. Both of them need the properties of materials and boundary conditions for given situations. Finite element method (FEM) is very popular and quite successful for many different analyze types. It gives quick information about our system. Using these kinds of computer programs (which use FEM) help us to select the right materials for our purpose and design our systems.

In this work, we used titanium dioxide ( $\text{TiO}_2$ ) – silicon dioxide ( $\text{SiO}_2$ ) binary system and tantalum pentoxide ( $\text{Ta}_2\text{O}_5$ ) as coating materials with different additives. Two different titanium dioxide – silicon dioxide recipes were used. As additive agent single-walled carbon nanotubes (SWCNTs) and cerium dioxide ( $\text{CeO}_2$ ) nano particles were used. For phase characterization and chemical composition of the samples, X-ray diffractometry (XRD) and X-ray photoelectron spectroscopy (XPS) were used, respectively. Scanning electron microscope (SEM), atomic force microscopy (AFM) and optical microscopy were used for examining film surfaces. UV-visible spectroscopy and NKD analyzer were used to measure transmittance and reflectance of samples. Contact angle was measured by tensiometer.

Ring-on-ring tests were used as main mechanical test. It is a biaxial test, which gives better results for the brittle materials. The second mechanical test was scratch test. It gives information about surface hardness directly and wear resistance indirectly. Finally, all results of the deposited films were compared to each other.

$\text{Ta}_2\text{O}_5$  thin films represent the best results. They demonstrated around 200% improvement for ultimate strength and huge increase in scratch resistance. Adding  $\text{CeO}_2$  nano particles to  $\text{TiO}_2$  –  $\text{SiO}_2$  binary sol gave poor results in terms of the mechanical properties. SWCNT shows some improvement especially on hardness. Very small amount of SWCNT leads 7% improvement on ultimate strength and 100% on hardness. Nevertheless, the positive effects of SWCNT decreases by increasing content. FEM gave nearly perfect results for all samples. It is obvious that, Ansys could easily apply to analyze bilayer or multilayer materials.



## **NANOKOMPOZİT İNCE FİMLERİN SENTEZİ VE MEKANİK ÖZELLİKLERİNİN KARAKTERİZASYONU**

### **ÖZET**

İnce film teknolojisi, kolay uygulanmasından ötürü son zamanlarda giderek yaygınlaşmıştır. Ayrıca tüm yapıyı kompozit üretmekten daha ucuza mal olmaktadır. Daha az malzeme tüketimi olduğundan, yüksek teknolojik malzemelerin üretiminde daha çevreci çözümler sunar.

Mukavemet, her malzeme için, tüm kullanım alanlarında en önemli özelliklerden biridir. Mekanik özellikler tüm tasarım parametrelerini etkiler. Bu sebeple sistemimizde kullanmadan önce malzemelerin davranışlarını bilmek ya da tahmin etmek çok önemlidir.

Kopma dayanımı, aşınma dayanımı ve kimyasallara karşı direnç gibi özellikler ince film teknolojisi ile geliştirilebileceği gibi geçirgenlik ve yansıtıcılık gibi optik özellikler de değiştirilebilir.

Prensipte hem inorganik hem de organik malzemeler farklı altlıklara kaplanabilir. Birçok kullanım alanı için zehirlilik en büyük problemlerden biridir. Tantalum, titanyum ve oksitleri insan vücuduyla uyumlu olmalarından dolayı son derece yaygın kullanımı olan malzemelerdir. En büyük sebep bu malzemelerin kimyasal olarak tepkime vermemesidir. Titanyum 1950'lerden beri ameliyatlarda kullanılır ve vücut sıvıları ile tepkimeye girmez. Bununla beraber dış kuvvetlere karşı gayet iyi dayanır.

Tantalum ve oksidi müthiş kimyasal kararlılığı ve yüksek yansıtıcılık özellikleri iyi bilinse de mükemmel mekanik özellikleri bu zaman kadar fazla dikkat çekmemiştir. Buna ilaveten tantalum filmler son derece transparandır ve bu camlar ile çalışmak için son derece önemli bir parametredir. Bu inanılmaz özellikler tantulumu cam altlıklar için mükemmel bir kaplama malzemesi yapar.

Camın mekanik özelliklerini iyileştirmek için uzun yılladır çalışılmıştır. Birçok bilim adamı camı hem inorganik hem de organik malzeme ile takviye etmeyi denemiştir. Polyvinyl butyral (PVB) hem kopma mukavemeti hem de tokluk açısından en yaygın olarak kullanılan organik takviye malzemesidir. Aynı zamanda kırılma durumlarında, cam parçalarını bir arada tutarak daha yüksek güvenlik sunar. Bu özelliklerinden dolayı PVB, araba camları ve inşaat sektörü gibi birçok kullanım alanına sahiptir. Lakin, güneş ışığının organik malzemeler üzerindeki negatif etkileri (degradasyon, vb.) bilinmektedir. Bu nedenle PVB bardak, tabak gibi insan ile temasta bulunan malzemelerde en iyi seçim olmayabilir. Genel olarak inorganik malzemeler zorlu çevre koşullarına karşı daha dayanıklıdır. Bu sebeplerden ötürü camın mekanik özellikleri inorganik malzemeler ve katkı maddeleri ile iyileştirilmeye çalışılmıştır.

Yukarıda belirtilen bütün özellikler üretim metoduyla bağlantılıdır. Yöntem ucuz ve seri üretime elverişli olmalıdır. Birçok farklı özellik sunmasıyla beraber göreceli olarak küçük bir laboratuvar ekipmanı olan, sol-gel metodu, bilim insanlarına, cam kaplama için etkili bir yöntem sunmaktadır. Ayrıca yüzey özellikleriyle kolayca

oyunabilmektedir. İkili, üçlü inorganik ve nano yapıli malzemelerin sentezi, bu yöntemin kullanılmasıyla günümüze kadar gelmiştir. Bu çalışmada, döndürerek ve daldırarak kaplama yöntemleri ayrı ayrı kullanılarak cam altlıklar kaplanmış ve sonuçlar incelenmiştir. Mekanik özellikler kaplama yöntemine bağılı olarak değışir, çünkü yöntem film kalınlığını doğrudan etkiler. İlk olarak, ikili ve üçlü sistemdeki filmler döndürerek ve daldırarak kaplama metotlarıyla kaplanmışır. Daha sonra, mekanik özellikler başta olmak üzere, filmlerin detaylı karakterizasyonu yapılmıştır. Sol-gel yöntemiyle elde edilen filmlerde, gelişmeye açık olan camların mekanik özelliklerini iyileştirmek amaçlanmıştır.

Dünyada binlerce farklı organik ve inorganik malzeme vardır. Kompozit teknolojisinde ise iki veya daha fazla malzeme bir arada kullanılır. Buna ek olarak mekanik ve optik özellikler nano boyutta tamamen değışir. Yani her bir malzemeyi, birbiriyle nano veya makro boyutta denemek neredeyse imkânsızdır. Bazen analitik çözümler ve/veya bilgisayar simülasyonları bitmiş yapının davranışlarını analiz etmek için gereklidir. İki yöntemde malzemenin mekanik özelliklerine ve verilen problem için sınır koşullarına ihtiyaç duyar. Sonlu elemanlar yöntemi son derece yaygındır ve farklı analiz tipleri için oldukça başarılı sonuçlar vermektedir. Bu çeşit bilgisayar programları doğru malzemeyi seçmemizde ve sistemimizi tasarlamamızda bize yardım eder.

Bu çalışmada titanyum dioksit ( $\text{TiO}_2$ ) – silisyum dioksit ( $\text{SiO}_2$ ) karışımı ve tantalum pentoksit ( $\text{Ta}_2\text{O}_5$ ) farklı katkı maddeleri ile kaplama malzemesi olarak kullanılmışır. İki farklı  $\text{TiO}_2$  –  $\text{SiO}_2$  reçetesi denenmiştir. Katkı malzemesi olarak da tek duvarlı karbon nanotüp (SWCNTs) ve ceryum dioksit ( $\text{CeO}_2$ ) nano parçacıklar kullanılmışır.

Örneklerin faz karakterizasyonu için, x-ışını spektroskopisi (XRD) ve x-ışını fotoelektron spektroskopisi kullanılmışır. Film yüzeylerinin incelenmesi için ise taramalı elektron mikroskopundan (SEM), atomik kuvvet mikroskopu (AFM) ve optik mikroskoptan yararlanılmışır. UV-görünür bölge spektroskopisi ve NKD analizör ile örneklerin optik geçirgenlik ve yansıtıcılık özelliklerini saptamak için kullanılmışır. Suyun kontak açısı, tensiyometre ile ölçülerek, yüzeylerin hidrofilitiklik ve hidrofobiklik özellikleri incelenmiştir.

Halka üzerinde halka testi asıl olan mekanik testtir. Bu test gevrek malzemeler için daha iyi sonuç veren, çift eksenli gerilme uygulayan bir yöntemdir. Numuneler iki farklı çaptaki halka arasına konarak, kırılınca kadar basma gerilmesi uygulanır. Camlar gevrek yapıda olduklarından akma gerilmesi, maksimum çekme gerilmesi ve kopma gerilmesi deęerlerinin hepsi birbirine yakındır. Cihaz gerilme ve sehim deęerlerini kaydeder. Böylece kaplanan farklı filmlerin, mekanik özelliklere olan etkisi güvenilir biçimde ölçülmüş olunur. Gevrek malzemelerde testin tekrarı, güvenilirlik için son derece önemlidir.

Uygulanan ikinci test ise çizilme testidir. Bu yöntem yüzey sertlięi ile ilgili direkt; aşınma direnci ile ilgili dolaylı yönden bilgi verir. Aynı zamanda sertlik ile akma dayanımı arasında da bir bağıntı vardır. Son olarak, tüm sonuçlar birbiri ile karşılaştırılmışır.

Tantalum pentoksit, optik ve yarı-iletken uygulamalarında yaygın olarak kullanılan bir malzemedir. Ancak yapılan testlerde, aynı zamanda mekanik özellikleri oldukça iyileştirdięi gözlemlenmiştir. Kopma mukavemetini yaklaşık olarak 3.5 katına çıkarmıştır. Mekanik özelliklerdeki bu iyileşmenin yanı sıra, transparan camın optik özelliklerini de bozmamıştır. Aynı zamanda insan sağığına olumsuz etkileri de

olmaması sebebiyle, tantalum pentoksit, mukavemet gerektiren birçok alanda kullanılabilir. Aynı zamanda kaplanan film oldukça incedir. Böylece malzeme verimli bir şekilde kullanılabilir.

Üçlü sol sistemi denemesi ise, başarısız olmuştur. Sebebi hatalı kimyasal reaksiyonlar olabilir. Solleri karıştırmak yerine tabakalı film uygulaması mekanik açıdan daha iyi sonuç verebilir. Öte yandan, titanyum ve silisyum oksit ikili sistemi de gerek mekanik gerek optik açıdan iyi sonuçlar vermiştir. Optik geçirgenlik özelliği, tantalum filmlerden yaklaşık olarak 20 kat daha kalın olmasına rağmen, daha iyidir. Aynı zamanda daha sünek ve tok bir film oluşturarak, darbe direncinin de artmasına yardımcı olur. Lakin, kalın film seri üretim söz konusu olduğunda, maliyet açısından olumsuz olabilir.

Mekanik özellikler bakımından, bilinen en iyi malzeme olan tek duvarlı karbon nanotüp katkısı ise beklenen etkiyi verememiştir. Sebebi sol içinde çözülme ve düzgün dağılmama sorunlarıdır. İlerleyen teknoloji seviyesi ile bu malzemenin istenildiği gibi kullanılmasına olanak sağlanacaktır.

Analitik çözüm, tek tabaka için oldukça başarılı sonuçlar verse de çok katmanlı yapılarda hassasiyetini kaybetmektedir. Sonlu elemanlar yöntemi ise, çok katmanlı yapıları da oldukça hassas şekilde analiz edebilmiştir ve ince film araştırma ve geliştirme çalışmalarında yaygın olarak kullanılması gerektiğini göstermiştir. Hata payı %10'un altındadır.



## 1. INTRODUCTION

A thin film is a layer of material ranging from fractions of a nanometer (monolayer) to several micrometers in thickness [1]. Electronic semiconductor devices and optical coatings are the main applications benefiting from thin-film construction.

Thin film materials have become technologically important recently, some examples are:

- Microelectronic Integrated Circuits
- Magnetic Information Storage Systems
- Optical Coatings
- Wear Resistant Coatings
- Corrosion Resistant Coatings.

Ability to make small-scale devices (magnetic storage), physical properties those are scale-dependent (optical filters), cost benefits (use small amounts of expensive materials for coatings) are the main points for using materials in thin film form [2-10].

Generally, we think thin films based devices in terms of their electronic, magnetic or optical properties, however in many applications mechanical properties can be improved significantly with thin film technology.

We named them thin because, the thicknesses of these substrates are usually much smaller than their lateral dimensions. In addition, deposited film thickness is generally much thinner than the thickness of the substrate. Figure 1.1 shows schematic view of a thin film and the substrate.

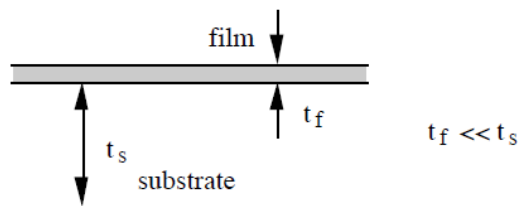


**Figure 1.1:** Simple schematic view of a thin film.

In the following section, a general introduction to applicable fabrication techniques of thin layers will be provided (see, 1.2). The materials used for this aim are introduced (see, 1.4). Measurement techniques related to thin films - that are utilized in this work - are listed (see, 1.5). After that, mechanics of materials, thin films and substrates are described in detail (see, 2) and optics of thin films are described (see, 3).

### 1.1. Microstructure

*Grain size =  $d$ ,*

*Dislocation spacing =  $1/\sqrt{\rho}$*

Film thickness is always comparable to microstructural dimension.

$t_f \approx d$ ,

$t_f \approx 1/\sqrt{\rho}$

The main purpose is getting finer microstructure than in bulk form. This causes mechanical properties of thin films to be different from those of bulk materials [10].

### 1.2. Thin Film Deposition

Thin films are grown by the deposition of material atoms on any substrate. The thin film growth exhibits the following features:

- The birth of thin films of all materials starts with a random nucleation process followed by nucleation and growth stages.
- The nucleation and growth stages are dependent upon various deposition conditions, such as growth temperature, growth rate, and substrate surface chemistry.
- The nucleation stage can be modified by external agencies, such as electron or ion bombardments.
- Film microstructure that is associated defect structure, and film stress depend on the deposition condition of the nuclear stage.
- Crystal phase and crystal orientation of the thin films are governed by the deposition conditions [11].

Figure 1.2 shows the growth mechanism for thin films.

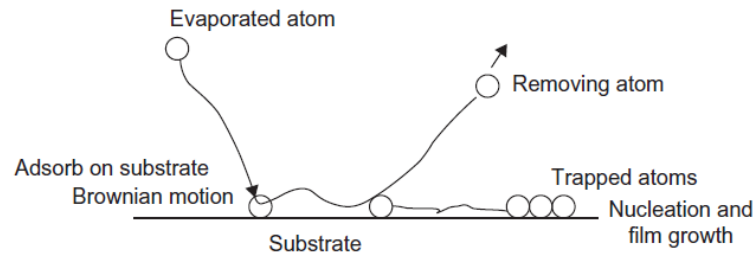


**Figure 1.2:** The growth model of the thin films.

By controlling deposition conditions, basic properties of thin films can be altered such as film chemical composition, structural properties, and film thickness. Thin films show very different characteristic properties than bulk materials:

- Unique material properties depend on the atomic growth process on the growing substrate.
- By including quantum size effects, size effects characterized by crystal orientation, thickness and multilayer aspects [11].

Generally, bulk materials are sintered from the powder of source material. Diameter of the powder is of the order of 1  $\mu\text{m}$ . On the other hand, thin films are synthesized from ultrafine particles like atoms or a cluster of atoms. Figure 1.3 shows thin film deposition process in vacuum.

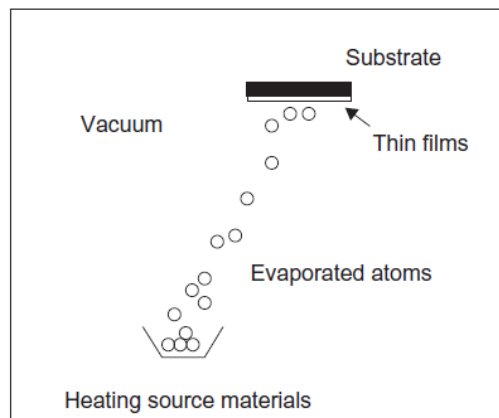


**Figure 1.3:** Typical thin film deposition system in vacuum.

There are two main categories for deposition process, physical and chemical. Figure 1.4 shows thin deposition techniques.

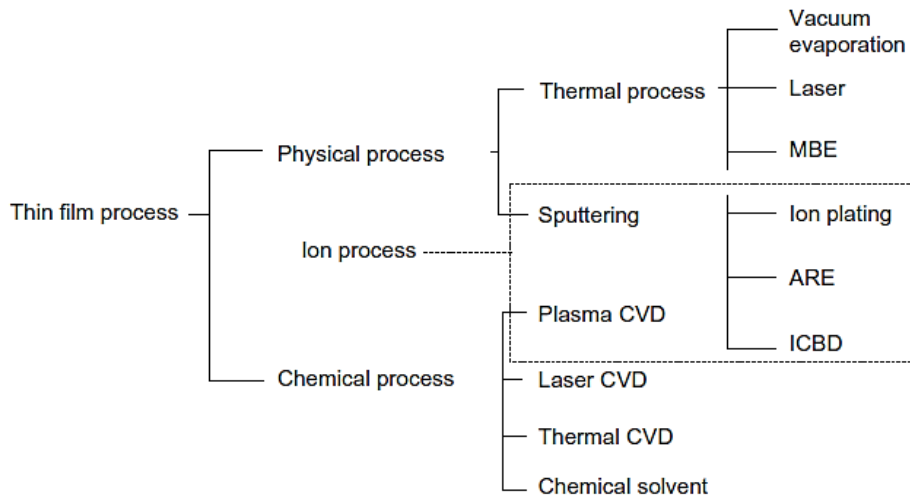


**Figure 1.4:** Typical deposition methods of thin films.

Plating, chemical solution deposition, spin coating, dip coating, spray-up, chemical vapor deposition and atomic layer deposition are chemical deposition techniques.

On the other hand, physical vapor deposition, sputtering, pulsed laser deposition, cathodic arc deposition and electro hydrodynamic deposition are physical techniques for deposition technology.

### 1.3. Sol-gel Process

Sol-gel process is used for production of solid materials from small molecules. Oxides of silicon and titanium are the most popular materials for this process. The process involves conversion of monomers into a colloidal solution (sol) that acts as the precursor for an integrated network (or gel) of either discrete particles or network polymers [12].

Materials prepared by sol-gel technology can range from relatively simple inorganic glasses to more complex hybrid composites [13]. By using composite thin films, advantages of both materials can be gained. Because of unique properties of sol-gel process, it has gained particular attention. Molecular scale homogeneity, low cost and easy control parameters are some advantages of sol-gel process. In addition, thin films that made by sol-gel process, shows excellent antiwear and friction reduction performances and low loads [14-16]. Figure 1.5 shows sol-gel technology scheme.



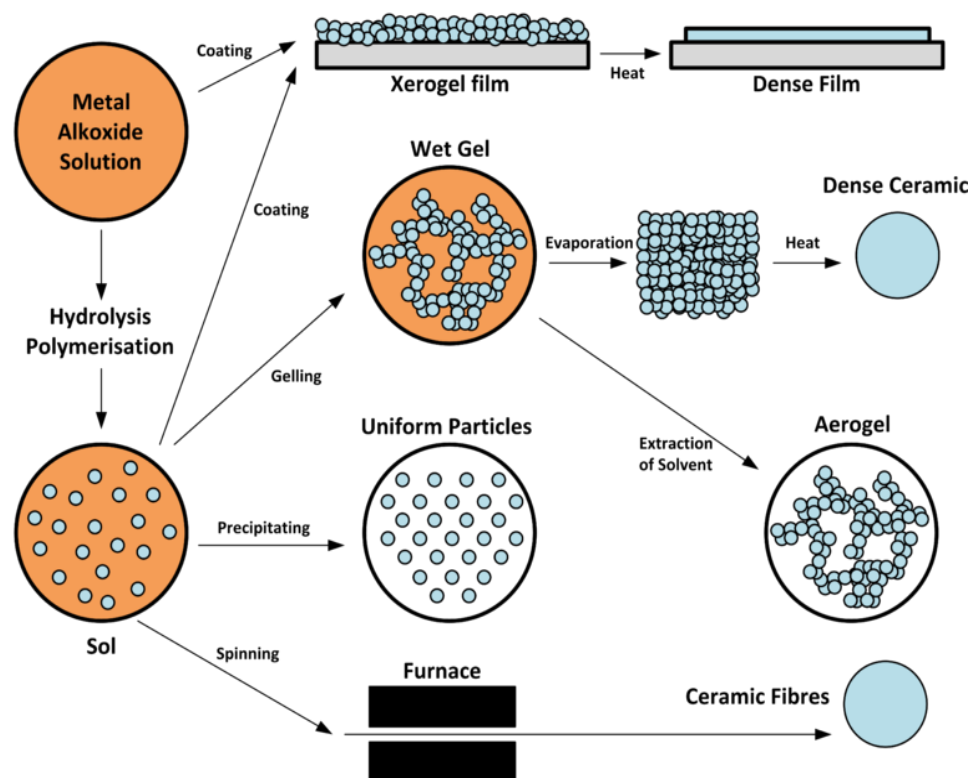


**Figure 1.5:** Sol-gel technology scheme.

Two of the most common ways used in analytical applications are monolithic gels and thin films. Monolithic gels can be easily prepared by pouring sol into appropriate container. After gelation and drying, the monolithic piece is shaped by the container in which it was poured [17]. Thin films can be prepared by spin coating, dip coating and spray-up techniques.

The chemical reactions that occur during the formation of the sol, gel, and xerogel strongly influence the composition and properties of the final product [18]. The hydrolysis and condensation process of sol material should be known well. Rate of aging and drying, temperature, added dopants, the type and concentration of co-solvents, the type and concentration of catalyst and pH are known as factors that influence hydrolysis [19].

The viscosity of the sol increases until a specific point as hydrolysis and condensation proceed, the solution ceases the flow and gelation has occurred. At this point whole mass has become interconnected with a liquid phase trapped within [20]. It is very important to know that, in contrast to many polymeric reactions, the sol-gel transition is irreversible. As the gel sits in its pore liquid, the structure of the gel continues to change via additional condensation reactions between neighboring

unreacted groups. As the gel ages, the connectivity of the network increases, the pore size decreases, and solvent is expelled from the pores. Temperature, time and pH affect the aging process and thus the final structure of the gel [21].

Solvent (i.e., alcohol) and water evaporate from the pores leading the solid matrix to shrink and pores to collapse during drying process. Xerogels, or fully dried gels, have final volumes that are approximately 1/8 their original volume and are considerably less porous than their "wet" counterpart. During drying, internal pressures can be built up in the gel due to surface tension forces that generates stress cracks and fractures to occur [21]. These cracks can be eliminated by drying monolithic gel slowly, in high humidity environment or by producing thin films [22].

The structure of the thin films can be very different from the structure of monolith, which prepared from the same sol because gelation and aging occur simultaneously with drying. In contrast, the aging and drying process in monolithic gels typically occurs over a period of several days to several weeks. As a result, thin films are often considerably denser and less porous than corresponding monolithic materials [23].

Materials that produced via sol-gel method have found various applications in the area of chemistry, biochemistry, engineering and materials science [24]. This particular attention comes from easy preparation and modification parameters of sol-gel technology. For example, the silicate glasses can be formed in different forms (thin films, monoliths, powders, fibers) and sizes, different physical and chemical properties (pore size, shape, distribution, surface area, refractive index, polarity). In addition, they can be readily doped with various polymers for any application [25].

These are the main usage area of materials that produced by sol-gel method:

- Chemical sensors (pH sensors, sensors for ions and neutral species, sensors for gases and vapors, biosensors)
- Chromatography
- Fabrication of selective materials
- Optical applications (nonlinear optical materials, optical waveguides, solid-state lasers, electroluminescent devices) [13].

### 1.3.1. Spin coating

It is the simplest method for fabricating a film on a substrate. Spin coating is a very practical way to deposit uniform thin films to flat substrate. The substrate is rotated at high speed in order to spread coating material by centrifugal force. The higher the angular speed of substrate, the thinner the film. The final thickness also depends on the concentration, surface tension and viscosity of the coating material. Even thicknesses below 15 nm films can be produced by this method [26]. Figure 1.6 shows the steps of spin coating process.

Thin resist layers for photolithography are coated with this technique. Some of the solvent is removed during spinning process due to evaporation and some by baking at elevated temperatures. This technique is often used for planarization purposes because it results relatively planar surfaces [27]. The advantages of spin coating:

- Fast process time and cost effective
- Highly uniform surfaces even curved parts can be achieved
- Lenses with different curvatures might be coated uniformly with minimal thickness edge effects or variation.
- Sol is used once for each coating so avoiding contamination is easier then dip coating.
- Fewer amounts of sol is needed for experimental use, also it is better for expensive materials [28].

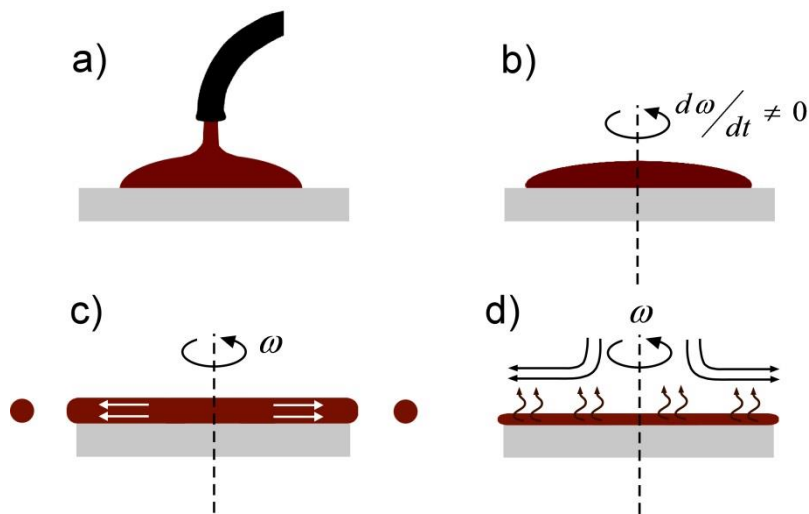


**Figure 1.6:** Spin coating process. a) Acceleration b) Dispensation c) Flow dominated d) Evaporation dominated.

### 1.3.2. Dip coating

In this method, the substrate is normally withdrawn vertically from a desired coating solution, which causes a complex process involving gravitational draining with concurrent drying and continued condensation reactions. Environmental conditions (temperature, humidity, airflow) are very important parameters as much as withdrawn speed. They all affect film parameters. The formation of thin films occurs through solvents evaporation (mainly ethanol and water), which concentrates nonvolatile species in the system, then leading to aggregation and gelation. The resulting film depends on these parameters:

- Withdrawal speed
- Capillary pressure
- Size and structure of precursors
- Condensation and evaporation rates
- Substrate surface [29]

It is the oldest and the most widely used deposition technique in industry because its ease of use, high coating quality, flexibility and cost efficiency [30]. Figure 1.7 shows schematic view of dip coating process.

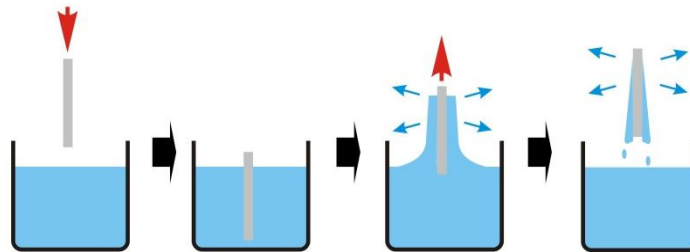


**Figure 1.7:** Schematic view of dip coating process.

### 1.4. Materials

Selection of proper materials for given situation is important. Both mechanical and physical properties should be known to predict final body behavior. There are more parameters to take into account like toxicity, cost, etc. Engineering is to find optimum point for every perspective. Selecting right materials is more complex for composite technology, because the behavior of one or more material may change during merging process.

Glass is very common material for different applications and it is amorphous solid. Generally, they are brittle and transparent. It has been traditionally used for bowls, vases, bottles, jars and glasses. Moreover, glass is very durable, even glass fragments can be found from early glass-making cultures. After suitable production method (poured, formed, extruded, and molded) finished glass product is brittle and will fracture, unless treated specially or laminated.

Improving mechanical strength of glass has been worked for many years. Many scientists have tried reinforcing glass with both inorganic and organic materials. Both ultimate strength and toughness properties are improved via polyvinyl butyral (PVB) which is an organic resin, also it provides safer breaking conditions by means of holding glass particles together. Laminated safety glass for cars and architectural fields are the main applications area. However, the negative effects (degradation, etc.) of sunshine on organic materials are well known. Therefore, PVB may not be the best selection for materials in touch with human body like glasses, plates, etc. Inorganic materials are generally more stable in rough environmental conditions.

#### **1.4.1. $\text{TiO}_2$ – $\text{SiO}_2$**

Silicon dioxide ( $\text{SiO}_2$ ) is also known as silica. Generally, it is found as quartz.  $\text{SiO}_2$  displays variable specific properties, which contribute to their wide usage area such as composites, biomaterials, sensory materials and coatings.  $\text{SiO}_x$  is promising additive because of porous structure and adsorption properties.  $\text{SiO}_2$  has extremely high surface activity and adsorbs various ions and molecules [31]. Figure 1.8 shows pure silicon dioxide powder.



**Figure 1.8:** Pure silicon dioxide.

The major part of produced silica is consumed by construction industry. Precursor to glass and silicon metal, food and pharmaceutical applications are the other common areas. Table 1.1 shows the mechanical properties of  $\text{SiO}_2$ .

**Table 1.1:** Mechanical properties of  $\text{SiO}_2$

<b>Mechanical Properties</b>	<b>SI Value</b>
Density	2.2 gr/cm <sup>3</sup>
Elastic modulus	73 GPa
Shear modulus	31 GPa
Bulk Modulus	41 GPa
Poisson's ratio	0.17
Compressive strength	1100 MPa
Hardness	5900 MPa

Titanium dioxide ( $\text{TiO}_2$ ) is also known as titania. Rutile, anatase and brookite are the most known minerals that occur in nature of  $\text{TiO}_2$ . Figure 1.9 shows pure titanium dioxide powder.



**Figure 1.9:** Pure titanium dioxide.

$\text{TiO}_2$  is used in composites for the increase of optical, electrical and mechanical properties. In addition,  $\text{TiO}_2$  has been used as additives to biomaterials in order to induce antimicrobial properties [32-33]. Besides, it shows photo-catalytic properties in presence of photons with wavelength lower than 388 nm [34]. There are many advantages of  $\text{TiO}_2$  such as white color, low toxicity, high stability, low cost have made this material an appropriate additive for many applications.  $\text{TiO}_2$  additive has

been added various composition to enhance their mechanical properties [35]. Table 1.2 shows the mechanical properties of titanium dioxide.

**Table 1.2:** Mechanical properties of  $\text{TiO}_2$ .

Mechanical Properties	SI Value
Density	4.01 gr/cm <sup>3</sup>
Elastic modulus	250 GPa
Shear modulus	101 GPa
Bulk Modulus	213 GPa
Poisson's ratio	0.27
Compressive strength	2100 MPa
Hardness	9750 MPa

Thus, combination of  $\text{TiO}_2$  –  $\text{SiO}_2$  binary system has been attracted many attentions recently [36].

#### 1.4.2. $\text{Ta}_2\text{O}_5$

Tantalum pentoxide ( $\text{Ta}_2\text{O}_5$ ) is an inorganic white solid that is insoluble in all solvents but strong bases and hydrofluoric acid. The crystal structure  $\text{Ta}_2\text{O}_5$  is little bit complicated. Disordered bulk material can be either amorphous or polycrystalline, however it is difficult to grow single crystals. Generally, it is hard to get crystal information via X-rays but powder diffraction. Figure 1.10 shows pure tantalum pentoxide.



**Figure 1.10:** Pure tantalum pentoxide.

Ta<sub>2</sub>O<sub>5</sub> has various precious properties such as chemical inertness [37], extremely high corrosion resistance [38], high surface sensitivity [39], high refractive index [40], high dielectric constant and compatibility with silicon [41-42].

With these unique properties, Ta<sub>2</sub>O<sub>5</sub> can be used different areas such as biomedical implants, surgical instruments, optical sensors, antireflective coating for lenses and solar panels, band-pass filters, mechanical sensors, transistor technology, ion sensors, and storage capacitors for dynamic random-access memory. Table 1.3 shows the mechanical properties of tantalum pentoxide.

**Table 1.3:** Mechanical properties of Ta<sub>2</sub>O<sub>5</sub>.

<b>Mechanical Properties</b>	<b>SI Value</b>
Density	8,25 gr/cm <sup>3</sup>
Elastic modulus	140 GPa
Shear modulus	54 GPa
Bulk Modulus	156 GPa
Poisson's ratio	0.23
Compressive strength	1900 MPa
Hardness	8750 MPa

#### **1.4.3. Carbon nanotube**

Carbon nanotube (CNT) is an allotrope of carbon with significant properties. It is known as strongest and stiffest material yet discovered. It has attracted a lot of attention due to mechanical and electrical properties and they are valuable for nanotechnology, electronics, optics and other materials science. CNTs are members of fullerene structural family [43].

There are two types of CNTs, single-walled carbon nanotubes (SWCNTs) and multi-walled carbon nanotubes (MWCNTs). Figure 1.11 shows single-walled and multi-walled carbon nanotubes.



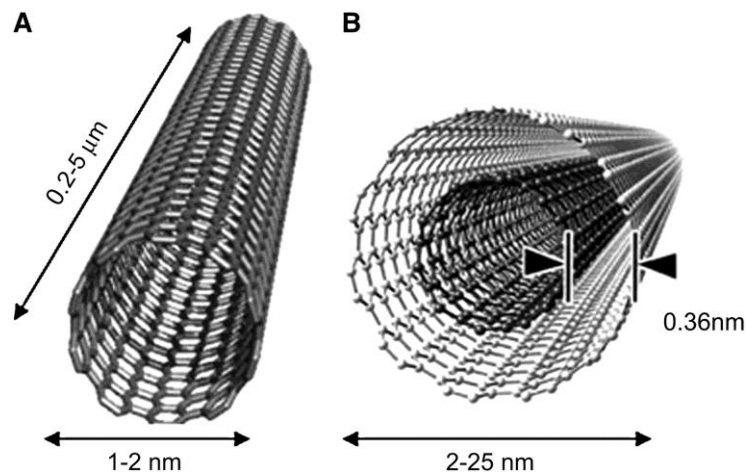


**Figure 1.11:** A) Single-walled carbon nanotube B) Multi-walled carbon nanotube

It can be produced with different techniques including arc discharge, laser ablation, high-pressure carbon monoxide disproportionation, and chemical vapor deposition (CVD). The most suitable method for batch production is CVD [44]. Table 1.4 shows the mechanical properties of single-walled carbon nanotubes.

**Table 1.4:** Mechanical Properties of SWCNTs.

Mechanical Properties	SI Value
Density	1,9 gr/cm <sup>3</sup>
Elastic modulus	1000 GPa
Shear modulus	478 GPa
Bulk Modulus	442 GPa
Poisson's ratio	0.1
Hardness	25 GPa

#### 1.4.4. Cerium (IV) oxide nanoparticles

Cerium (IV) oxide is also known as ceric oxide, ceria, cerium oxide and cerium dioxide (CeO<sub>2</sub>). It is pale yellow-white. CeO<sub>2</sub> is technologically important and rare earth material because of its different application areas such as polishing material [45], fuel cells [46], catalysts [47], UV blockers [48], protection against oxidative stress [49-53], neurodegeneration [54] and confers radiation protection [55]. Figure 1.12 shows pure cerium dioxide powder.



**Figure 1.12:** Pure CeO<sub>2</sub>.

For its most stable phase, bulk CeO<sub>2</sub> adopts a fluorite-type Fm<sub>3</sub>m crystal structure in which metal cation is surrounded by eight oxygen atoms [56-57]. The band gap of pure CeO<sub>2</sub> nano particle is ~5 eV [58-59]. Beside these optical properties, CeO<sub>2</sub> nano particles have some effect on mechanical properties especially on hardness and scratch resistance. It is also used in PP matrix for different applications [60]. Table 1.5 shows the mechanical properties of cerium dioxide.

**Table 1.5:** Mechanical properties of CeO<sub>2</sub>.

<b>Mechanical Properties</b>	<b>SI Value</b>
Density	7,2 gr/cm <sup>3</sup>
Elastic modulus	220 GPa
Shear modulus	66,2 GPa
Poisson's ratio	0.29

### 1.5. Measurement Systems

XRD and XPS have been used for phase analyses. UV-visible spectroscopy and NKD analyzer have been used to measure the optical transmittance and reflectance of thin films. SEM and AFM were used to examine the microstructure and the surface morphology of the films deposited on glass substrates. Ring-on-ring and scratch test were used to obtain mechanical properties of thin films and substrates. Profilometer was used to measure thickness of the films mechanically.

### 1.5.1. Mechanical tests

Ring on ring, which was the main mechanical test, was carried out at room temperature with Instron Corporation Series IX Automated Materials Testing System 8.33.00 testing machine at Şişecam Company. For brittle materials yield strength, ultimate strength and failure strength are pretty close to each other. Coated and uncoated glass substrates are compressed via two rings with different radius until they break. Failure strength was obtained for all samples via ring on ring test. The supporter ring radius was  $21\text{ mm}$  and the indenter ring radius was  $9,5\text{ mm}$ . Figure 1.13 shows the application of ring-on-ring test.

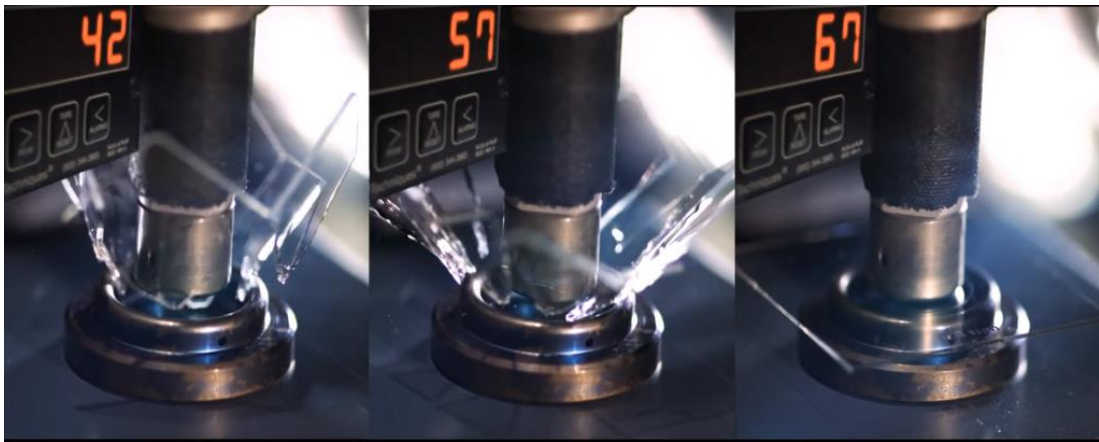


**Figure 1.13:** Application of ring-on-ring test to different glasses.

Second mechanical test in this paper was scratch test. It was done via sharp steel tip pen. The principle is that a harder object will scratch a softer object. Scratch hardness means the force require cutting through the film to the substrate for coating technology.

There are different measurements of hardness because the behavior of solids under force is complex.

- Scratch hardness
- Indentation hardness
- Rebound hardness

Ductility, plasticity, elastic stiffness, strain, strength, toughness, viscoelasticity and viscosity are the parameters that affect hardness [61].

### 1.5.2. X-Ray diffractometer (XRD)

X-rays are electromagnetic radiations, which lie between gamma rays and ultraviolet light in the electromagnetic spectrum. They are characterized by their wavelength. Excitation or scattering are the interaction between X-rays and matter.

XRD technique reveals information about the chemical composition and crystallographic structure of materials. In addition, it is a versatile and non-destructive. It is based on the elastic scattering, which causes only directional change of electromagnetic waves without energy loss. The detector will give a peak only and only if Bragg's Law ( $2d\sin(\theta) = n\lambda$ ) is satisfied for  $\theta$  direction. Figure 1.14 shows the working scheme of XRD.

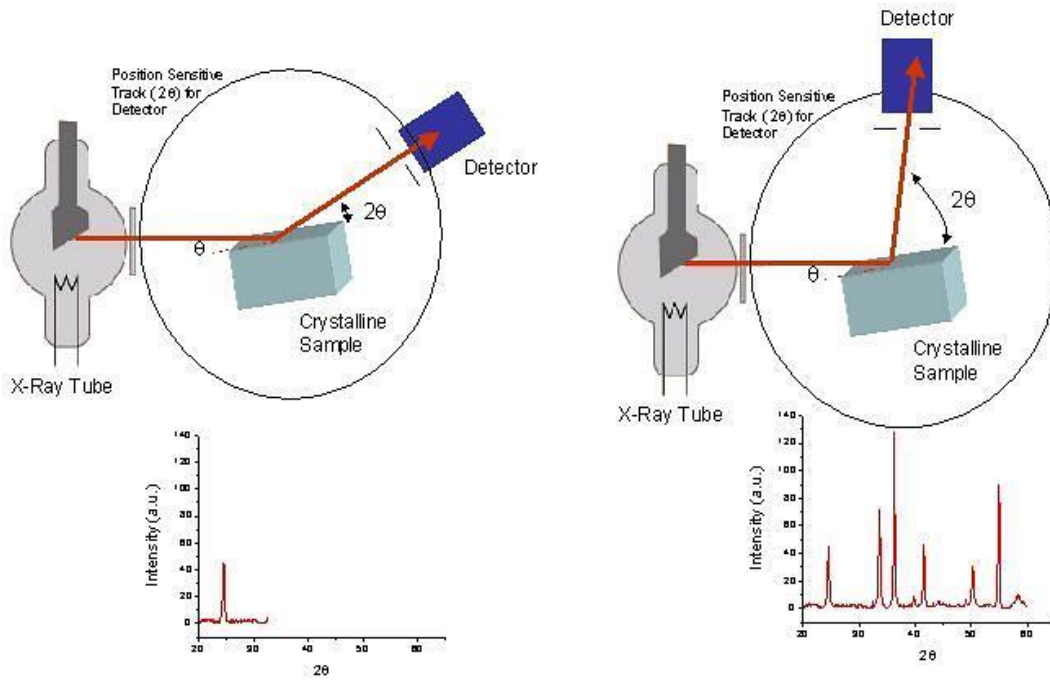


**Figure 1.14:** XRD working scheme.

In addition, the average crystalline size  $C_s$  can be estimated by *Scherrer's formula* [62] showed in eq. (1.1).

$$C_s = \frac{0.9 \lambda}{\beta \cos \theta} \quad (1.1)$$

where  $\lambda$  is X-ray wavelength,  $\beta$  is the full width at half maximum (FWHM) of the main peak of XRD spectrum and  $\theta$  is the Bragg angle. However, we should take into account line broadening due to the equipment and subtract from the experimental peak width.

The strain ( $\varepsilon$ ) in the film is calculated by [63],

$$\varepsilon = \left(\frac{1}{4}\right) \beta \cos \theta \quad (1.2)$$

Additionally chemical and structural analysis of the samples were done with Cu source (CuK $\alpha$ : 1.5418 Angstrom) in Bruker D8 Advance by X-ray diffractometer (XRD) device. The samples were measured directly on the Si holder by making solid samples into their powder and film states. Phase identification was achieved through International Centre for Diffraction Data (ICDD).

### 1.5.3. X-ray photoelectron spectroscopy (XPS)

XPS is a surface sensitive quantitative spectroscopy technique. It measures empirical formula, electronic state and chemical state of elements that exists in given material. The data is obtained by irradiating material with a beam of X-rays while simultaneously measuring the kinetic energy and number of escaping electrons from the top 0 to 10 nm. XPS needs vacuum or ultra-high vacuum conditions and it is a surface chemical analysis technique that is becoming a standard in order to understand the properties of solid surface. Figure 1.15 shows the working scheme of XPS.

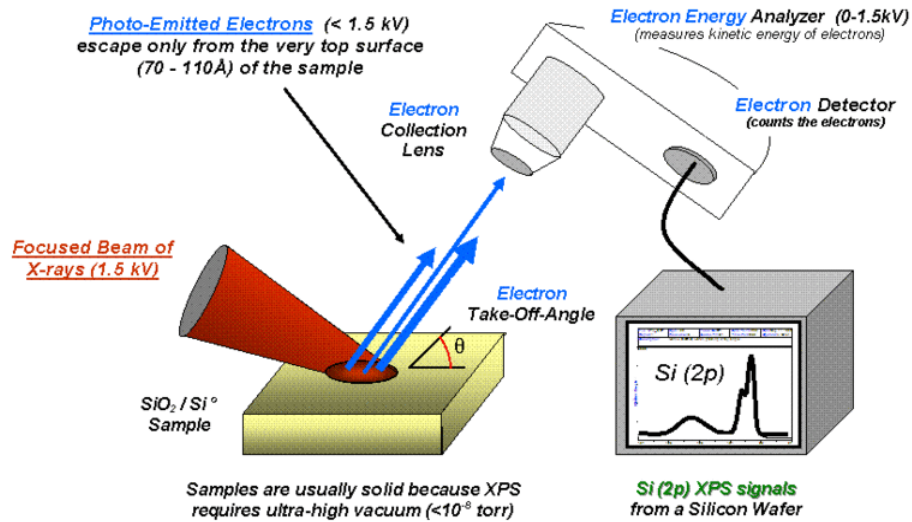


**Figure 1.15:** XPS working scheme.

X-ray photoelectron spectroscopy (XPS) measurements were performed using a Thermo Scientific K-Alpha spectrometer using an aluminum anode (Al K $\alpha$  = 1468.3 eV) at electron take-off angle of 90° (between the film surface and the axis of the analyzer lens). Spectra were processed using Thermo Avantage 5.903 software. All

spectra were calibrated with C1s residual peak at a binding energy of 285 eV to correct for the energy shift caused by charging.

#### 1.5.4. Scanning electron microscopy (SEM)

SEM enables the investigation of specimen with a resolution even to the nanometer scale. It is possible to obtain an image up to 25 Å detail with a high resolution SEM. The composition of individual crystals can be determined via SEM in conjunction with EDS. Regular SEM requires high vacuum environment.

Generally, a tungsten filament or a field emission gun is used as electron source. The electron beam is accelerated through high voltage like 20 kV. Afterwards accelerated electrons pass through apparatus and electromagnetic lenses to produce a thinner beam of electron. Scan coils lead the beam scanning the surface of specimen. Secondary electron detector collects the electron emitted from the specimen. The test finishes when the beam scans given surface area completely. Figure 1.16 shows the working scheme of scanning electron microscopy.

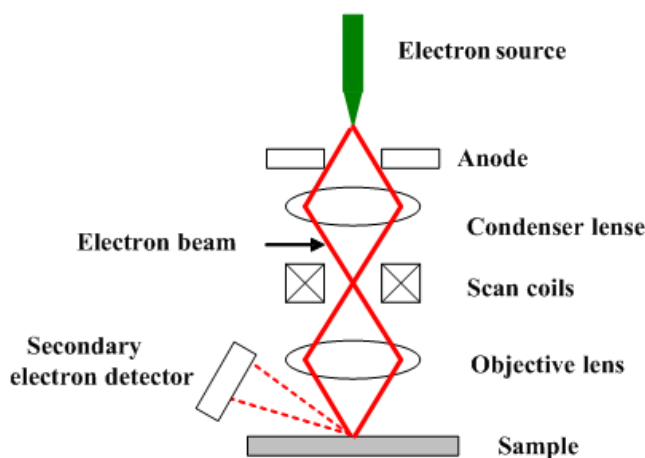


**Figure 1.16:** Working scheme of SEM.

A JEOL 6320 FV FE-SEM was used to examine the microstructure and the surface morphology of the films deposited on glass substrates.

#### 1.5.5. Ultraviolet-visible spectroscopy

Ultraviolet-visible spectroscopy uses light in the visible and very neighbor (near-UV and near infrared) ranges. It gives information about reflectance and transmittance of sample for different wavelengths. UV and visible light have adequate energy to excite electrons towards outer shells. This technique is applied on transition metal

ions, highly conjugated organic compounds and biological macromolecules. Generally, solutions are investigated but solids and gases may be also studied. UV-vis is not the best method for characterization. Hydrogen or deuterium bulb is used for UV measurements; tungsten bulb is used for visible region. Figure 1.17 shows the working scheme of UV-vis.

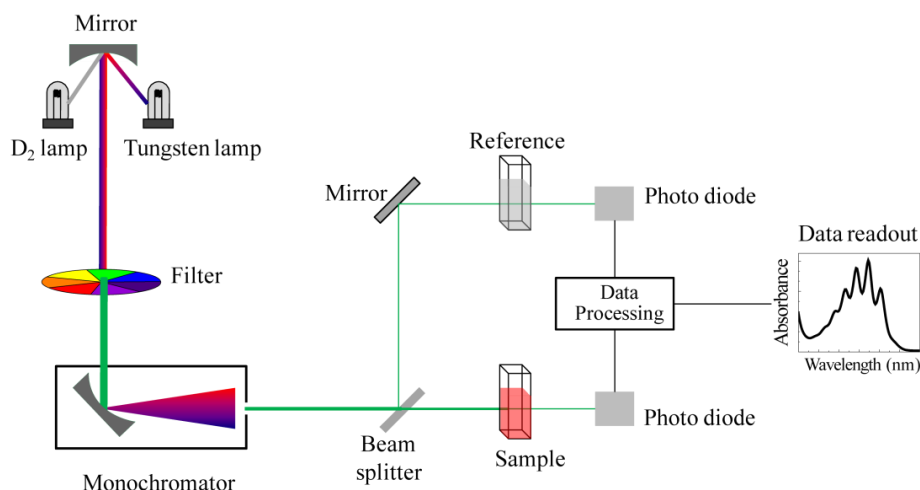


**Figure 1.17:** UV-vis working scheme.

#### 1.5.6. NKD analyzer

NKD-7000 UV-vis spectrophotometer was used to measure transmittance ( $T$ ) and reflectance ( $R$ ) of thin films for  $p$  and  $s$  polarization, separately. Wavelength was ranged 300-1000 nm. Quartz is used as reference material. The light excites the sample with  $30^\circ$  and the device measures transmittance and reflectance at the same time by comparing them with the results of quartz.

#### 1.5.7. Atomic force microscopy

Atomic force microscopy (AFM) is also known as scanning force microscopy (SFM), is a very high-resolution technique for scanning probe microscopy. Resolution can be on the order of nanometers. The precursor to the AFM is the scanning tunneling microscopy. Mechanical probe feels the surface in order to give information about it. Piezoelectric element moves very tiny but accurate and precise for extremely precise scanning. It consists of a cantilever and a sharp tip (probe) that scans sample surface. When the probe and sample surface approximate very closely, forces between them cause cantilever to deflect according to Hooke's Law. Deflection is measured by photodiodes that detect laser spot reflected from the top

surface of cantilever. Contact, tapping and non-contact are the types of AFM. It gives 3-dimensional surface profile and Figure 1.18 shows schematic of AFM.

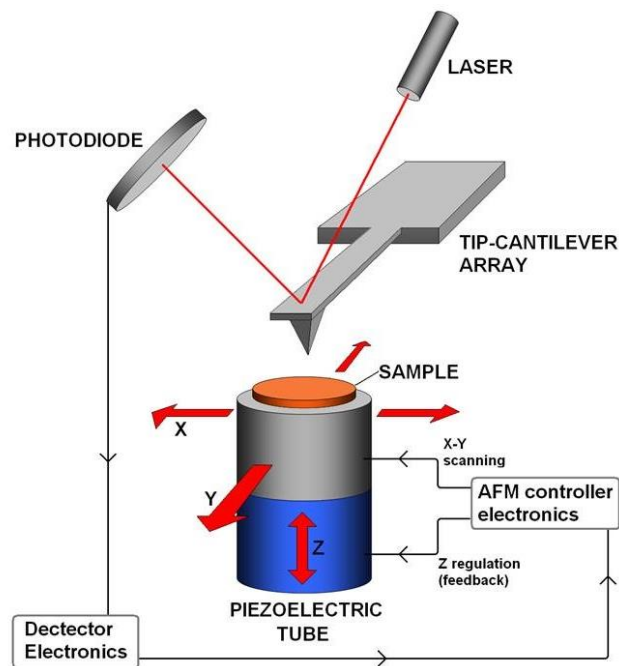


**Figure 1.18:** Schematic view of AFM.

Shimadzu SPM-9500J3 was used to examine surface profile of thin films.

### 1.5.8. Tensiometer

Tensiometers measure contact angle, surface free energy and drop volume. Surface tension and interfacial tension can also be measured. Tensiometers measure advancing and receding angles that is another key feature for contact angle measurements. Figure 1.19 shows the wetting types and the contact angle between surface and liquid.



**Figure 1.19:** Wetting types and contact angle.



KSV Theta Lite Optical Tensionmeter was used to measure contact angle of pure water on thin films.

#### **1.5.9. Finite element method**

Finite element method (FEM) is a numerical method and it has been commonly used for various multiphysics problems recently. FEM is applied for:

- Solid mechanics (gear, automotive power train)
- Structure analysis (cantilever, bridge, oil platform)
- Thermal analysis (thermal stress of brake discs, heat radiation of finned surface)
- Dynamics (earthquake, bullet ,impact)
- Electrical analysis (electrical signal propagation, piezo actuator)
- Biomaterials (human tissues and organs)

FEM is developed for solving solid mechanics problem. It seeks the answer for values of the stress, strain and displacement at each material point. Dividing the interval of integration and choosing proper simple functions to approximate the true function in each sub-interval are the two key steps. The numerical results are an approximation to real solution. Number of sub-interval and approximate function are the main parameters for the accuracy of numerical result [64].

*Ansys* is engineering simulation software, which uses FEM to understand behavior of materials in any situation. *Ansys 15* was used in this paper.

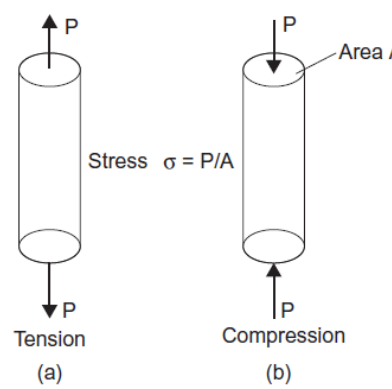


## 2. MECHANICS OF MATERIALS, THIN FILMS AND SUBSTRATES

In this section, brief information about general mechanics will be given. It is very important to know the basics before going further. After that, mechanics of thin films and substrates will be given in detail.

### 2.1. Stress

The easiest explanation is, internal force acting on given area of cross section. There are two types: pulling forces are named as tension and pushing forces along to its axis as compression. It is also expressed as force intensity. Eq. (2.1) gives the relation between stress and force and Figure 2.1 shows axial stress types.

$$\text{Stress} = \left( \frac{\text{Force}}{\text{Area}} \right) \quad (2.1)$$


**Figure 2.1:** (a) Object under tension, (b) object under compression.

It is expressed as Newton per square meter or *Pascal* in *SI* units and pounds per square inch or *psi* in *CGS* units. It has two components, normal and shear stress.

$$\text{Normal Stress} = \frac{\text{Force normal to given area}}{\text{Area on which the force acts}} \quad (2.2)$$

Greek letter sigma ( $\sigma$ ) is used to express normal stress. For tensile stress  $\sigma$  is indicated by positive value; for compression stress, it is negative.

$$\text{Shear Stress} = \frac{\text{Applied force}}{\text{Area on which the force acts}} \quad (2.3)$$

Greek letter tau ( $\tau$ ) is used to express shear stress. If the applied force has two components, which are equal, and opposite parallel forces that is not applied on same line of action, there will be a tendency for sliding between bodies. Figure 2.2 shows the schematic application of shear stress.

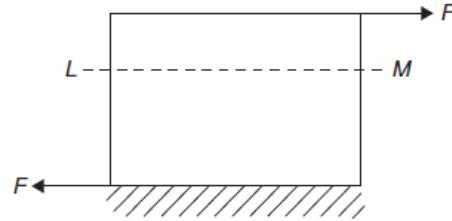


**Figure 2.2:** Shear stress because of two equal and opposite parallel forces.

Shear stress has same unit as normal stress [65].

## 2.2. Strain

When external forces act on a body, there will be position change for each individual point, which means deformation for entire body. The movement of given point from the initial position is called strain. External forces cause body to deform as well as temperature change. Elongation per unit length is defined as normal strain and it is dimensionless. Strains are categorized as normal and shear strain. Figure 2.3 shows different strain types.

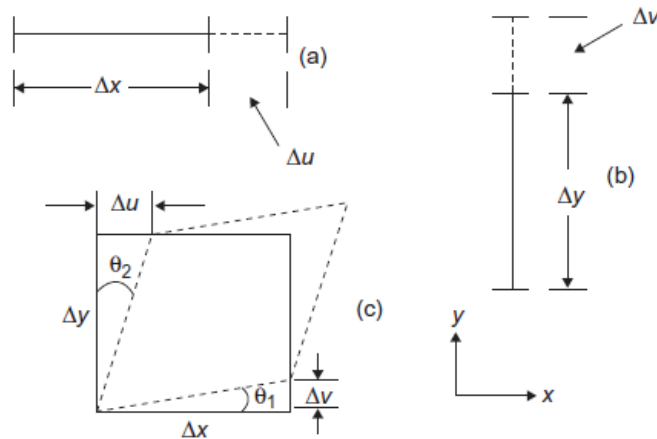


**Figure 2.3:** (a) Normal strain in the x-direction, (b) normal strain in the y-direction, (c) shear strain in the x-y plane.

Greek letter epsilon ( $\epsilon$ ) is used to express normal strain.

$$\text{Normal strain} \frac{\text{Elongation}}{\text{Original length}} = \frac{\delta}{L} \quad (2.4)$$

Shear strain is defined as angular change in given directions and expressed with  $\gamma_{xy}$ . XY means the direction of deformation [65].

### 2.3. Hooke's Law for Elastic Materials

Elastic material means it returns its original position with removal of external forces. In elastic region, applied loads are always proportional to deformations. Thus, if materials are elastic,

$$\frac{\text{Stress}}{\text{Strain}} = \text{constant} \quad (2.5)$$

For elastic materials, any deformation produced by external forces will be completely recovered when the load is removed.

If a material shows uniform properties throughout in all directions, it is called *isotropic*, conversely if it is not uniform, it is called *anisotropic*.

*Orthotropic* material means having different properties in different planes [66].

### 2.4. Modulus of Elasticity (Young Modulus)

Equation (2.5) shows ratio of stress to strain is constant in elastic deformation region. So that eq. turns into,

$$E = \frac{\sigma}{\epsilon} \quad (2.6)$$

This constant  $E$  is usually assumed to be the same in tension or compression. It is one of the most important properties of materials. For most of engineering materials it has a high numerical number i.e.,  $E = 200 \times 10^9 \text{ N/m}^2$  for steel.

It is determined by carrying out a standard tensile test on specimen. The nominal stress at failure is called *ultimate tensile stress* for given material. Stress - strain curves are given in Figure 2.4.

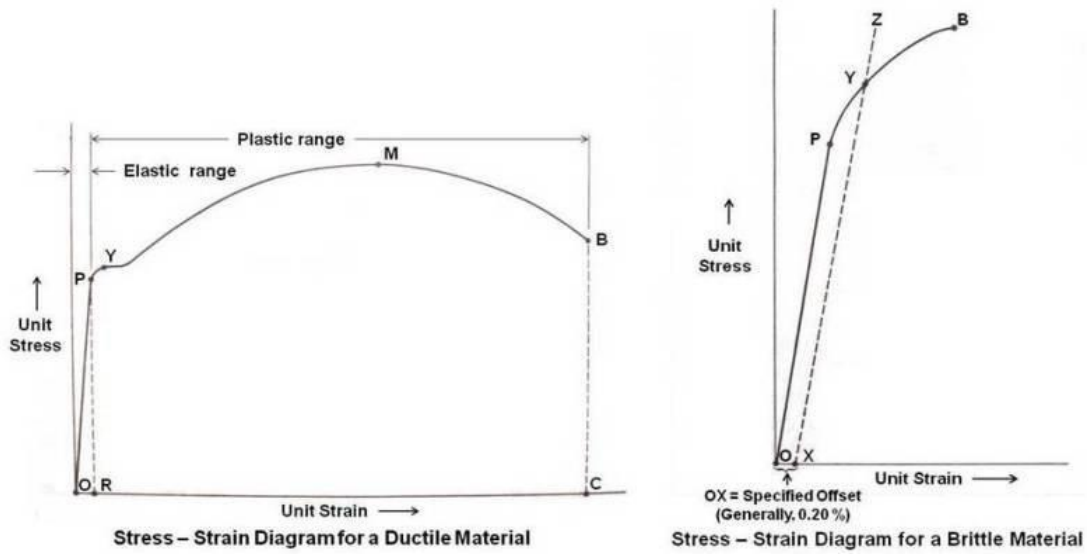


**Figure 2.4:** Stress - strain curves.

There is huge difference between the graphs of two different materials in Figure 2.3. For the first sample, plastic deformation range covers much wider part of strain axis than elastic part. Total capacity for plastic deformation, material to allow large extensions is termed its *ductility*. Materials with high ductility are called *ductile materials*; on the other hand, materials with low ductility are termed as *brittle materials*. Quantitative value of ductility is determined by both eq. (2.7) and (2.8)

$$\text{Percentage elongation} = \frac{\text{Increase in gauge length to fracture}}{\text{Original gauge length}} \times 100 \quad (2.7)$$

$$\text{Percentage reduction in area} = \frac{\text{Reduction of cross sectional area}}{\text{Original area}} \times 100 \quad (2.8)$$

Brittle materials show very little plastic deformation before failure and there is little or no necking at fracture [66].

## 2.5. Poisson's Ratio

If biaxial tensile stress is applied to a bar, it also exhibits a reduction in dimension laterally. The ratio of longitudinal extension to breadth and depth contraction is termed as *Poisson's Ratio*. Greek letter nu ( $\nu$ ) is used to express and it has always negative value between  $-0.5 < \nu < 0$  [37]. Eq. (2.9) gives Poisson's Ratio by,

$$\nu = \frac{\text{Lateral strain}}{\text{Longitudinal strain}} \quad (2.9)$$

## 2.6. Mechanics of Nano Crystalline Materials

The main purpose of miniaturization is creating perfect, defect free materials. As we know, various defects affect final properties. If we could arrange final material atom by atom, many things would be different. This is the main reason why nanotechnology has become so popular recently.

Materials are produced with grain size in the range of nanometers led to expectation to have extremely high strength. The empirical *Hall-Petch equation* predicts that,

$$\sigma_y = \sigma_0 + \frac{k}{\sqrt{d}} \quad (2.10)$$

where  $\sigma_y$  is yield strength,  $\sigma_0$  is friction stress,  $k$  is a material constant and  $d$  is the grain size of material. According to this equation, yield strength goes extremely high values for very fine grain size. However, many experiments show that yield strength falls well below that calculated by Hall-Petch equation [67].

### 2.6.1. Density, pores and microcracks

Previous nanocrystalline researches show that, for given samples, density measurements gave values ranging only about 70% to >90% of the single crystal density [68-69]. The density shortfall was caused by nanocrystalline grain boundaries having extremely low densities [68] or primarily by the presence of pores [70]. Porosity has significant effect on the elastic modulus and the other mechanical properties as well, so it is very important to detect number and size of the pores.

Generally, positron spectroscopy is used to identify voids in nanocrystalline sample. The smallest ones are presumed to be located at *grain interfaces*. The middle-sized voids are located at *grain triple junctions*. The largest ones are identified with *missing grain pores* [67].

## 2.7. Thin Films and Substrates Mechanics

Many studies have been done in order to calculate mechanical behavior of films so far. We can consider thin film problem as biaxial bending of a thin plate. Figure 2.5 shows biaxial bending of a thin plate.

M = moment per unit length applied along edges of plate.

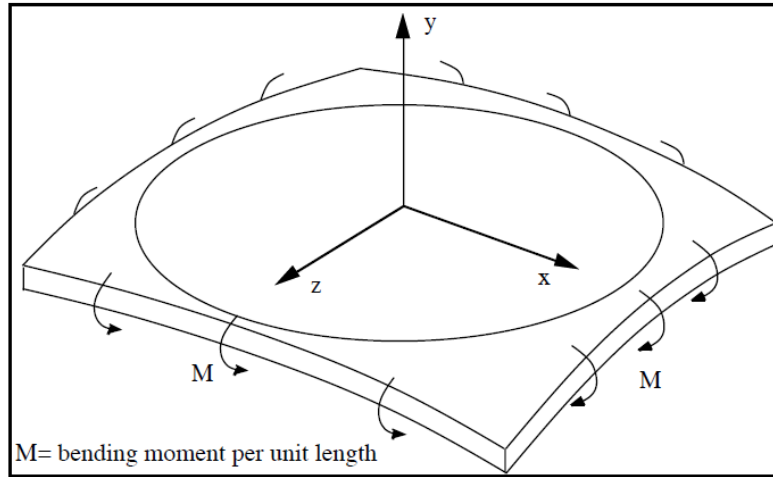


**Figure 2.5:** Biaxial bending of a thin plate.

### 2.7.1. Bending stresses

The biaxial stress distribution is (for pure bending):

$$\sigma_{xx} = \alpha y \quad (= \sigma_{zz}) \quad (2.11)$$

as shown in the Figure 2.6.

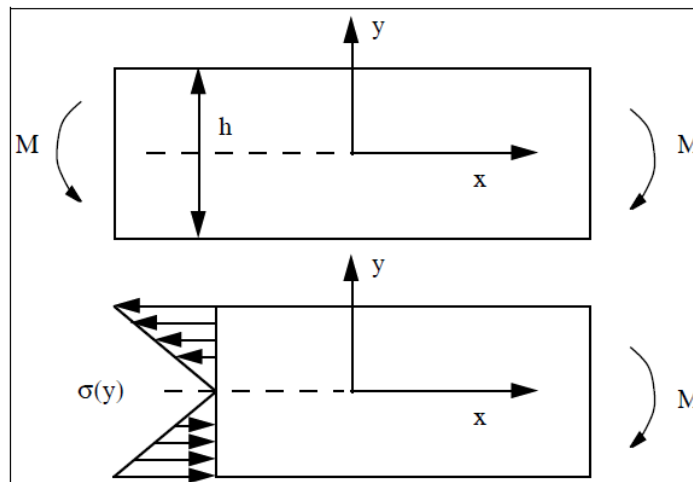


**Figure 2.6:** Bending moments and stress distribution.

The stresses in the beam are related to the bending moment. The moment (per unit length along the edge) is related to the stresses in the plate by,

$$M = \int_{-h/2}^{h/2} \sigma_{xx} y dy = \int_{-h/2}^{h/2} \alpha y^2 dy = \frac{\alpha h^3}{12} \quad (2.12)$$

$$\alpha = \frac{12M}{h^3} \quad (2.13)$$



Thus the stresses are:

$$\sigma_{xx} = \sigma_{zz} = \frac{12M}{h^3} y \quad (2.14)$$

with all other stress components being zero [10].

### 2.7.2. Curvature of radius

The relation between bending stress and curvature (for pure bending),

$$\epsilon_{xx}(y) = \frac{(R+y)\theta - R\theta}{R\theta} = \frac{y}{R} = -\kappa y \quad (2.15)$$

If we want to obtain relation between curvature and strain,

$$\kappa = -\frac{1}{R} = \frac{-\epsilon_{xx}(y)}{y} \quad (2.16)$$

### 2.7.3. Curvature associated with a biaxial bending moment

We must calculate  $\epsilon_{xx}(y)$  to obtain curvatures. If we apply Hooke's Law (isotropic), the strain is,

$$\epsilon_{xx} = \frac{1}{E} [\sigma_{xx} - \nu (\sigma_{yy} + \sigma_{zz})] \quad (2.17)$$

where,

$$\sigma_{yy} = 0 \text{ and } \sigma_{zz} = 0.$$

Then we can obtain biaxial stress-strain relation,

$$\epsilon_{xx} = \frac{(1-\nu)}{E} \sigma_{xx} \quad (2.18)$$

Specifically, the strain and stress are,

$$\epsilon_{xx}(y) = \frac{(1-\nu)}{E} \sigma_{xx}(y) \quad (2.19)$$

The stress is related to the moment by eq. (2.14) so that,

$$\epsilon_{xx}(y) = \frac{(1-\nu)}{E} \frac{12M}{h^3} y \quad (2.20)$$

Finally, the relation between the applied moment and the resulting curvature is,

$$\kappa = -\frac{(1-\nu)}{E} \frac{12M}{h^3} \quad (2.21)$$

#### 2.7.4. Deflection associated with biaxial bending

It can be considered as negative curvatures  $\sim$  negative displacement. From eq. (2.21) and Figure 2.7 shows plate deflection due to moment.

$$\frac{d^2 u_y}{dr^2} = \kappa = -\frac{(1-\nu)}{E} \frac{12M}{h^3} = \text{constant}$$

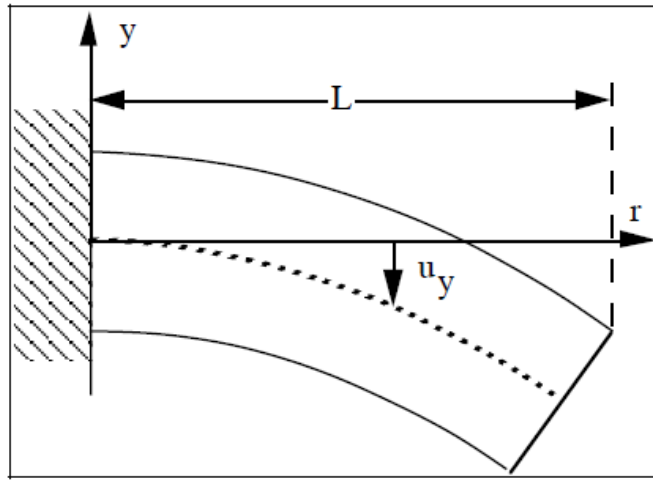


Figure 2.7: Plate deflection.

The curvature is constant for pure bending. Integrate the equation to obtain,

$$\frac{du_y}{dr} = \kappa r + c_1 \quad (2.22)$$

If we apply boundary conditions,

$$\frac{du_y}{dr} = 0 \text{ at } r = 0 \text{ to obtain } c_1 = 0.$$

If we integrate again to find,

$$u_y = \frac{\kappa r^2}{2} + c_2 \quad (2.23)$$

with boundary conditions,

$$u_y = 0 \text{ at } r = 0 \text{ to obtain } c_2 = 0.$$

The final equation is,

$$u_y = \kappa \frac{r^2}{2} = -\frac{(1-\nu)}{E} \frac{12M}{h^3} \frac{r^2}{2} \quad (2.24)$$

If we need cartesian coordinates,

$$u_y = -\frac{(1-\nu)}{E} \frac{12M}{h^3} \frac{(x^2+z^2)}{2} \quad (2.25)$$

Finally, at the edge of the plate ( $r = L$ ),

$$u_y (r = L) = -\frac{(1-\nu)}{E} \frac{6ML^2}{h^3} \quad (2.26)$$

We should that a positive moment creates a negative curvature and also negative displacements [10].

### 2.7.5. Thin Film Stresses

A stress free film of thickness  $t_f$  bonded to stress free substrate of  $t_s \gg t_f$ . Figure 2.8 shows the schematic view of film on a substrate.

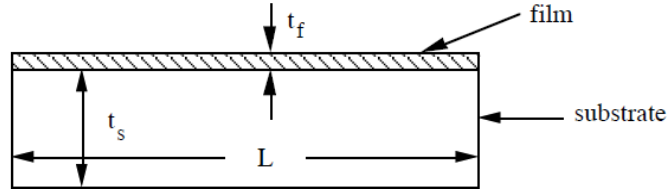


**Figure 2.8:** Thin film on a substrate.

If we consider the typical case in which  $L \gg t_s$ , so the substrate behave as a plate. If we attach any thin film on a stress free substrate, every thin film stresses are caused by the elastic accommodation of an incompatibility between the film and the substrate. If that film is removed from substrate and allowed to change its dimensions, that is, become incompatible with the substrate. The film is then elastically strained to again match the substrate via phase transformation.

It is considered as the stress in the film can be caused by incompatibilities or misfit between the film and the substrate:

- Differences in thermal expansion,
- Phase transformations with volume changes,

- Densification of the film,
- Epitaxial effects.

It is easier to make calculations, if it is thought as film is free of the substrate. Then allow the film to shrink or expand relative to the substrate. The final state is then achieved by deforming both the film and substrate so that they again fit together perfectly [10]. Figure 2.9-2.11 shows thin film stress and its effect on substrate.

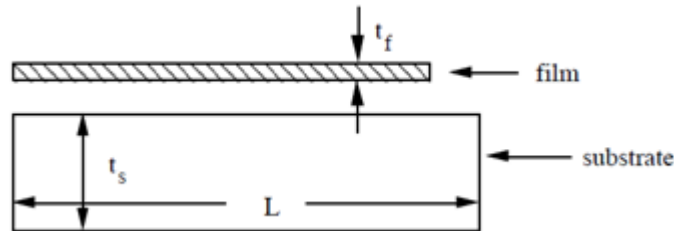


**Figure 2.9:** The film and substrate in a stress free state.

To fit the film, we should apply biaxial tension force to the film.

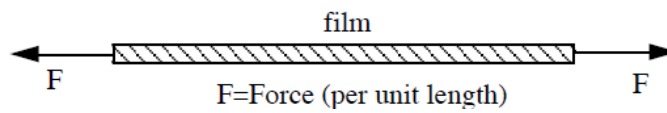


**Figure 2.10:** Stretching the film.

An equal and opposite directional force must be applied to the edge of the substrate.

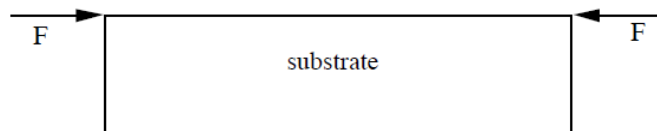


**Figure 2.11:** Substrate forces.

Biaxial tension stresses are created by the tension forces in the film, on the other hand biaxial compression and biaxial bending are produced by the compressive force on the substrate [10].

#### 2.7.6. Film stress - curvature relation

Assume that a biaxial tension stress,

$$\sigma_{xx} = \sigma_{zz} = \sigma_f$$

exist in the film as shown in Figure 2.12. So,

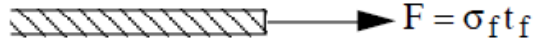


**Figure 2.12:** Film forces.

and for the substrate in Figure 2.13,

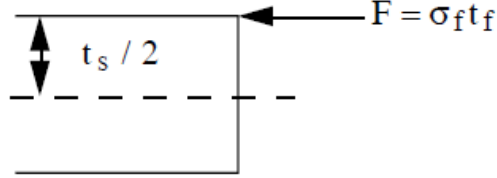


**Figure 2.13:** Substrate forces.

which leads to a moment is shown in Figure 2.14,

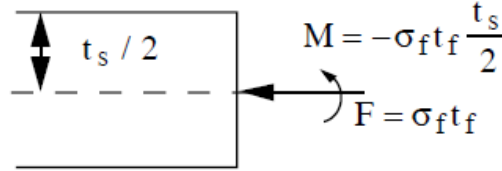


**Figure 2.14:** Moment effect due to external forces.

This moment bends the substrate eq. (2.21),

$$\kappa = -\frac{(1-\nu)}{E} \frac{12M}{t_s^3} = -\frac{(1-\nu)}{E} \frac{12}{t_s^3} \left( -\sigma_f t_f \frac{t_s}{2} \right) \quad (2.27)$$

$$\kappa = -\frac{(1-\nu_s)}{E_s} \frac{6\sigma_f t_f}{t_s^2} \quad (2.28)$$

thus, the stress in film is eq. (2.16) and (2.28),

$$\sigma_f = \left( \frac{E_s}{1-\nu_s} \right) \frac{t_s^2}{6t_f} \kappa = \left( \frac{E_s}{1-\nu_s} \right) \frac{t_s^2}{6t_f R} \quad (2.29)$$

Eq. (2.29) is called *Stoney Relation*. It was derived first for beams but then generalized for plate.

We can obtain that from the film stress-curvature relation:

- To find film stress, we must measure the curvature of the substrate.
- Substrate, the elastic properties of substrate and the dimension of film are the only parameters that affect the results, not the properties of the film [10].

### 2.7.7. Stresses in film and substrate (far from the edges of the film)

The stresses in the film are biaxial and all other components are zero.

$$\sigma_{xx} = \sigma_{zz} = \sigma_f$$

This biaxial stress include both biaxial compression (or tension) and biaxial bending stresses.

$$\sigma_{xx} = \sigma_{zz} = \sigma_{compression} + \sigma_{bending}$$

The forces acting on the substrate can be used to calculate these components is shown in Figure 2.15,

$$\sigma_{compression} = -\frac{F}{t_s} = -\frac{t_f}{t_s} \sigma_f$$

$$\sigma_{bending} = \frac{12M}{t_s^3} y$$

$$\sigma_{bending} = -\frac{6\sigma_f t_f}{t_s^2} y$$

**Figure 2.15:** Calculation of stresses.

### 2.7.8. Stress diagram

Stresses at the interface between film and substrate is shown Figure 2.16, where  $y=t_s/2$  are,

in the film,

$$\sigma_{xx} = \sigma_f$$

in the substrate,

$$\sigma_{xx} = \sigma_{compression} + \sigma_{bending}$$

$$\sigma_{xx} \left( y = \frac{t_s}{2} \right) = -\frac{t_f}{t_s} \sigma_f - \frac{3t_f}{t_s} \sigma_f = -\frac{4t_f}{t_s} \sigma_f \quad (2.30)$$

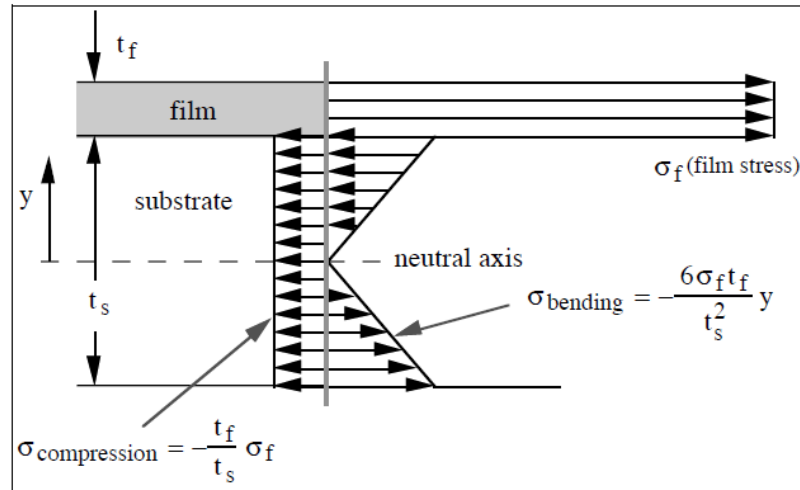


**Figure 2.16:** Stresses in film and substrate.

For example,

$t_f = 1 \mu m$  and  $t_s = 500 \mu m$ , stress in substrate eq. (2.30),

$$\sigma_{xx} \left( \text{substrate } y = \frac{t_s}{2} \right) = - \frac{4t_f}{t_s} \sigma_f = - \frac{4}{500} \sigma_f$$

As we can see here, the substrate stresses are about 100 times smaller than the film stresses. The forces transmitted between the film and the substrate act through the interface only near the edges of the film.

If there are two or more films on a substrate, each film deposited imposes a separate bending moment, which produces a curvature [10].

### 2.7.9. Interfacial stresses

Stresses in the film cause stresses to develop in the substrate. Thus, across the film/substrate interface there should be some forces that are transmitted. If we consider part of the film far from the edges in Figure 2.17,

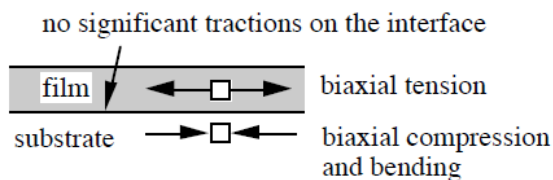


**Figure 2.17:** Stresses in film and substrate.

Because the film thickness is much smaller than the substrate thickness; on the film substrate interface, very little normal traction is observed. Figure 2.18 shows the force balance.

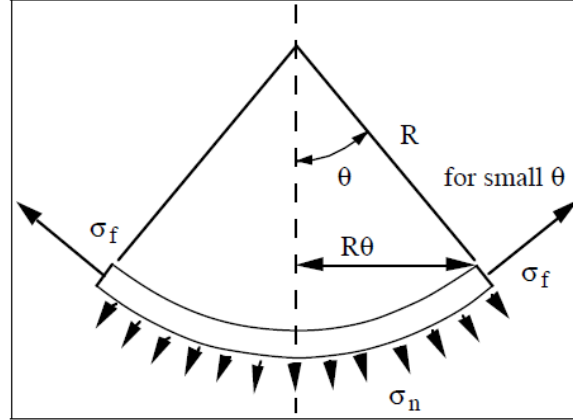


**Figure 2.18:** Force balance.

Free body analysis,

$$F_{up} = 2\pi(R\theta)\sigma_f t_f \sin\theta$$

$$F_{down} = \sigma_n \pi (R\theta)^2$$

By equaling the forces,

$$2\pi(R\theta)\sigma_f t_f \sin\theta = \sigma_n \pi (R\theta)^2$$

We can find the normal stress on the interface by,

$$\sigma_n = \frac{2t_f}{R} \sigma_f \sin\theta$$

for example,

$$t_f = 10^{-6} \text{ m},$$

$$R = 100 \text{ m}$$

then we obtain the normal stress on the interface,

$$\sigma_n = 2 \times 10^{-8} \sigma_f$$



It is very small stress [10].

#### 2.7.10. Edge effects and interfacial shear stresses

Thin film stresses apply forces on the substrate and it is known that interfacial forces can be negligible among far regions from the edges. Therefore, these interfacial forces are important only near the edges of the film. Figure 2.19 shows the misfit strain.

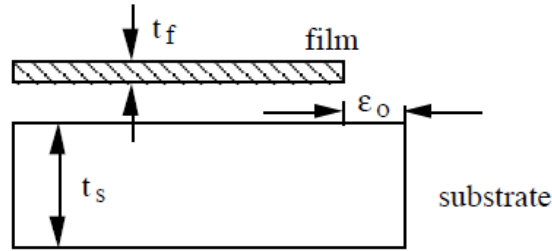


**Figure 2.19:** Misfit strain.

Biaxial tensile stress should apply to align film to substrate like shown in Figure 2.20.

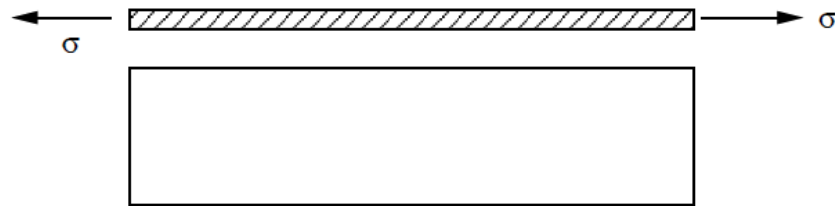


**Figure 2.20:** Film with external loading.

Internal forces inside the surface element on the edge are shown in Figure 2.21.

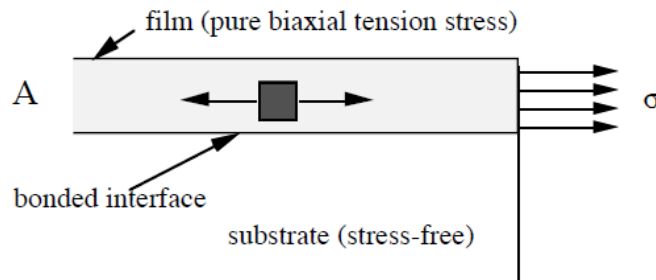


**Figure 2.21:** External edge loading.

To find final stress, we should add edge forces to remove the external forces. Figure 2.22 shows removal of edge forces.

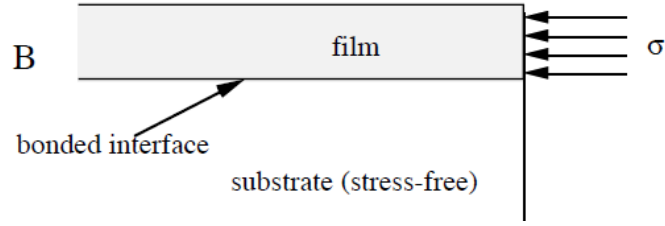


**Figure 2.22:** Removal of edge forces.

The stresses of the film near the edge can be calculated by summing the stresses Figure 2.21 and 2.22. Figure 2.23 shows the interfacial stress distribution.

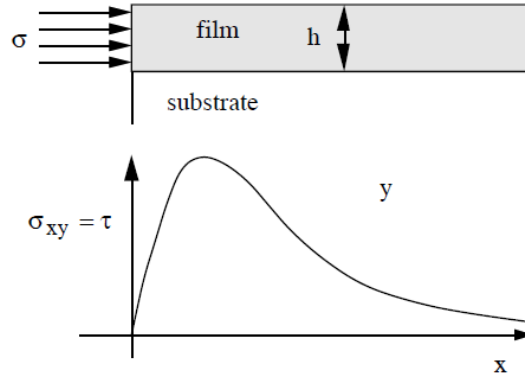


**Figure 2.23:** Interfacial stress distribution.

Assume,

$$\tau = A \frac{x}{h} \exp\left(-B \frac{x}{h}\right) = A\alpha \exp(-B\alpha) \quad (2.31)$$

If we apply force equilibrium,

$$\int_0^\infty \tau dx = \sigma h \text{ or } \int_0^\infty \tau d\alpha = \sigma \quad (2.32)$$

$\frac{d\tau}{d\alpha} = 0$  for maximum  $\alpha$ ,

$$\frac{d\tau}{d\alpha} = A\alpha \exp(-B\alpha) (-B) + A \exp(-B\alpha) = 0$$

$$(1 - B\alpha) A \exp(-B\alpha) = 0$$

so we obtain,

$$\alpha_{max} = \frac{1}{B} \quad (2.33)$$

We should apply force equilibrium again,

$$\int_0^{\infty} A\alpha \exp(-B\alpha) d\alpha = \sigma \quad (2.34)$$

or

$$\int_0^{\infty} A\alpha \exp(-B\alpha) d\alpha = \frac{\sigma}{A}$$

By partial integration,

$$\int_0^{\infty} A\alpha \exp(-B\alpha) d\alpha = \frac{1}{B^2} = \frac{\sigma}{A}$$

so we have,

$$A = \sigma B^2 = \frac{\sigma}{\alpha_{max}^2} \quad (2.35)$$

or

$$\tau = \frac{\sigma\alpha}{\alpha_{max}^2} \exp\left(-\frac{\alpha}{\alpha_{max}}\right)$$

The maximum interfacial shear stress is,

$$\tau_{max} = \tau(\alpha = \alpha_{max}) = \frac{\sigma}{e\alpha_{max}} \quad (2.36)$$

Exact placement of maximum shear stress depends on the rigidity of the substrate. Maximum shear stress moves toward edges, on the other hand for compliant substrates, it reaches maximum farther from edges [10]. Figure 2.24 and 2.25 shows the shear stress distribution for a rigid and compliant body, respectively.

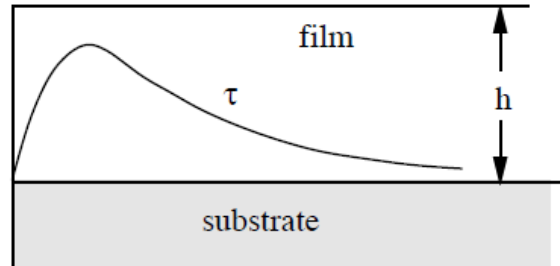


**Figure 2.24:** Shear stress distribution for a rigid substrate.

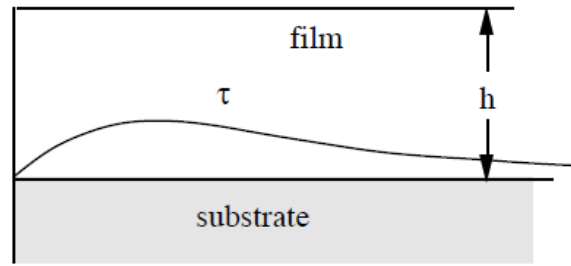


**Figure 2.25:** Shear stress distribution for a compliant substrate.

### **2.7.11. Theoretical mechanical analyses of multi layers with ring-on-ring test**

Multi layered systems are used in various applications. Thus, it is so important to keep reliability and stability. Generally, ceramic materials have high compressive strength but because of low ductility, they cannot resist high tensile loadings [71-72].

There are two main tests are used to measure flexure strength of ceramics. Three-point bending of beam and four-point bending of beam are the measurement techniques for uniaxial flexure tests and ball-on-ring, ball-on-three-ball, piston-on-ring and ring-on-ring tests are biaxial flexure tests. The maximum tensile stress, which is biaxial, is appeared at the center of the disk [73]. The flexural strength would be the same as the tensile strength if the material were homogeneous.

The piston-three-balls test has been standardized as *ISO 6872* (ISO 6872:2008 specifies the requirements and the corresponding test methods for dental ceramic materials for fixed all-ceramic and metal-ceramic restorations and prostheses.) for ceramic materials [74]. Biaxial flexure tests have some advantages over uniaxial flexure tests such as independency from edge conditions [75]. Real materials are faced multiple loadings during applications so results which is obtained from biaxial tests become more meaningful [73].

The flexural stress analyses are so complicated and hard to solve. It requires solving a biharmonic equation to understand relations between the transverse displacement and the load. In addition, there are boundary conditions to satisfy. Figure 2.26 shows the layer-by-layer stacking process.

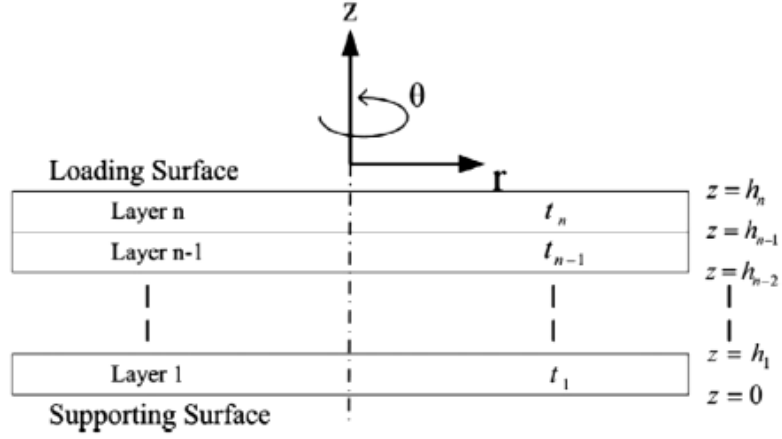


**Figure 2.26:** Schematic of an axial symmetry of a thin elastic multilayered disc showing.

The disc in Figure 2.26 is made up of  $n$  layers, which individually have  $t_i$  thickness. Subscript  $i$  represent the layer number starts from 1. The interface between  $i$  and  $i+1$  is expressed as  $h_i$ . Thus,  $h$  means the thickness of the disk is given in eq. (2.34).

$$h_i = \sum_i^j t_j \quad (i = 1 \text{ to } n) \quad (2.37)$$

The interface between discs is supposed to keep bonded during test.  $z = 0$  represents supporting ring and  $z = h_n$  shows loading ring surfaces.

The strains are proportional to the curvature of the disk also the distance between neutral axes and middle plane of the disc for mono layered structures. On the other hand, the neutral surface can derive from the mid plane due to different elastic properties.

The radial and tangential strains,  $\varepsilon_r$  and  $\varepsilon_h$  are [76]:

$$\varepsilon_r = \frac{z - z_{nr}}{r_r} \quad (0 \leq z \leq h_n) \quad (2.38)$$

$$\varepsilon_h = \frac{z - z_{n\theta}}{r_\theta} \quad (0 \leq z \leq h_n) \quad (2.39)$$

$z_{nr}$  and  $z_{n\theta}$  shows the position of the neutral surfaces in radial and tangential directions, respectively,  $r_r$  and  $r_\theta$  are the radius of curvatures. Eq. (2.38) and (2.39) show the strain distribution, while the stress normal can be ignored for a thin disc.

$$\sigma_{ri} = E_i^p (\varepsilon_r + \nu_i \varepsilon_\theta) \quad (i = 1 \text{ to } n), \quad (2.40)$$

$$\sigma_{\theta i} = E_i^p (\varepsilon_\theta + \nu_i \varepsilon_r) \quad (i = 1 \text{ to } n), \quad (2.41)$$

where  $E_i^p = E_i / (1 - \nu_i^2)$  is the plane strain modulus,  $E$  is Young's modulus,  $\nu$  is Poisson's ratio and  $i$  means the layer number.

The relationships between bending moment and stress are,

$$\sigma_{ri} = \frac{E_i^p (z - z_n^m) M_r}{D^m} \quad (2.42)$$

$$\sigma_{\theta i} = \frac{E_i^p (z - z_n^m) M_\theta}{D^m} \quad (2.43)$$

where  $M_r$  and  $M_\theta$  are the bending moments at two directions and  $D^m$  is the flexural rigidity of layer.  $D^m$  is obtained by providing the force and the bending moment's equilibrium conditions.

$$D^m = \sum_{i=1}^n E_i^p t_i \left[ h_{i-1}^2 + h_{i-1} t_i + \frac{t_i^2}{3} - z_n^m \left( h_{i-1} + \frac{t_i}{2} \right) \right] \quad (2.44)$$

The neutral surface position can be obtained by solving the force equilibrium conditions; however, expressions of  $z_{nr}$  and  $z_{n\theta}$  become very complex. If the difference between  $\nu_i$  is ignored in eq. (2.40) and (2.41), the  $z_{nr}$ 's description is simplified significantly. So if we assume  $\nu_i = \nu$ , the expression of  $z_{nr}$  and  $z_{n\theta}$  are,

$$z_n^m = z_{nr} = z_{n\theta} = \frac{\sum_{i=1}^n E_i^p t_i \left( h_{i-1} + \frac{t_i}{2} \right)}{\sum_{i=1}^n E_i^p t_i} \quad (2.45)$$

Radial and tangential neutral surfaces are equal and it is redefined as  $z_n^m$ . If we have a monolayer disc with uniform material properties,  $E_i = E$  and  $\nu_i = \nu$ , so for monolayer disc, stress and bending moment relations are eq. (2.14),

$$\sigma_r = \frac{12(z - z_n) M_r}{h_n^3} \quad (2.46)$$

$$\sigma_\theta = \frac{12(z - z_n) M_\theta}{h_n^3} \quad (2.47)$$

So, eq. (2.44) and (2.45) become,

$$D = \frac{E h_n^3}{12(1-\nu^2)} \quad (2.48)$$

$$z_n = \frac{h_n}{2} \quad (2.49)$$

Stress distribution in multilayered discs must have some relations with monolayer discs. If we compare eq. (2.42) and (2.43) with Eq. (2.46) and (2.47) we find that,

$$\sigma = \frac{E_i^p h_n^3}{\sum_{i=1}^n 2E_i^p t_i [6h_{i-1}^2 + 6h_{i-1}t_i + 2t_i^2 - 3z_n^m(2h_{i-1} + t_i)]} \sigma^* \quad (i = 1 \text{ to } n) \quad (2.50)$$

$\sigma^*$  and  $\sigma$  are the stresses in monolayer and multilayer discs, respectively. A schematic view of ring-on-ring tests is shown in Figure 2.27 and the top view is shown in Figure 2.28.

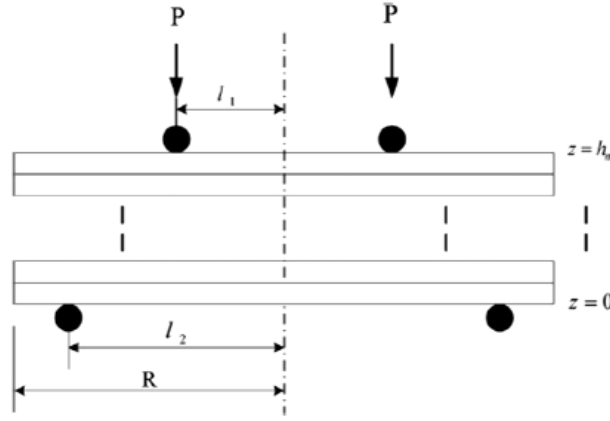


**Figure 2.27:** Schematic view of multilayered discs subjected to ring-on-ring test.

The specimen is supported by outer ring and loaded by smaller inner ring. Biaxial stress is decomposed into tangential  $\theta$  and radial  $r$  directions in the center area for monolayer discs. The stresses on the tensile surface are [75,77,78],

$$\sigma_r = \sigma_\theta = \frac{3P}{4\pi h_n^2} \left[ 2(1 + \nu) \ln \left( \frac{l_2}{l_1} \right) + \frac{(1-\nu)(l_2^2 - l_1^2)}{R^2} \right] \quad (r \leq l_1 \text{ and } z = 0) \quad (2.51)$$

$$\sigma_r = \frac{3P}{4\pi h_n^2} \left[ 2(1 + \nu) \ln \left( \frac{l_2}{r} \right) + \frac{(1-\nu)l_1^2(l_2^2 - r^2)}{(rR)^2} \right] \quad (r > l_1 \text{ and } z = 0) \quad (2.52)$$

$$\sigma_\theta = \frac{3P}{4\pi h_n^2} \left[ 2(1 + \nu) \ln \left( \frac{l_2}{r} \right) - \frac{(1-\nu)l_1^2(l_2^2 + r^2)}{(rR)^2} + 2(1 - \nu) \left( \frac{l_2}{R} \right)^2 \right] \quad (r > l_1 \text{ and } z = 0) \quad (2.53)$$

where  $l_2$ ,  $l_1$  and  $R$  are the radius of outer, inner ring and the disc, respectively.  $P$  represents applied load. For converting this solution from monolayer to multilayer, we have to consider the eq. (2.40) and (2.41) again. It is a must to satisfy the condition of biaxial stress  $\varepsilon_r = \varepsilon_\theta$  so,

$$\sigma_{ri} = \sigma_{\theta i} = E_i^p \varepsilon_r (1 + \nu_i) \quad (2.54)$$

In eq. (2.48)  $\nu_i = \nu$  is used for the neutral surface of multilayer discs, where  $\nu$  is the average Poisson's ratio and given by,

$$\nu = \nu_{avg} = \frac{1}{h_n} \sum_{i=1}^n \nu_i t_i \quad (2.55)$$

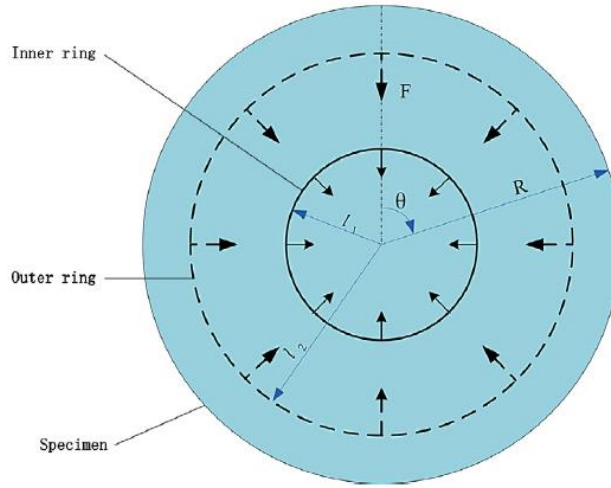


**Figure 2.28:** Schematic drawing on top view of ring-on-ring test.

So eq. (2.54) becomes,

$$\sigma_{ri} = \sigma_{\theta i} = E_i^p \varepsilon_r (1 + \nu) \quad (i = 1 \text{ to } n). \quad (2.56)$$

If we compare eq. (2.54) to (2.56), we realize that eq. (2.54) is more accurate. By multiplying eq. (2.56) with  $(1 + \nu_i) / (1 + \nu)$ , the stress distribution for multilayer discs can be express more accurately.

$$\sigma_{ri} = \sigma_{\theta i} = \frac{-E_i P (z - z_n^m)}{8\pi D^m (1 - \nu_i)} \left[ 2 \ln \left( \frac{l_2}{l_1} \right) + \frac{(1 - \nu)(l_2^2 - l_1^2)}{(1 + \nu)R^2} \right] \quad (r \leq l_1 \text{ and } i = 1 \text{ to } n) \quad (2.57)$$

$$\sigma_r = \frac{-E_i P (z - z_n^m)}{8\pi D^m (1 - \nu_i)} \left[ 2 \ln \left( \frac{l_2}{r} \right) + \frac{(1 - \nu)l_1^2 (l_2^2 - r^2)}{(1 + \nu)(rR)^2} \right] \quad (r > l_1 \text{ and } i = 1 \text{ to } n) \quad (2.58)$$



$$\sigma_{\theta} = \frac{-E_i P(z - z_n^m)}{8\pi D^m (1 - \nu_i)} \left[ 2 \ln \left( \frac{l_2}{r} \right) + \frac{(1 - \nu) l_1^2 (l_2^2 + r^2)}{(1 + \nu) (rR)^2} + \frac{2(1 - \nu)}{(1 + \nu)} \left( \frac{l_2}{R} \right)^2 \right] \quad (r > l_1 \text{ and } i = 1 \text{ to } n) \quad (2.59)$$

where  $D^m$  and  $z_n^m$  are obtained by eq. (2.44) and (2.45). Fracture cannot occur at any layer until the stress exceeds its tensile strength during test. Other biaxial flexure tests can be evaluated by this method for multilayer material like ring-on-ring test [73].



### 3. THIN FILM OPTICS

The magnitude of light beam that propagates one or more medium should be known. We apply boundary conditions to Maxwell Equation for that. These equations are so complicated and needs complex solutions. Thus, we use assumptions. In this section, brief information about thin film optics will be given.

#### 3.1. Absorbing Mediums

Equation of propagating light in permeable medium can be used in absorbing medium as well, if we use refractive index as complex number. The imaginary part is related to absorbance in medium. If we have a wave in a permeable medium that refractive index  $n$ , towards  $(\lambda, \mu, \nu)$  directions and rotational frequency  $\omega$ , so the field vector is shown in eq. (3.1),

$$E = E_0 \exp i \omega \left( t - \frac{n(\lambda x + \mu y + \nu z)}{c} \right) \quad (3.1)$$

where  $c$  is speed of light in vacuum.

In absorbing medium this equation evaluates,

$$E = E_0 \exp i \omega \left( t - \frac{\lambda(\lambda x + \mu y + \nu z)}{c} + \frac{i\beta(\lambda' x + \mu' y + \nu' z)}{c} \right) \quad (3.2)$$

where  $(\lambda', \mu', \nu')$  is the direction of maximum reduction (damping).

For a incident wave in normal direction,

$$E = E_0 \exp i \omega \left( t - \frac{(n - ik)(\lambda x + \mu y + \nu z)}{c} \right) \quad (3.3)$$

$\alpha$  and  $\beta$  from Eq. (3.2) are related to the direction of propagation and angle of incidence ( $\theta$ ).

$$\alpha^2 - \beta^2 = n^2 - k^2 \quad (3.4)$$

$$\alpha\beta\cos\varphi = nk \quad (3.5)$$

$$\sin\theta = \alpha\sin\varphi \quad (3.6)$$

These equations give the relation between  $\theta$ ,  $\varphi$  and  $n$ , also they are more detailed than Snell Law.

### 3.2. Transmittance and Reflectance in Permeable Medium

For an isotropic medium, electromagnetic laws represent these equations,

$$\text{div } D = \varepsilon \text{div } E = 4\pi\rho \quad (3.7)$$

$$\text{div } B = \mu \text{div } H = 0 \quad (3.8)$$

$$\text{curl } E = -\frac{\mu}{c} \frac{\partial E}{\partial t} \quad (3.9)$$

$$\text{curl } H = \frac{4\pi\sigma E}{c} + \frac{\varepsilon}{c} \frac{\partial E}{\partial t} \quad (3.10)$$

Propagation of electromagnetic waves in uncharged medium represent with Maxwell equations are given in eq. (3.11)-(3.14).

$$\frac{\varepsilon\mu}{c^2} \frac{\partial^2 E}{\partial t^2} + \frac{4\pi\mu\sigma}{c^2} \frac{\partial E}{\partial t} = \nabla^2 E \quad (3.11)$$

$$\frac{\varepsilon\mu}{c^2} \frac{\partial^2 E}{\partial t^2} + \frac{4\pi\mu\sigma}{c^2} \frac{\partial H}{\partial t} = \nabla^2 H \quad (3.12)$$

For non-conducting medium ( $\sigma = 0$ ) equations turns,

$$\frac{\varepsilon\mu}{c^2} \frac{\partial^2 E}{\partial t^2} = \nabla^2 E \quad (3.13)$$

$$\frac{\varepsilon\mu}{c^2} \frac{\partial^2 E}{\partial t^2} = \nabla^2 H \quad (3.14)$$

Waves propagates at speed of  $c/\sqrt{\mu\varepsilon}$ . Almost every material, value of  $\mu$  is nearly equals to unity at optical frequencies. Thus, the final speed turns into  $c/\sqrt{\varepsilon}$ .  $\varepsilon$  is the dielectric constant. By using refractive index, we obtain  $n = \sqrt{\varepsilon}$ . Finally, transmittance and reflectance are obtained by applying boundary conditions to Maxwell equations. Coordinate system is shown in Figure 3.1.  $E_{0p}^+$  and  $E_{0s}^+$ ,  $E_{0p}^-$  and  $E_{0s}^-$ ,  $E_{1p}^-$  and  $E_{1s}^-$  are the component of incident, reflected and transmitted wave, respectively.

$$\exp i \left( \omega t - \frac{2\pi n_0 x \sin \varphi_0}{\lambda} - \frac{2\pi n_0 z \cos \varphi_0}{\lambda} \right) \quad (3.15)$$

$$\exp i \left( \omega t - \frac{2\pi n_0 x \sin \varphi_0}{\lambda} + \frac{2\pi n_0 z \cos \varphi_0}{\lambda} \right) \quad (3.16)$$

However, the equation evaluates for propagating wave,

$$\exp i \left( \omega t - \frac{2\pi n_1 x \sin \varphi_0}{\lambda} - \frac{2\pi n_1 z \cos \varphi_0}{\lambda} \right) \quad (3.17)$$

where  $\lambda$  is the wavelength in vacuum.

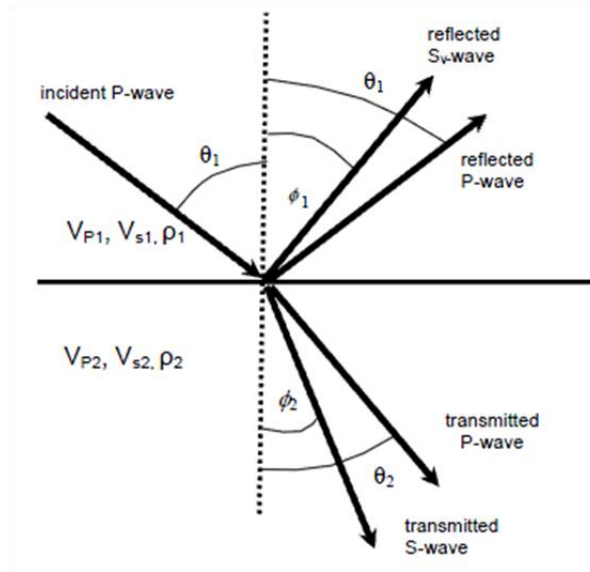


**Figure 3.1:** Incident, transmitted and reflected wave.

$$E_{0x} = (E_{0p}^+ + E_{0p}^-) \cos \varphi_0$$

$$E_{0y} = E_{0s}^+ + E_{0s}^-$$

$$H_{0x} = n_0 (-E_{0p}^+ + E_{0p}^-) \cos \varphi_0 \quad (3.18)$$

$$H_{0y} = n_0 (E_{0p}^+ + E_{0p}^-)$$

and for first medium,

$$E_{1x} = E_{1p}^+ \cos \varphi_1$$

$$E_{1y} = E_{1s}^+$$

$$H_{lx} = -n_1 E_{1s}^+ \cos \varphi_1 \quad (3.19)$$

$$H_{ly} = n_1 E_{1p}^+$$

If we apply boundary conditions for transmitted and reflected wave,

$$\frac{E_{0p}^-}{E_{0p}^+} = \frac{n_0 \cos \varphi_1 - n_1 \cos \varphi_0}{n_0 \cos \varphi_1 + n_1 \cos \varphi_0} = r_{1p} \quad (3.20)$$

$$\frac{E_{1p}^+}{E_{0p}^+} = \frac{2n_0 \cos \varphi_0}{n_0 \cos \varphi_1 + n_1 \cos \varphi_0} = t_{1p} \quad (3.21)$$

$$\frac{E_{0s}^-}{E_{0s}^+} = \frac{n_0 \cos \varphi_0 - n_1 \cos \varphi_1}{n_0 \cos \varphi_0 + n_1 \cos \varphi_1} = r_{1s} \quad (3.22)$$

$$\frac{E_{1s}^+}{E_{0s}^+} = \frac{2n_0 \cos \varphi_0}{n_0 \cos \varphi_0 + n_1 \cos \varphi_1} = t_{1s} \quad (3.23)$$

where  $r_{1p}$ ,  $r_{1s}$  and  $t_{1p}$ ,  $t_{1s}$  are the coefficients of Fresnel reflectance and transmittance, respectively. We need these coefficients to solve multilayer systems. From eq. (3.20) - (3.23) we obtain,

$$t_{1p} = 1 + r_{1p}$$

$$t_{1s} = 1 + r_{1s}$$

and if  $n_0 > n_1$ ,  $t_{1p}$  and  $t_{1s}$  approach to 1. Figure 3.2 shows the reflectivity values for different incident angle.

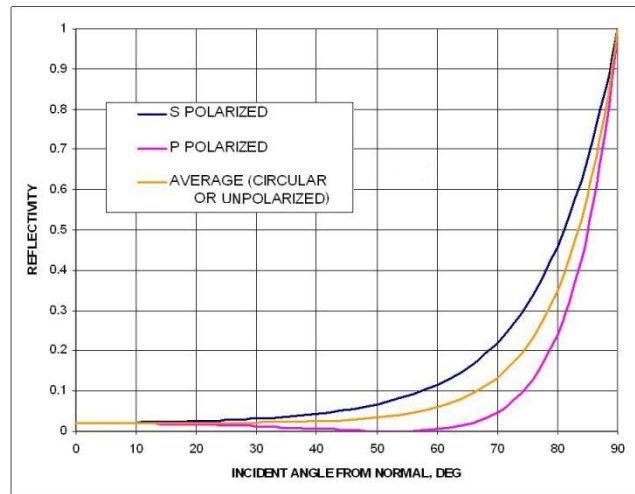


**Figure 3.2:** Reflectivity values.

Poynting vector represents with  $S$  and if we apply energy conservation and Poynting law,

$$|S| = \frac{c}{4\pi} [E \times H] \quad (3.24)$$

$$|S| = \frac{c}{4\pi} n [E]^2 \quad (3.25)$$

Therefore reflectance,

$$R_p = \frac{(E_{0p}^-)^2}{(E_{0p}^+)^2} = r_{1p}^2 \quad (3.26)$$

$$R_s = \frac{(E_{0s}^-)^2}{(E_{0s}^+)^2} = r_{1s}^2$$

and transmittance,

$$T_p = \frac{n_1 (E_{1p}^+)^2}{n_0 (E_{0p}^+)^2} = \frac{n_1}{n_0} t_{1p}^2 \quad (3.27)$$

$$T_s = \frac{n_1 (E_{1s}^+)^2}{n_0 (E_{0s}^+)^2} = \frac{n_1}{n_0} t_{1s}^2$$

For an incident normal wave, transmittance and reflectance values are,

$$R_p = R_s = \left( \frac{n_0 - n_1}{n_0 + n_1} \right)^2 \quad (3.28)$$

$$T_p = T_s = \frac{4n_0 n_1}{(n_0 + n_1)^2} \quad (3.29)$$

If we apply Snell Law, we obtain Fresnel coefficients,

$$r_{1p} = \frac{\tan(\varphi_1 - \varphi_0)}{\tan(\varphi_1 + \varphi_0)} \quad (3.30)$$

$$r_{1s} = \frac{\sin(\varphi_1 - \varphi_0)}{\sin(\varphi_1 + \varphi_0)} \quad (3.31)$$

$$t_{Ip} = \frac{2\sin\varphi_1\cos\varphi_0}{\sin(\varphi_1+\varphi_0)\cos(\varphi_1-\varphi_0)} \quad (3.32)$$

$$t_{Ip} = \frac{2\sin\varphi_1\cos\varphi_0}{\sin(\varphi_1+\varphi_0)} \quad (3.33)$$

These equations are very popular for a layer but not so much for multilayers.

### 3.3. Reflection at Surface of Absorbing Medium

As done in previous section, we can obtain propagation equations in absorbing medium by using complex refractive index. Thus, Eq. (3.20)-(3.23) evaluates,

$$\sin\varphi_I = \frac{n_0\sin\varphi_0}{n_1-ik_1} \quad (3.34)$$

So  $\varphi_I$  becomes complex and does not represent refractive index unless  $\varphi_0 = \varphi_I = 0$ . This is a special condition that we can easily find Fresnel refractive coefficients.

$$r_{Ip} = r_{Is} = \frac{n_0-n_1+ik_1}{n_0+n_1-ik_1} \quad (3.35)$$

$$R_p = R_s = \frac{(n_0-n_1)^2+k_1^2}{(n_0+n_1)^2+k_1^2} \quad (3.36)$$

Except normal incident, reflection term becomes too complicated and needs assumption. Major part of absorbing materials, especially metals, shows  $n^2 + k^2 \gg 1$  in visible spectrum. With this assumption,

$$R_p = \frac{(n^2+k^2)\cos^2\varphi_0-2n\cos\varphi_0+1}{(n^2+k^2)\cos^2\varphi_0+2n\cos\varphi_0+1} \quad (3.37)$$

$$R_s = \frac{(n^2+k^2)-2n\cos\varphi_0+\cos^2\varphi_0}{(n^2+k^2)+2n\cos\varphi_0+\cos^2\varphi_0} \quad (3.38)$$

We obtain eq. (3.36) and (3.37). The Fresnel transmittance coefficients are non-effective by the interaction between the amplitude of wave and propagation in absorbing medium. Figure 3.3 shows reflected and transmitted rays. So complex Fresnel transmittance coefficients are,

$$r_{ip} = \sigma_{ip}e^{i\beta_{1p}} \quad (3.39)$$



$$r_{is} = \sigma_{is} e^{i\beta_{1s}} \quad (3.40)$$

where  $\sigma_{ip}$ ,  $\sigma_{is}$  are the amplitude of reflected waves and  $\beta_{1p}$ ,  $\beta_{1s}$  represent phase transformation at the surface.  $\sigma$  and  $\beta$  values represents as,

$$\frac{1+\sigma e^{i\beta}}{1-\sigma e^{i\beta}} = \frac{\sin\varphi_0 \tan\varphi_0}{[(n-ik)^2 - \sin^2\varphi_0]^{1/2}} \quad (3.41)$$

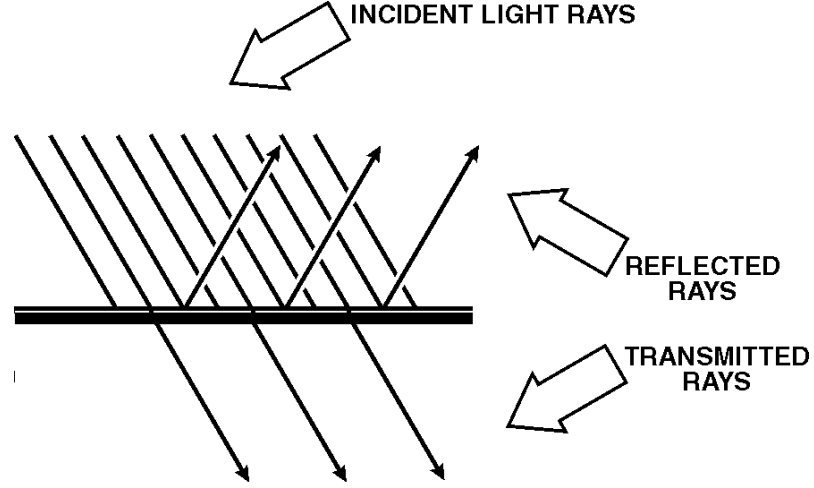


**Figure 3.3:** Light waves reflected and transmitted.

### 3.4. Transmittance and Reflectance of Single Layer

We can use results that obtained in section (3.3) to evaluate transmittance coefficients for non-absorbing single layer, which is limited by half infinitive non-absorbing mediums at both sides. Incident light beam is separated to reflected and transmitted parts. We pile up both parts separately and this method is very useful for single layer. Results are represents via Fresnel coefficients.

Fresnel coefficients from Eq. (3.20)-(3.23) will be represented as  $r_l$ ,  $t_l$  for propagation  $n_0$  to  $n_l$ ;  $r'_l$  and  $t'_l$  for propagation  $n_l$  to  $n_0$ . Since, these coefficients are hold for both directions of polarization; it gives appropriate values to  $r$  and  $t$ . Thus, Second index (p or s) will be ignored. From Fresnel reflectance coefficients, we can evaluate that  $r'_1$  equals to  $-r'_1$ . So, the amplitude of reflected consecutive rays are represented as  $r_l$ ,  $t_l t'_1 r_2$ ,  $-t_l t'_1 r_1 r_2^2$ ,  $t_l t'_1 r_1^2 r_2^3$ , ... and transmitted consecutive rays are represented as  $t_l t_2$ ,  $-t_l t_2 r_1 r_2$ ,  $t_l t_2 r_1^2 r_2^2$ , ... .  $\delta_l$  is the phase transition of transmitted rays,

$$\delta_I = \frac{2\pi}{\lambda} n_1 d_1 \cos \varphi_1 \quad (3.42)$$

so, the reflected amplitude,

$$R = r_I + t_I t_1' r_2 e^{-2i \delta_1} - t_I t_1' r_I r_2^2 e^{-4i \delta_1} + \dots$$

$$R = r_I + \frac{t_1 t_1' r_2 e^{-2i \delta_1}}{1 + t_1 t_1' r_2 e^{-2i \delta_1}} \quad (3.43)$$

This term is independent of time. For non-absorbing mediums, representing Fresnel transmittance coefficients is easier with  $r_1$  and  $r_2$  terms. From energy conservation and Eq. (3.20) and (3.23),

$$t_I t_1' = -r_2^2 \quad (3.44)$$

so, Eq. (3.42) evaluates,

$$R = \frac{r_1 + r_2 e^{-2i \delta_1}}{1 + r_1 r_2 e^{-2i \delta_1}} \quad (3.45)$$

and the amplitude of transmitted rays are given in eq. (3.46),

$$T = t_I t_2 e^{-i \delta_1} - t_I t_2 r_I r_2 e^{-3i \delta_1} + t_I t_2 r_1^2 r_2^2 e^{-5i \delta_1} - \dots$$

$$T = \frac{t_1 t_2 e^{-i \delta_1}}{1 + r_1 r_2 e^{-2i \delta_1}} \quad (3.46)$$

Eq. (3.45) and (3.46) are general. For not normal incident, there are two possibilities due to polarization of incident light. For parallel coefficient Eq. (3.20) and (3.21) are used; for perpendicular coefficient Eq. (3.22) and (3.23) are used.

If the layer is absorbing or is limited by absorbing mediums, we use complex values for  $n_0$ ,  $n_1$ , and  $n_2$ . Thus, Fresnel coefficients become complex and calculating  $R$  and  $T$  values become complicated. The total energy of rays,

$$n_0 R R^* = \frac{n_0 (r_1^2 + 2r_1 r_2 \cos 2\delta_1 + r_2^2)}{(1 + 2r_1 r_2 \cos 2\delta_1 + r_1^2 r_2^2)} \quad (3.47)$$

$$n_2 T T^* = \frac{n_2 t_1^2 t_2^2}{(1 + 2r_1 r_2 \cos 2\delta_1 + r_1^2 r_2^2)} \quad (3.48)$$

then reflectance and transmittance evaluates to eq. (3.49) and (3.50),

$$R = \frac{r_1^2 + 2r_1r_2\cos 2\delta_1 + r_2^2}{1 + 2r_1r_2\cos 2\delta_1 + r_1^2r_2^2} \quad (3.49)$$

$$T = \frac{n_2}{n_0} \frac{t_1^2 t_2^2}{1 + 2r_1r_2\cos 2\delta_1 + r_1^2r_2^2} \quad (3.50)$$

From Eq. (3.20) - (3.23) Fresnel coefficients,

$$r_I = \frac{n_0 - n_1}{n_0 + n_1} \quad \text{and} \quad t_I = \frac{2n_0}{n_0 + n_1} \quad (3.51)$$

$$r_2 = \frac{n_1 - n_2}{n_1 + n_2} \quad \text{and} \quad t_2 = \frac{2n_2}{n_1 + n_2} \quad (3.52)$$

so, Eq. (3.45) and (3.46) becomes,

$$R = \frac{(n_0 - n_1)(n_1 + n_2)e^{i\delta_1} + (n_0 + n_1)(n_1 - n_2)e^{-i\delta_1}}{(n_0 + n_1)(n_1 + n_2)e^{i\delta_1} + (n_0 - n_1)(n_1 - n_2)e^{-i\delta_1}} \quad (3.53)$$

$$T = \frac{4n_0n_1}{(n_0 + n_1)(n_1 + n_2)e^{i\delta_1} + (n_0 - n_1)(n_1 - n_2)e^{-i\delta_1}} \quad (3.54)$$

and finally reflectance and transmittance is given by eq. (3.55) and (3.56),

$$R = \frac{(n_0^2 + n_1^2)(n_1^2 + n_2^2) - 4n_0n_1^2n_2 + (n_0^2 - n_1^2)(n_1^2 - n_2^2)\cos 2\delta_1}{(n_0^2 + n_1^2)(n_1^2 + n_2^2) + 4n_0n_1^2n_2 + (n_0^2 - n_1^2)(n_1^2 - n_2^2)\cos 2\delta_1} \quad (3.55)$$

$$T = \frac{8n_0n_1^2n_2}{(n_0^2 + n_1^2)(n_1^2 + n_2^2) + 4n_0n_1^2n_2 + (n_0^2 - n_1^2)(n_1^2 - n_2^2)\cos 2\delta_1} \quad (3.56)$$

These terms can be easily evaluated for non-absorbing mediums. If the film or the limiting mediums are absorbing, then we should change  $n_0$ ,  $n_1$  and  $n_2$  values to  $n = n - ik$ .

In this section, we have tried to obtain optical constants of film by transmittance relation. We have measured transmittance due to wavelength and we have already known the refractive index of substrate and air, so we can calculate the refractive index, absorbing and damping coefficients of film.



#### 4. EXPERIMENTAL PROCEDURES

Two types of glass substrates were used in these experiments. Indented (300 g for 5 seconds) glass and Corning glass 2947 were used for the mechanical and the optical characterizations, respectively. Figure 4.1 shows the glass substrate for mechanic tests.



**Figure 4.1:** Uncoated glass substrates for the mechanical tests (8 x 8 mm plain, thickness: 3.2 mm).

Corning glass substrates has approximately 89% transparency at visible light spectrum. Figure 4.2 shows coated glass substrate.



**Figure 4.2:** Ta<sub>2</sub>O<sub>5</sub> thin film coated Corning glass 2947 (7.62x2.54 mm plain, thickness: 1mm).

Titanium oxide and silicon oxide (TiO<sub>2</sub> – SiO<sub>2</sub>) binary films were deposited by spin coater at 1500 rpm for 60 seconds. Tantalum pentoxide (Ta<sub>2</sub>O<sub>5</sub>) thin films were coated on the glass substrates at 1000 rpm for 60 seconds. All as-deposited films were heated at 120 °C for 30 minutes. Each prepared sols were dried at 150 °C on the magnetic stirrer in order to get powder forms. Later, heat treatment was applied the obtained powders at 450 °C for 1 hour as calcination process.

#### 4.1. Cleaning Procedure of Glass Substrates

Cleanliness of glass substrates surface is key element for the quality of coating. If any contamination exists, it negatively affects both the optical and the mechanical properties. Prior to the deposition of film on the glass substrate, the substrates were first flushed with a liquid detergent and then washed with de-ionized water. Next, the surface is washed ultrasonically in acetone, methanol and ethanol, respectively.

#### 4.2. Preparation of Sols

Two different recipes were used for  $\text{TiO}_2 - \text{SiO}_2$  binary system. The first one, which was developed by Şişecam Company, was obtained and used directly. The ratio of  $\text{TiO}_2$  to  $\text{SiO}_2$  is 5%. Figure 4.3 shows preparation process of traditional titanium dioxide sol.

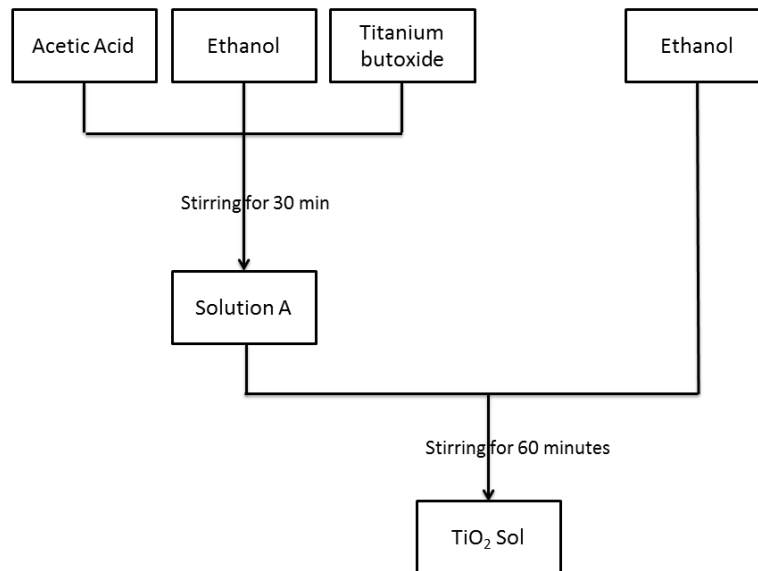


**Figure 4.3:** Preparation of traditional  $\text{TiO}_2$  sol.

On the other hand, the well-known flowchart of  $\text{TiO}_2 - \text{SiO}_2$  in the literature was also used.  $\text{TiO}_2$  sol was prepared by adding 180  $\mu\text{l}$  acetic acid ( $\text{CH}_3\text{OOH}$ ) to 15 ml ethanol ( $\text{C}_2\text{H}_5\text{OH}$ ), after that 1.2 ml titanium (IV) butoxide ( $\text{Ti}(\text{OCH}_2\text{CH}_2\text{CH}_2\text{CH}_3)_4$ ) was added to mixture very slowly and stirred for 30 minutes. Eventually, 10 ml ethanol was added and stirred for 60 minutes.

$\text{SiO}_2$  sol was prepared by stirring 5 ml tetraethyl orthosilicate ( $\text{Si}(\text{OC}_2\text{H}_5)_4$ ), 55 ml isopropyl alcohol ( $\text{C}_3\text{H}_8\text{O}$  or  $\text{C}_3\text{H}_7\text{OH}$ ), 12 ml hydrochloric acid ( $\text{HCl}$ ) and 0.5 ml distilled water for 20 minutes at  $70^\circ\text{C}$ . After that, the mixture was stirred for 60

minutes at room temperature. The ratio of  $\text{TiO}_2$  to  $\text{SiO}_2$  is 50% by volume. Figure 4.4 shows preparation process of traditional silicon dioxide sol.

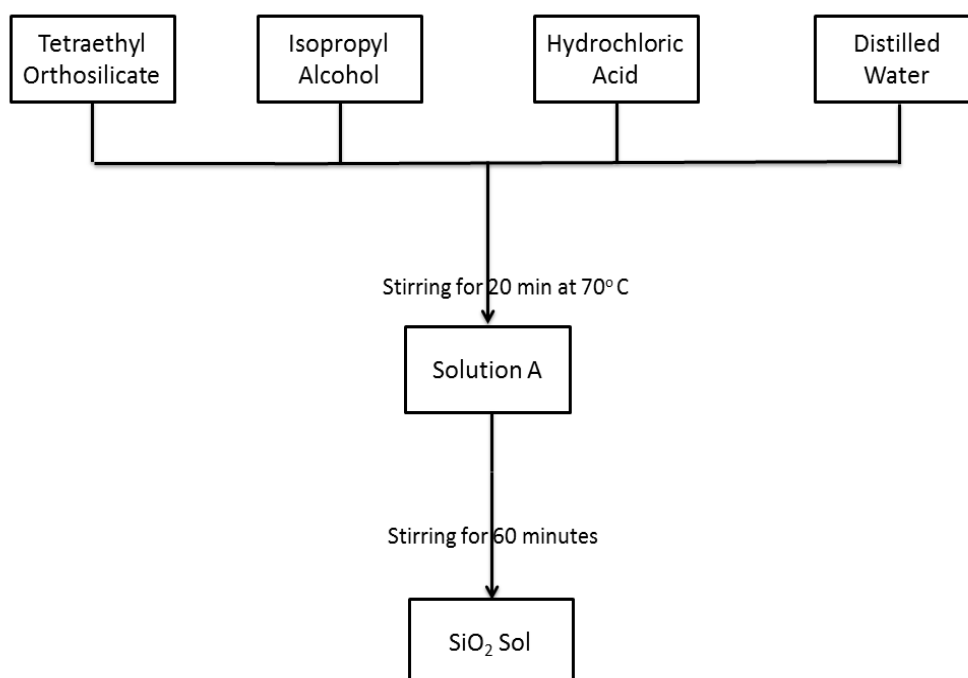


**Figure 4.4:** Preparation of  $\text{SiO}_2$  sol.

For  $\text{Ta}_2\text{O}_5$  sol, 35 ml ethanol and 0.5 ml acetic acid were stirred in first beaker and then 1.8 ml tantalum ethoxide ( $\text{Ta}_2(\text{OC}_2\text{H}_5)_5$  and 99.98% pure) which was obtained from Sigma-Aldrich Co. LLC. and used without any purification, was poured into this solution and stirred for 30 minutes. Meanwhile in second beaker 15 ml pure water and 0.5 ml acetic acid were stirred for a while. 0.75 ml of second beaker solution was added into third beaker with 7.5 ml ethanol and were stirred for 20 minutes. 2.5 ml of third beaker solution was added into first beaker and were stirred for 18 hours slowly with magnetic stirrer. Figure 4.5 shows the preparation process of tantalum pentoxide sol.

Cerium nanoparticles were used directly without any purification process. SWCNTs (purity 98.3% and diameter  $\sim 1$  nm, produced via CVD and purified via 6 molar  $\text{HNO}_3$  for 6 hours) were dissolved in N-Methyl-2-pyrrolidone (NMP) and stirred for one hour in ultrasonic cleaner.

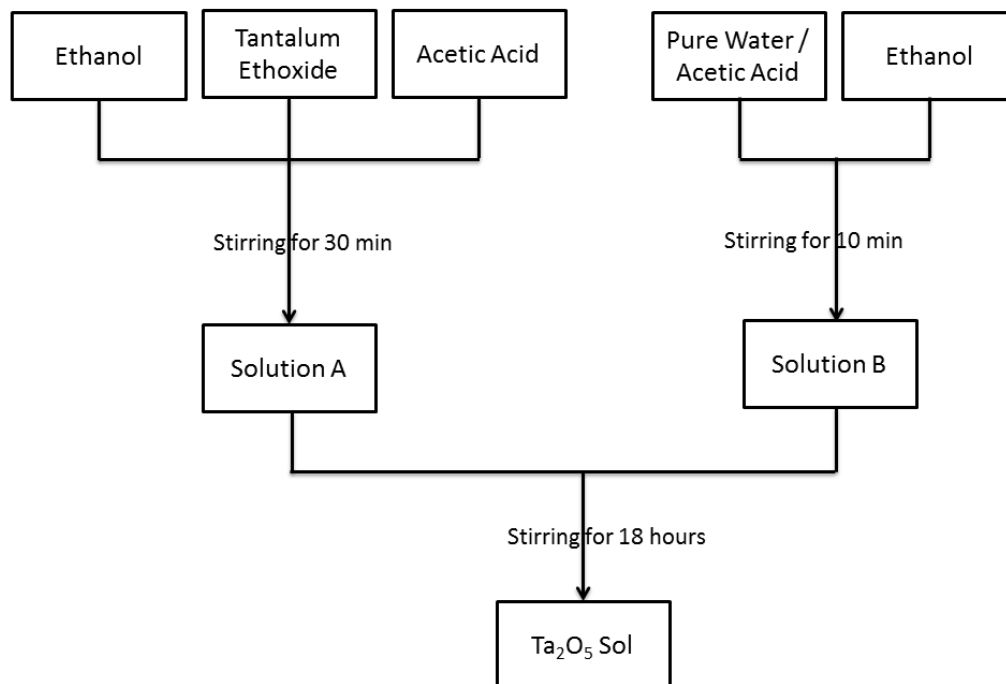


**Figure 4.5:** Preparation of Ta<sub>2</sub>O<sub>5</sub> sol.

### 4.3. Preparation of Films

All films were deposited on glass substrates by a sol-gel technique. The films were prepared on glass substrates by spin and dip coating. Tantalum pentoxide films are deposited at 1000 rpm; titanium and silicon dioxide binary films are deposited at 1500 rpm for 60 seconds by spin coater. All as-deposited films were heated at 120 °C for 30 minutes in order to get film formation on the glass substrates.



## 5. RESULTS

In this section, all gathered data are listed and compared to each other. For mechanical properties of the deposited films, analytical calculations, finite element method and experimental results were obtained separately and the obtained results of every method was compared and discussed. It is obvious that experimental data is the most trustable and useful one. However, it is impossible to try out every possibility for design and material selection. Therefore, we need analytical solutions and computer simulations. Especially computer simulations, which use FEM like Ansys, give promising results for understanding behavior of materials.

XRD and XPS were used for phase characterization and chemical composition. SEM, AFM and optical microscopy were used to examine surface properties of thin films. UV-vis and NKD analyzer were used to obtain transmittance and reflectance curves of films as a function of wavelength. Profilometer was used to measure the thickness on films. Tensiometer was used to examine contact angle of film surfaces.

### 5.1. Analytical Solution Results

Mechanical properties of materials have to be known in order to calculate final structure's behavior. Table 5.1 shows some mechanical properties of glass substrates and metal oxides [79].

**Table 5.1:** Mechanical property of various oxide films and glass substrate.

<b>Material</b>	<b>Young's Modulus (GPa)</b>	<b>Poisson's Ratio</b>	<b>Yield Strength (MPa)</b>
Glass Substrate	70	0,22	70
TiO <sub>2</sub>	250	0,27	340
Ta <sub>2</sub> O <sub>5</sub>	140	0,23	300
SiO <sub>2</sub>	73	0,17	100

All materials are assumed isotropic during analytical calculations. The thickness of glass substrate and the deposited film are  $t_g = 3.2 \text{ mm}$  and  $t_f = 10^{-3} \text{ mm}$ , respectively.

$D^m$  and  $Z_n^m$  values are obtained from eq. (2.44) and (2.45). Herein, the stress distribution upon the glass substrate and the obtained film were calculated easily from eq. (2.57)-(2.59). The radial and tangential stresses are equal where  $r \leq l_f$ . Total magnitude of stress is decreased while increasing  $r$  value. Table 5.2 shows the interaction between the applied force (P) and the stress ( $\sigma$ ).

**Table 5.2:** Interaction between P and  $\sigma$ .

<b>TiO<sub>2</sub>-SiO<sub>2</sub></b>		<b>Ta<sub>2</sub>O<sub>5</sub></b>	
Samples	$\sigma_r = \sigma_\theta$ (MPa)	Samples	$\sigma_r = \sigma_\theta$ (MPa)
Glass Substrate	-0.04839P	Glass Substrate	-0.04831P
Film	-0.05144P	Film	-0.09841P

In overall, tantalum pentoxide coated films diminishes the stress within the glass substrate in order to resist extra external forces. Hence, tantalum pentoxide coated films can be used in many applications. Moreover, the inorganic materials such as tantalum pentoxide can be eliminated the negative effects (degradation, corrosion, etc.) of sunshine on the materials.

Typical glasses have approximately same yield and ultimate strength that is around  $70 \text{ MPa}$ . Therefore, the glass substrate should stand up to,

$$\sigma_r = \sigma_\theta = 70 = -0,04839 P,$$

$$P = -1446,579 N$$

Herein, negative sign represents compression force. The same calculations were used to obtain other samples' ultimate forces and their results are given in the Table 5.3.

**Table 5.3:** Ultimate forces for various materials.

Samples	Ultimate Force (N)
Uncoated Glass	1446
TiO <sub>2</sub> + SiO <sub>2</sub>	2177
Ta <sub>2</sub> O <sub>5</sub>	3048

## 5.2. Finite Element Method (FEM) Results

Ansysis is an engineering simulation software, which uses finite element method. Besides, it gives nearly perfect results for analyzing substrates and thin films under external loads. Table 5.4. shows the results of uncoated and coated glass substrates separately.

FEM methodology provided an effective means to explore and predict the behavior of high-performance thin film systems. The use of FEM design could reduce the total number of experimental trials, while still maintaining high accuracy of analysis. The identification of the critical process factors via a screening experiment was essential for method optimization and resulted in a reduced number of system components greatly simplifying the technological process.

**Table 5.4:** FEM results of the samples.

Samples	Deflection (mm)	Ultimate Stress (MPa)
Glass substrate	0.215	74.4
TiO <sub>2</sub> -SiO <sub>2</sub>	0.307	145.3
Ta <sub>2</sub> O <sub>5</sub>	0.437	205.6

These are the evaluated results of uncoated and coated glass substrates. Figures 5.1-5.6 show the detailed information about stress distribution and deflection. Comparison of the results in Figure 5.3 and Figure 5.5, the stress distribution is more uniform for Ta<sub>2</sub>O<sub>5</sub> coated samples. It is the main reason why tantalum oxide films withstand more forces that are external. Uncoated glass substrates shows non-uniform distribution, which causes failure at low loads as shown in Figure 5.1. The middle point of the glass substrates shows maximum deflection due the position of the indenter ring.

Figure 5.1 and 5.2 show the stress distribution and the deflection of uncoated glass substrate, respectively.

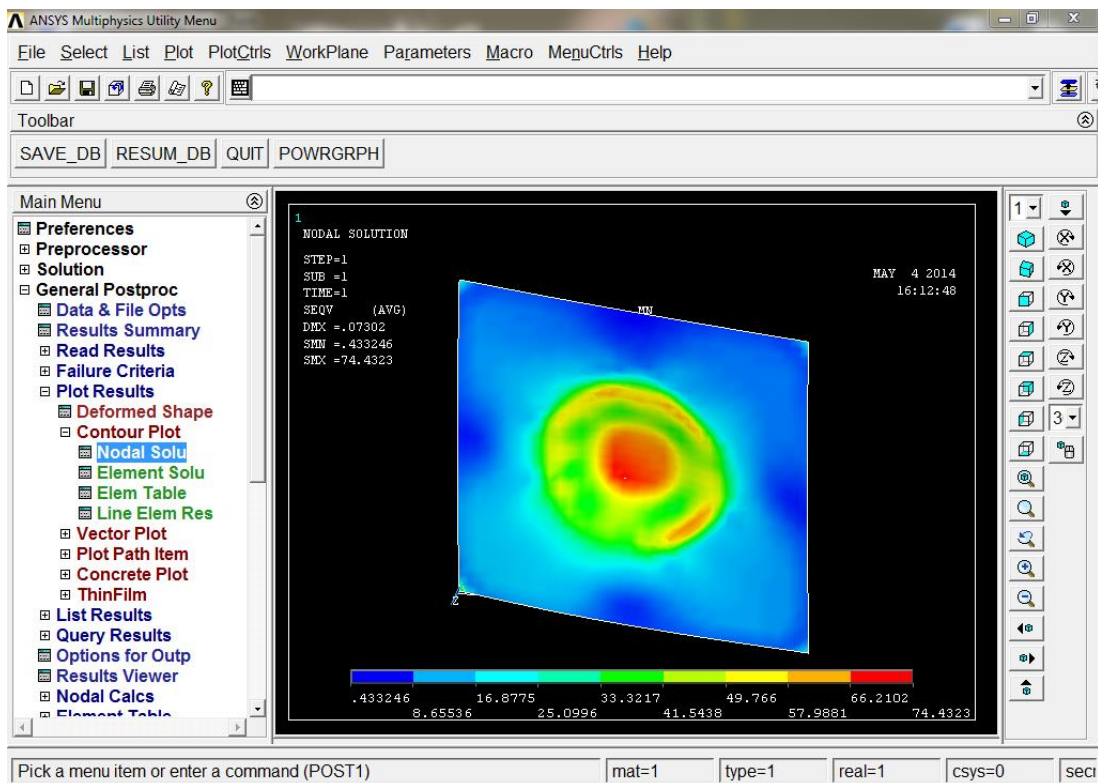


Figure 5.1: Stress distribution of glass substrate.

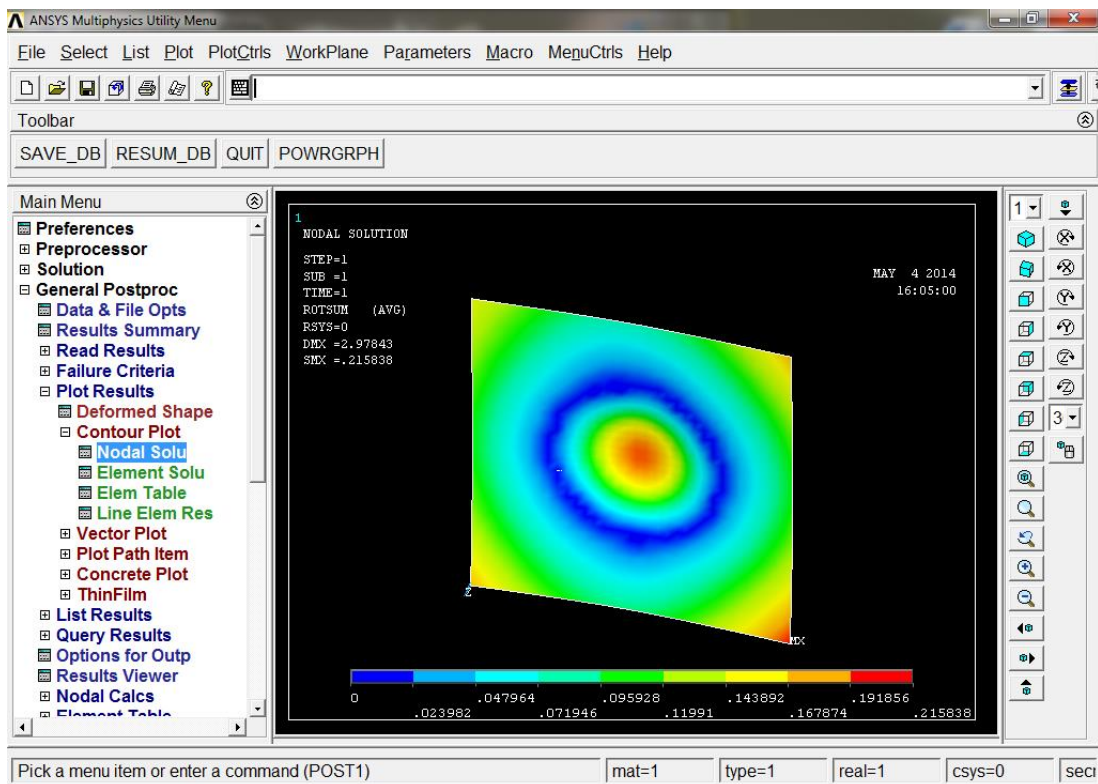
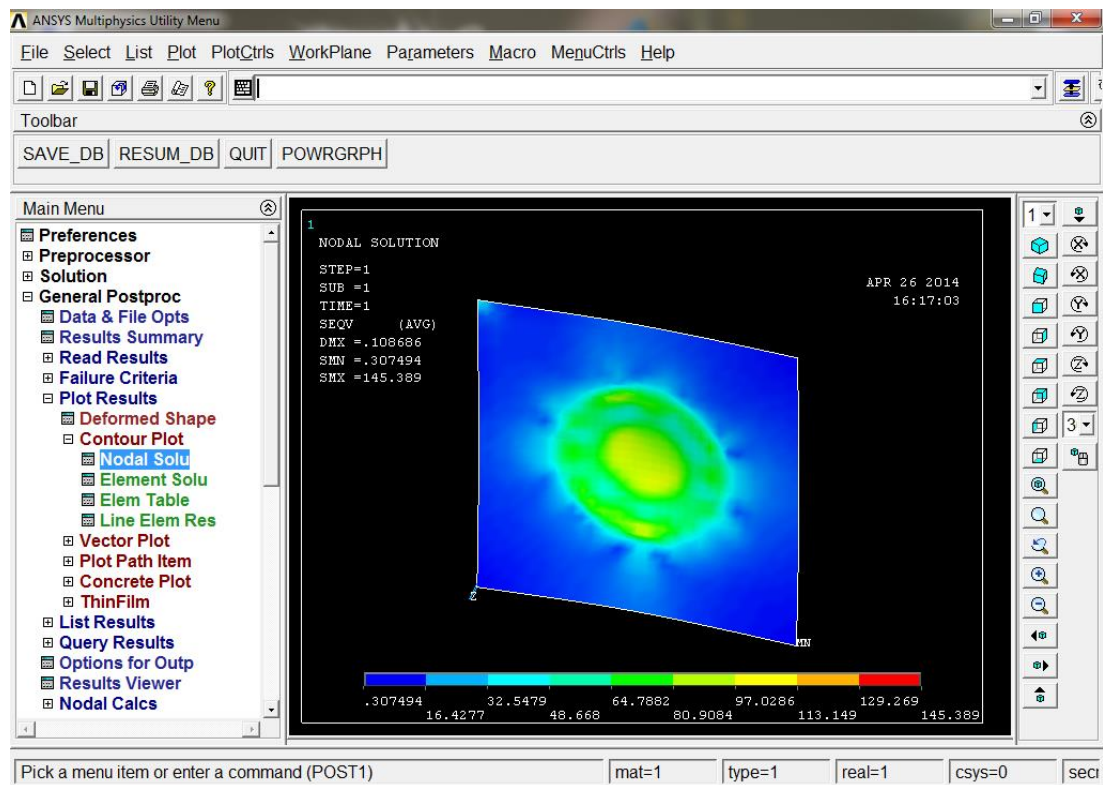
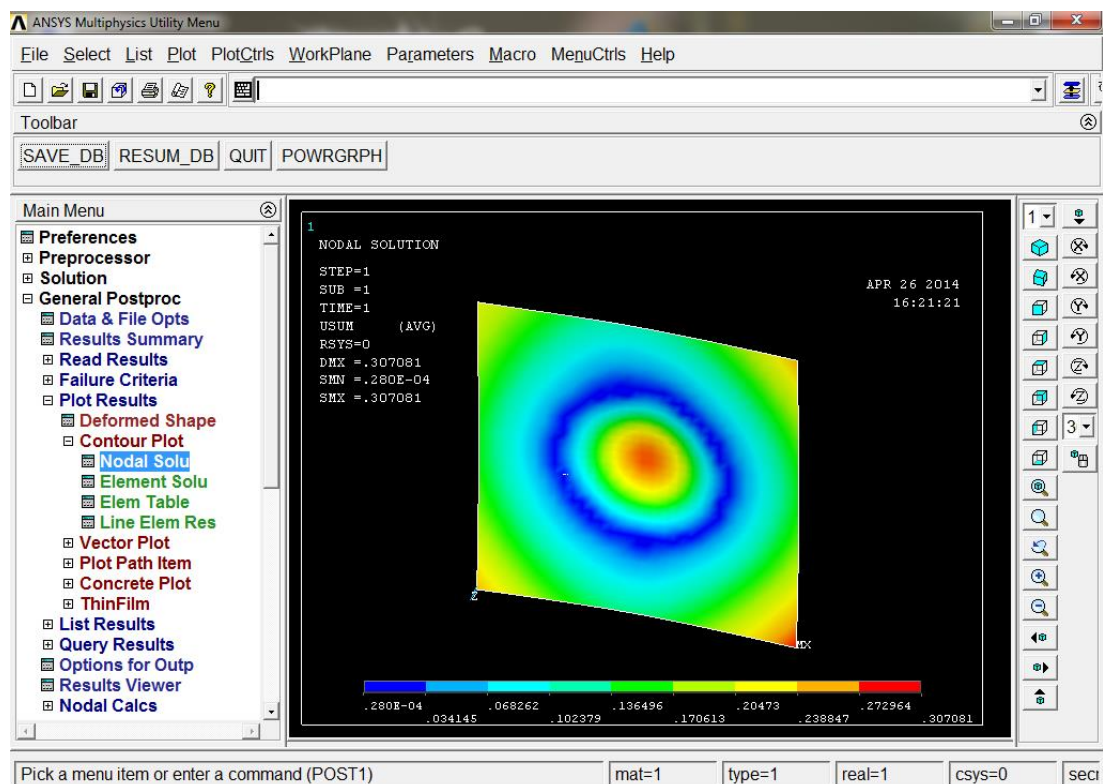


Figure 5.2: Deflection of glass substrate.

Figure 5.3 and 5.4 show the stress distribution and the deflection of  $\text{TiO}_2 - \text{SiO}_2$  thin film coated glass substrate, respectively.



**Figure 5.3:** Stress distribution of  $\text{TiO}_2 - \text{SiO}_2$  coated glass substrate.



**Figure 5.4:** Deflection of  $\text{TiO}_2 - \text{SiO}_2$  coated glass substrate.

Figure 5.5 and 5.6 show the stress distribution and the deflection of Ta<sub>2</sub>O<sub>5</sub> thin film coated glass substrate, respectively.

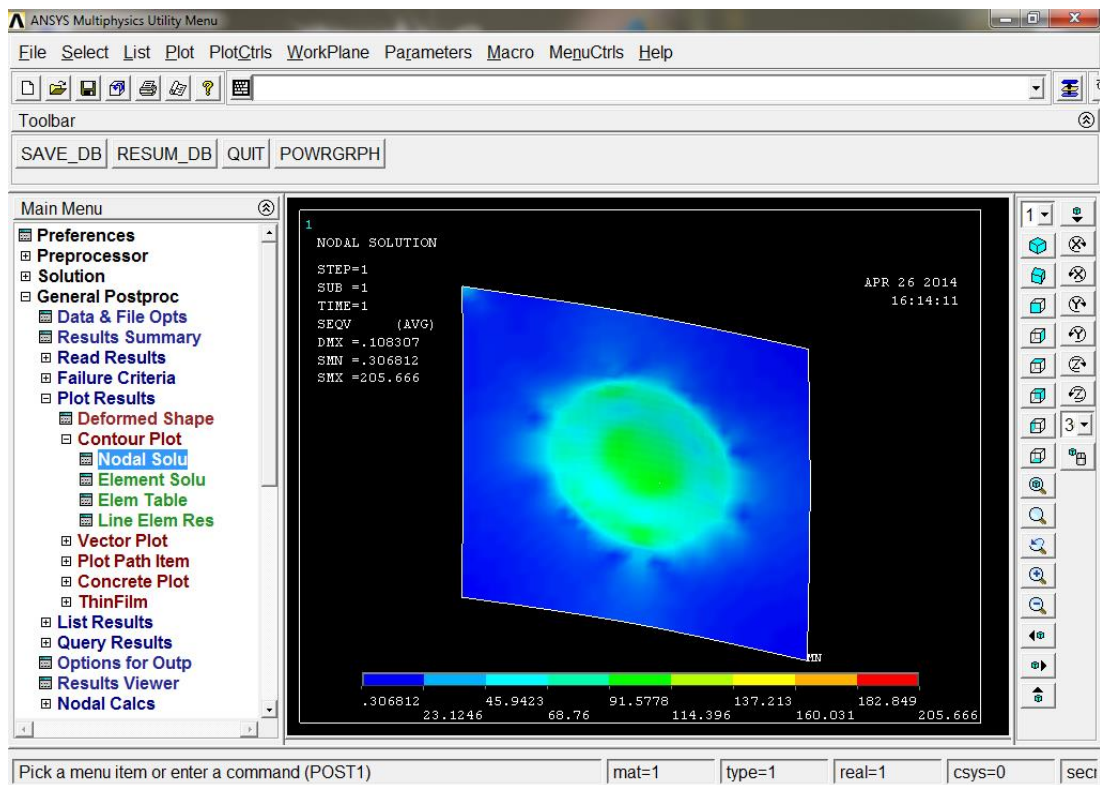


Figure 5.5: Stress distribution of Ta<sub>2</sub>O<sub>5</sub> coated glass substrate.

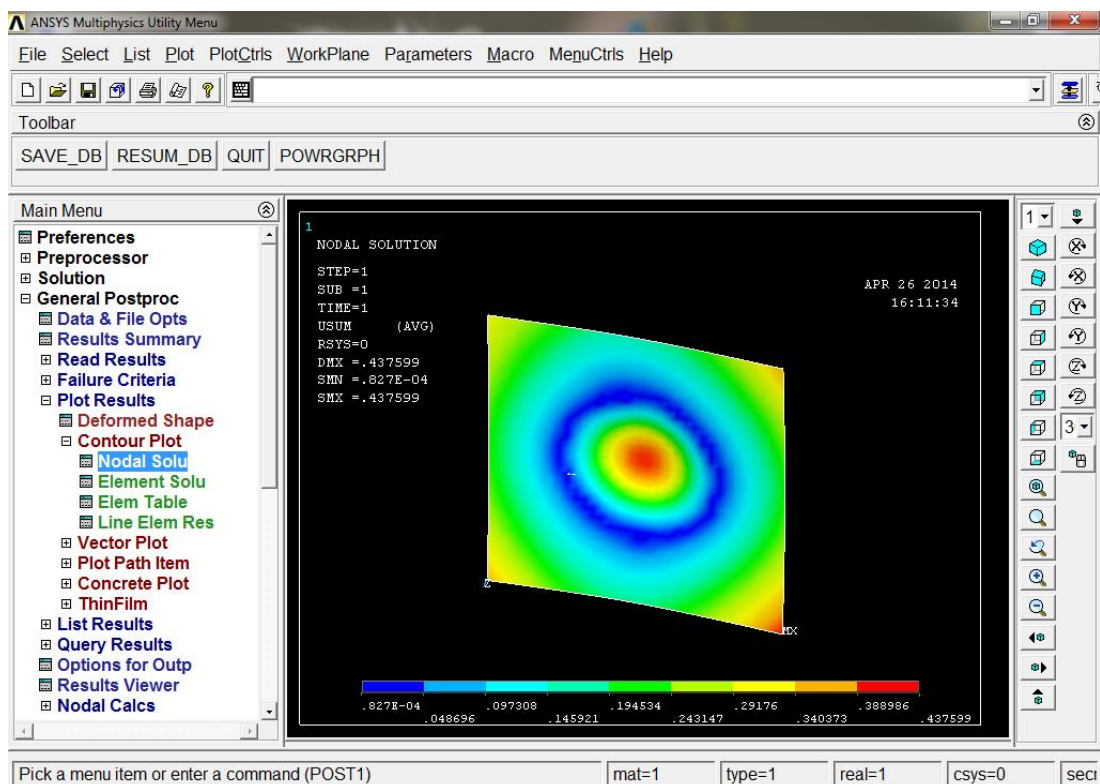


Figure 5.6: Deflection of Ta<sub>2</sub>O<sub>5</sub> coated glass substrate.



### 5.3. Experimental Results

Table 5.5 shows experimental results that obtained from ring-on-ring and scratch tests for various coatings. Fortunately, theoretical and experimental results of uncoated glass substrates are quite similar. However, there is a reasonable difference between theoretical and experimental results of the deposited films up to 30%. The main reason for difference is the mechanical properties that alter from nano to bulk form. There are other parameters that affect film's final structure and behavior too:

- Inclusion, impurities in the solutions,
- Inadequate or imperfect chemical transformation,
- Residual stresses among film structure,
- Imperfect bonding between substrate and thin film,
- Internal micro cracks,
- Imperfect gelation process and phase transformation.

Traditional recipe of  $\text{TiO}_2$  -  $\text{SiO}_2$  leads very frustrating results. Şişecam's recipe shows promising results, although the ratio of  $\text{TiO}_2$  to  $\text{SiO}_2$  is 5:95 in volume. Additionally, there is reasonable difference in spin coated and dip coated samples. The method affects final film thickness directly, so dip coated samples have thicker film that leads better mechanical results.

$\text{Ta}_2\text{O}_5$  thin films represent the best results. They demonstrated around 200% improvement for ultimate strength and huge increase in scratch resistance. However, the preparation process of tantalum pentoxide film is very critical. We could not achieve the same success when the powder form of tantalum ethoxide was used as precursor. Figure 5.7 shows image of coated glass substrate after ring-on-ring test.



**Figure 5.7:** Broken glasses with different coatings and three different failure types.

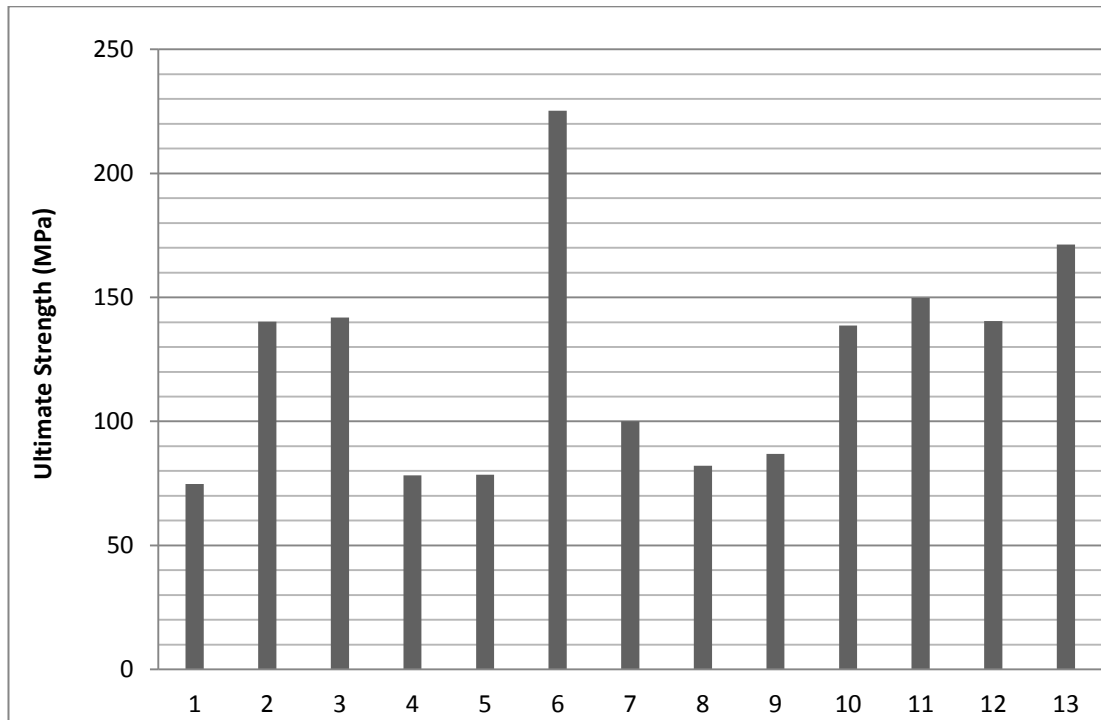
Adding CeO<sub>2</sub> nano particles to TiO<sub>2</sub> – SiO<sub>2</sub> binary sol gave poor results in terms of the mechanical properties. SWCNT shows some improvement especially on hardness. Very small amount of SWCNT leads 7% improvement on ultimate strength and 100% on hardness. Nevertheless, the positive effects of SWCNT decreases by increasing content. Table 5.5 shows experimental results that obtained from ring-on-ring and scratch tests for various coatings.

**Table 5.5:** Experimental results obtained from ring-on-ring and scratch tests.

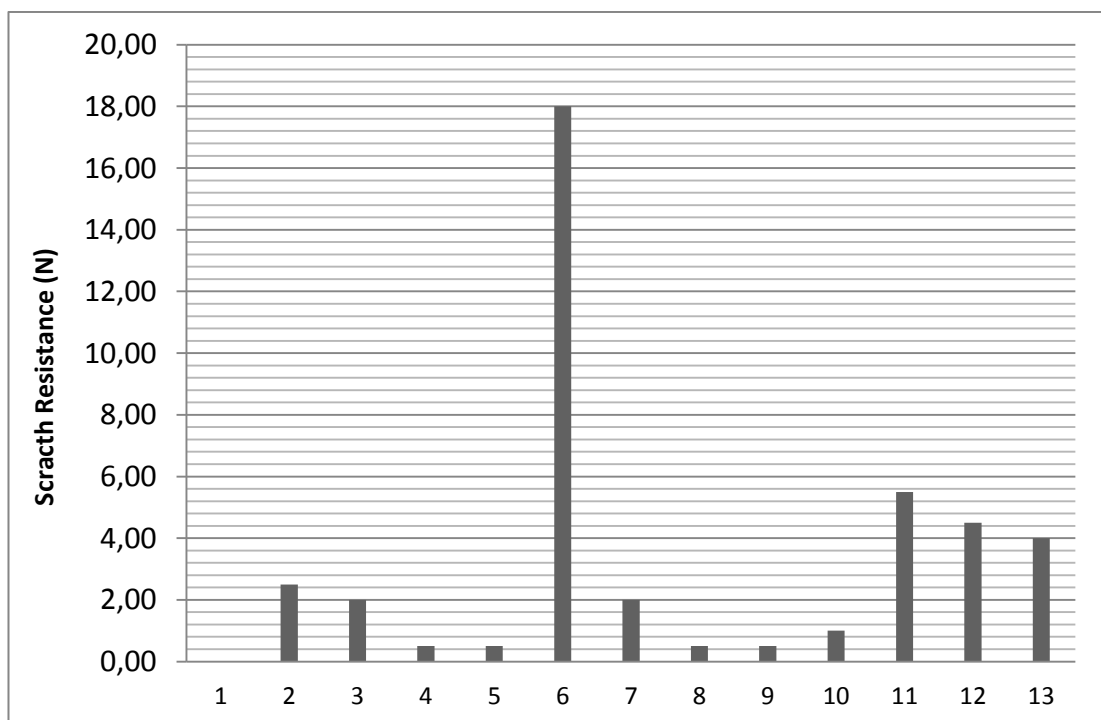
CHEMICAL INGREDIENTS	ULTIMATE FORCE (N)	DEFLECTION (mm)	FAILURE STRENGTH (MPa)	SCRATCH RESISTANCE (N)	NUMBER OF EXPERIMENTS
<b>1)</b> Uncoated Glass (3,2 mm)	1363,9	0,225	74,8		42
<b>2)</b> 100% TiO <sub>2</sub> -SiO <sub>2</sub>	2554,8	0,319	140,2	2-3	40
<b>3)</b> 94,5% TiO <sub>2</sub> -SiO <sub>2</sub> - 5,5% Ta <sub>2</sub> O <sub>5</sub>	2585,5	0,330	141,9	2	22
<b>4)</b> 100% TiO <sub>2</sub> -SiO <sub>2</sub> (II)	1425,3	0,227	78,2	0-1	22
<b>5)</b> 94,5% TiO <sub>2</sub> -SiO <sub>2</sub> (II) - 5,5% Ta <sub>2</sub> O <sub>5</sub>	1429,9	0,223	78,5	0-1	18
<b>6)</b> 100% Ta <sub>2</sub> O <sub>5</sub>	4107,0	0,452	225,3	18	7
<b>7)</b> 50% TiO <sub>2</sub> -SiO <sub>2</sub> - 50% Ta <sub>2</sub> O <sub>5</sub> (powder)	1822,7	0,285	100,0	2	11
<b>8)</b> 100% Ta <sub>2</sub> O <sub>5</sub> (powder)	1496,6	0,236	82,1	0-1	11
<b>9)</b> 50% TiO <sub>2</sub> -SiO <sub>2</sub> - 50% Ta <sub>2</sub> O <sub>5</sub>	1583,9	0,241	86,9	0-1	22
<b>10)</b> 80% TiO <sub>2</sub> -SiO <sub>2</sub> - 20% Ce NP	2525,4	0,331	138,6	1	8
<b>11)</b> 99% TiO <sub>2</sub> -SiO <sub>2</sub> - 1% NMP (0,025gr SWCNT)	2728,3	0,336	149,7	5-6	11
<b>12)</b> 99% TiO <sub>2</sub> -SiO <sub>2</sub> - 1% NMP (0,035gr SWCNT)	2561,5	0,330	140,5	3-4	11
<b>13)</b> 100% TiO <sub>2</sub> -SiO <sub>2</sub> (dip coated)	3121,8	0,390	171,3	4	22



Figure 5.8 and 5.9 show the comparison for both mechanical tests results. Ta<sub>2</sub>O<sub>5</sub> samples give incredible results, especially on surface resistance.



**Figure 5.8:** Comparison for ultimate strength.



**Figure 5.9:** Comparison for scratch resistance.

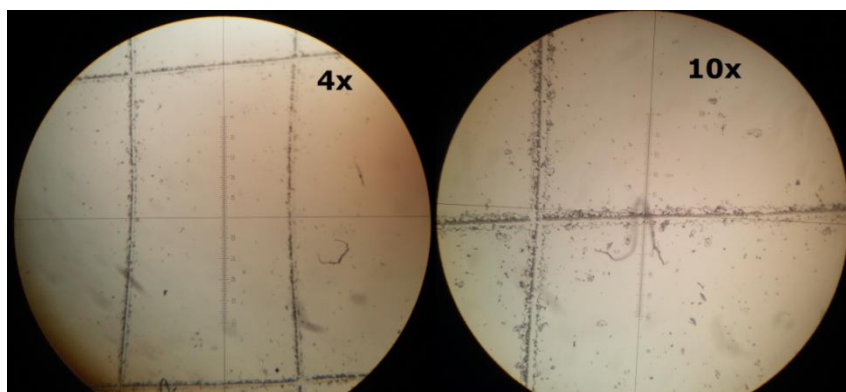
FEM results are summarized on Table 5.4 FEM gave nearly perfect results for all samples. It is obvious that, Ansys could easily apply to analyze bilayer or multilayer materials. Table 5.6 shows difference between Ansys and experimental results.

**Table 5.6:** Comparing experimental and FEM results.

Samples	Experimental Results	FEM Results	Difference
<b>Uncoated Glass</b>			
Deflection (mm)	0,225	0,215	-4,5%
Maximum Stress (MPa)	74,8	74,4	-0,5%
<b>TiO<sub>2</sub>-SiO<sub>2</sub></b>			
Deflection (mm)	0,319	0,307	-3,7%
Maximum Stress (MPa)	140,2	145,4	3,7%
<b>TA<sub>2</sub>O<sub>5</sub></b>			
Deflection (mm)	0,452	0,437	-3,3%
Maximum Stress (MPa)	225,3	205,6	-8,7%

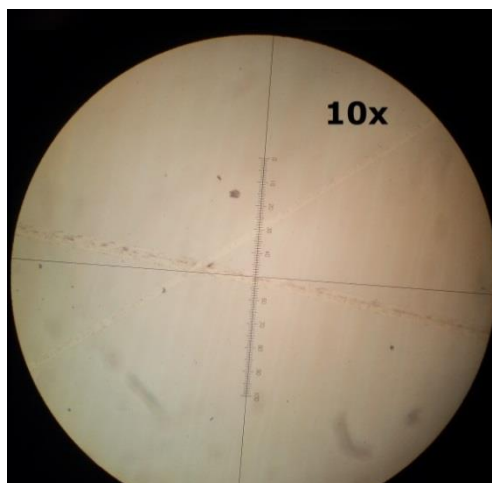
#### 5.4. Optical Microscopy Results

Optical microscopy was used to examine surface properties of the samples. The method was applied to regions after scratch test in order to investigate adhesion properties of the films. Wide and deep trails mean the coating film is ductile and easy to remove. Distinctive trails of TiO<sub>2</sub> – SiO<sub>2</sub> film can be easily seen in Figure 5.10. Actually, the adhesion properties of the sol was quite well during coating process, but Figure 5.10 shows that the film can be easily removed from glass substrate.



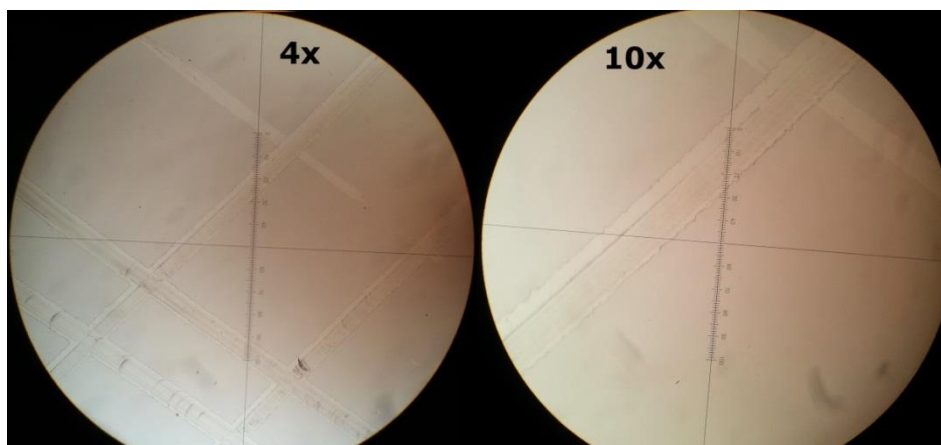
**Figure 5.10:** Optical microscopy image of TiO<sub>2</sub> - SiO<sub>2</sub> film with different magnification.

Figure 5.11 shows excellent adhesion of tantalum pentoxide thin films as well as hardness. Hardness values are given in previous section (5.3) and optical microscopy image supports results. Samples gave quite obscure trails, which hard to distinguish.



**Figure 5.11:** Optical microscopy image of  $\text{Ta}_2\text{O}_5$  thin film.

Figure 5.12 shows unfavorable effects of  $\text{CeO}_2$  nanoparticles in  $\text{TiO}_2 - \text{SiO}_2$  binary system for both adhesion and hardness.



**Figure 5.12:** Optical microscopy image of  $\text{TiO}_2 - \text{SiO}_2$  with  $\text{CeO}_2$  nanoparticles film with different magnification.

## 5.5. Scanning Electron Microscopy Results

SEM images examine the surface properties of the thin films. The images were taken with 2 kV and different magnification factors. Figure 5.13-5.15 show the SEM image of  $\text{Ta}_2\text{O}_5$  film with different magnifications. The thicknesses of tantalum pentoxide thin films are around 90 nm. SEM images represent that films are deposited on glass substrates uniformly.

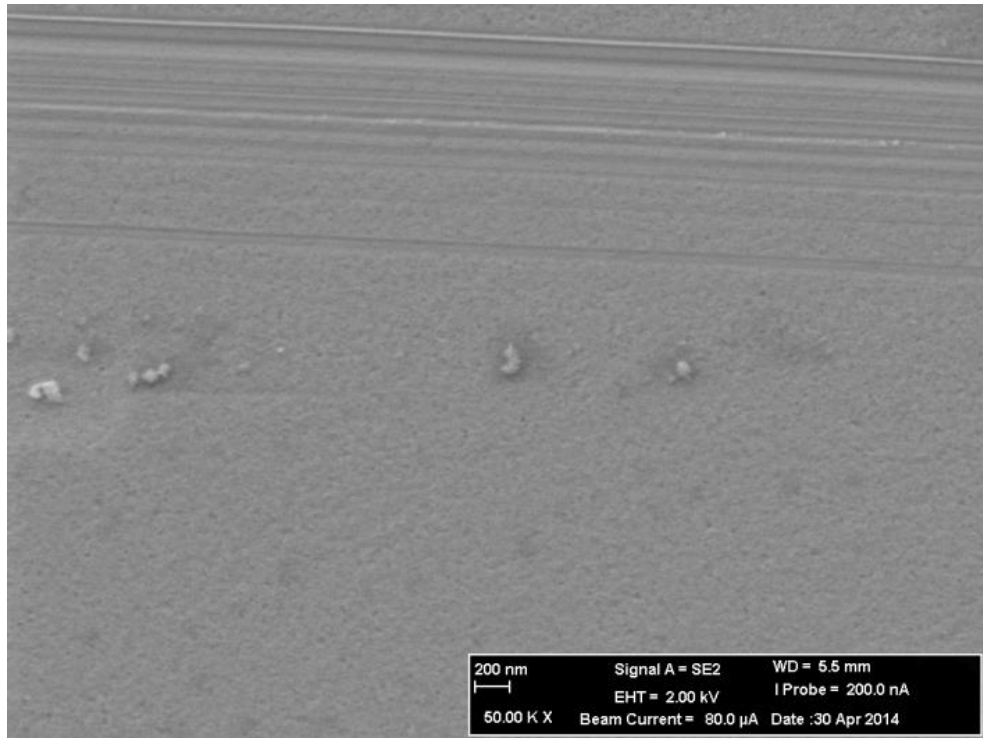


**Figure 5.13:** SEM image of Ta<sub>2</sub>O<sub>5</sub> thin film (50X).

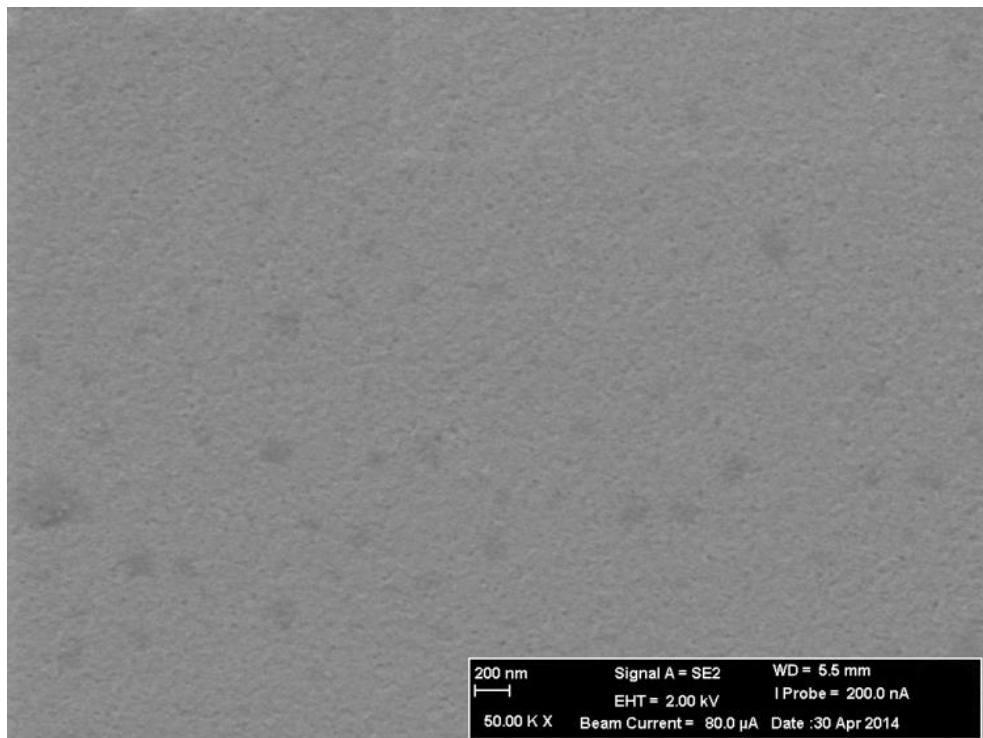


**Figure 5.14:** SEM image of Ta<sub>2</sub>O<sub>5</sub> thin film (50X).

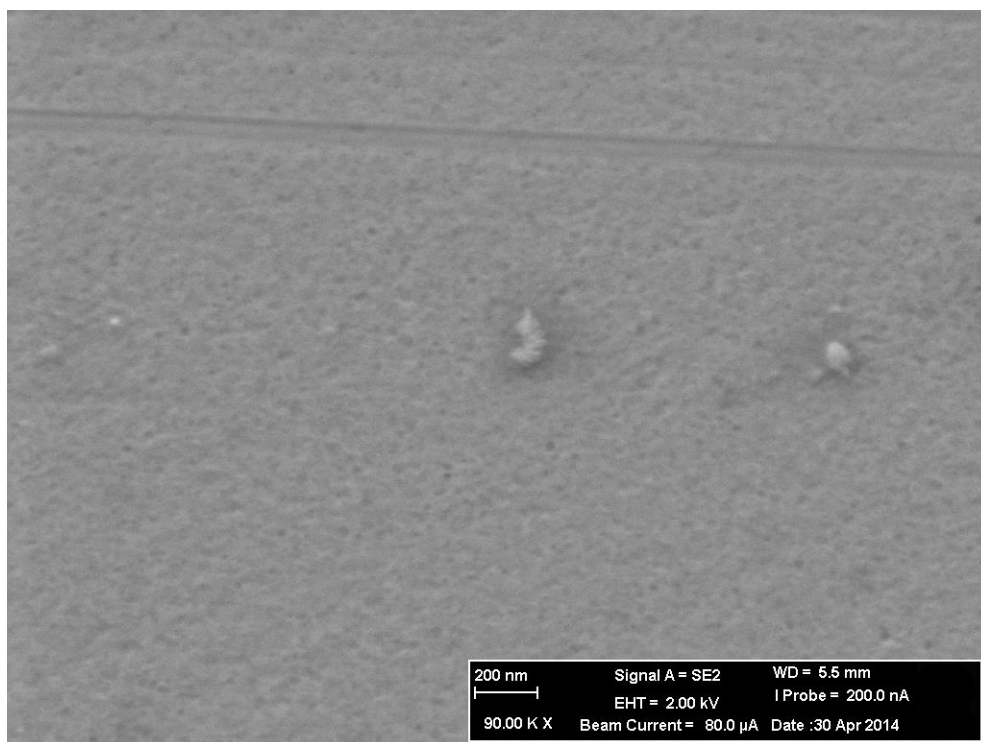


**Figure 5.15:** SEM image of Ta<sub>2</sub>O<sub>5</sub> thin film (90X).

Figure 5.16 and 5.17 show the SEM images of TiO<sub>2</sub> - SiO<sub>2</sub> composite film.

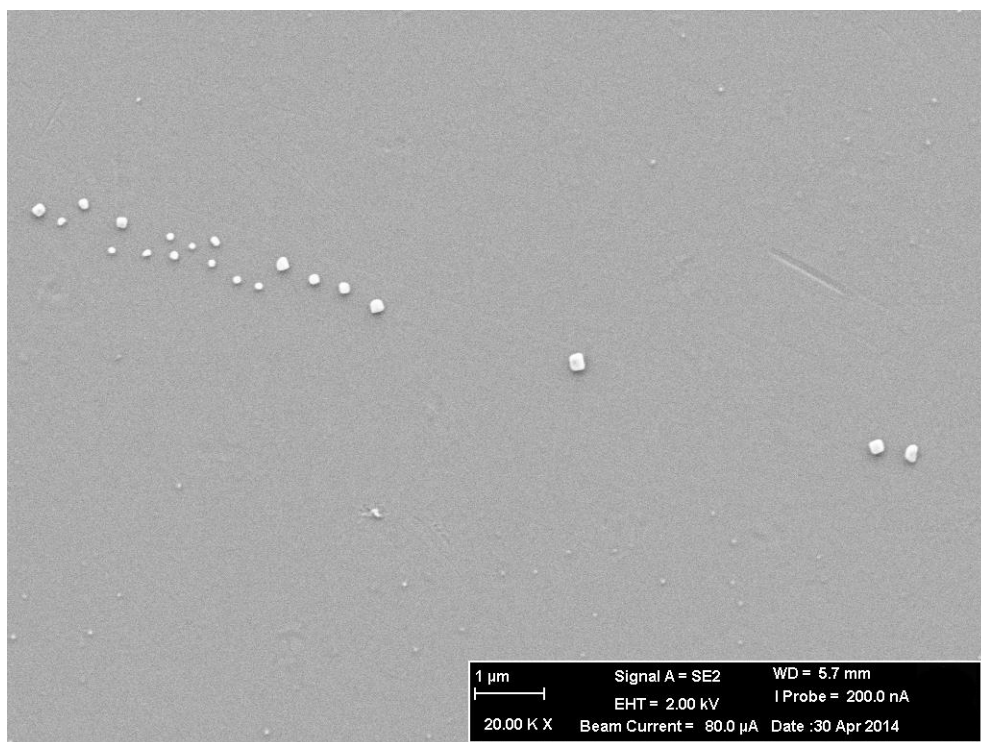


**Figure 5.16:** SEM image of TiO<sub>2</sub> - SiO<sub>2</sub> film (20X).

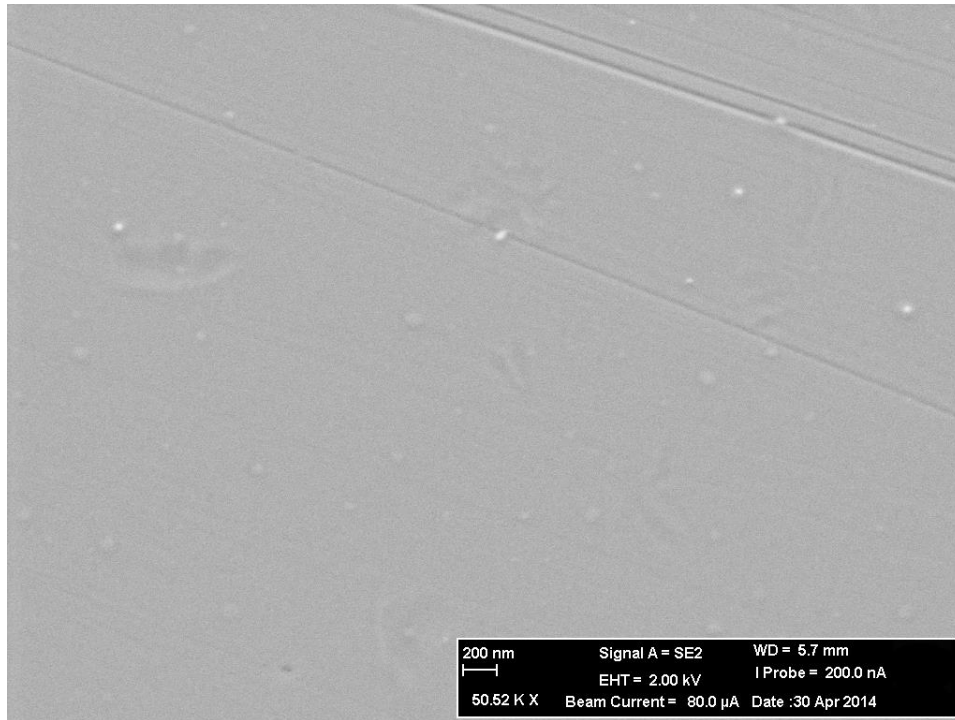


**Figure 5.17:** SEM image of  $\text{TiO}_2$  -  $\text{SiO}_2$  film (50X).

SEM images of  $\text{TiO}_2$  –  $\text{SiO}_2$  composite films show that all the films were coated uniformly. The thicknesses of the composite films are around 2200 nm. There are some contamination on the glass substrates as shown in Figure 5.16 easily. Figure 5.18 and 5.19 show the SEM image of  $\text{TiO}_2$  -  $\text{SiO}_2$  + SWCNT film.

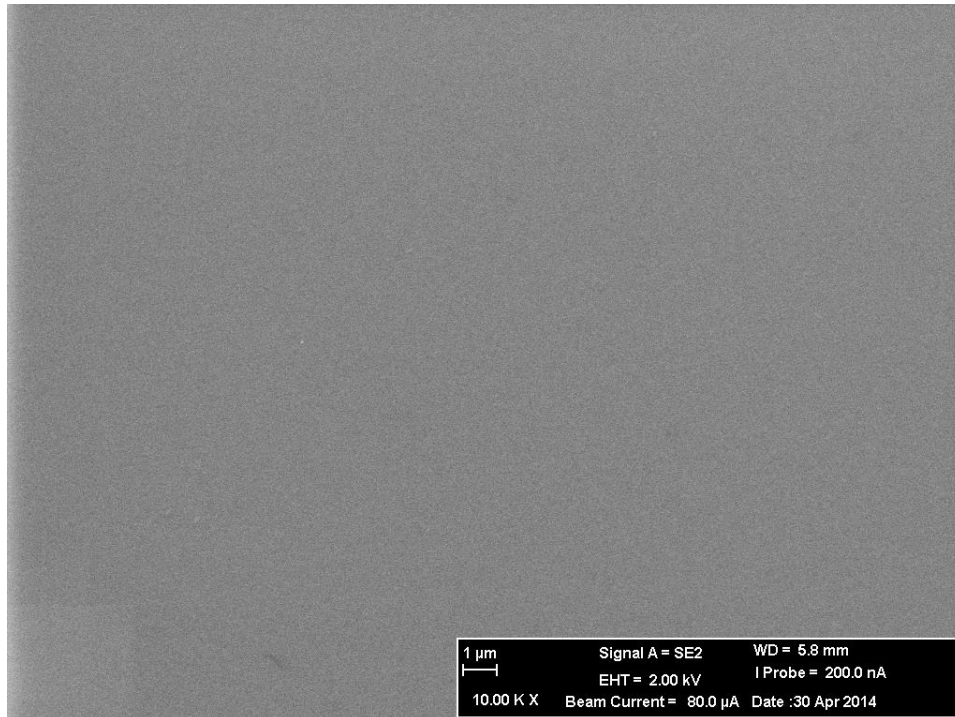


**Figure 5.18:** SEM image of SWCNT (less) reinforced  $\text{TiO}_2$  -  $\text{SiO}_2$ .



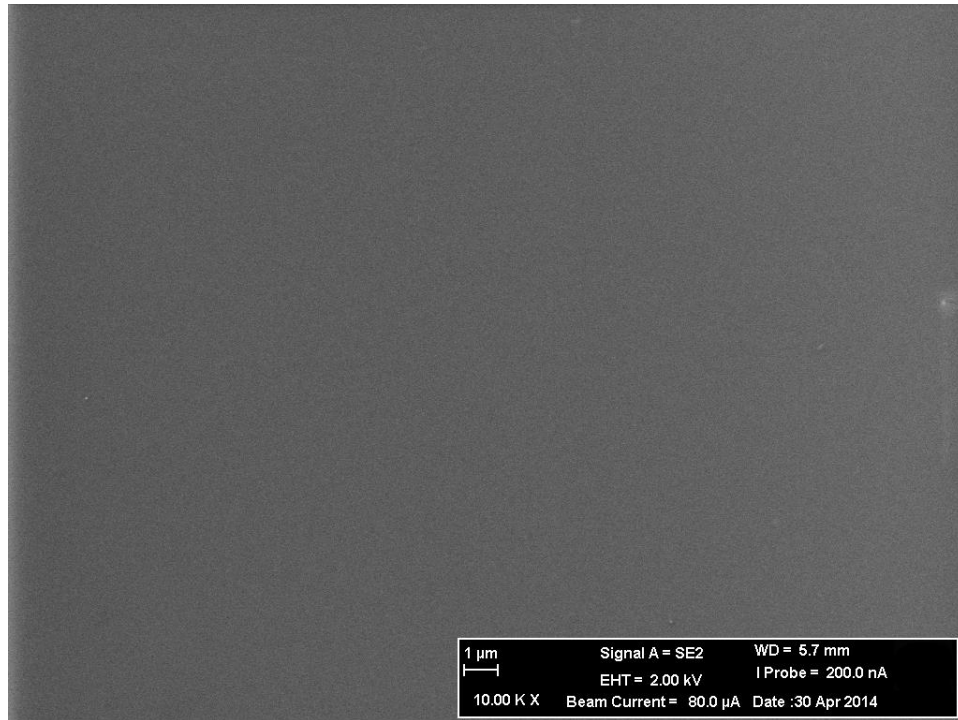


**Figure 5.19: SEM image of SWCNT (more) reinforced  $\text{TiO}_2$  -  $\text{SiO}_2$ .**

Figure 5.18 and 5.19 show that, the transparency decreases with increasing carbon nanotube percentage. Besides, ultimate strength and hardness are going worse with higher amount of CNTs.

## 5.6. Atomic Force Microscopy Results

Surface roughness of samples was obtained with AFM. Roughness affects fatigue limit, so materials having more uniform surfaces can last longer. Figure 5.20 shows AFM image of  $\text{Ta}_2\text{O}_5$  sample.

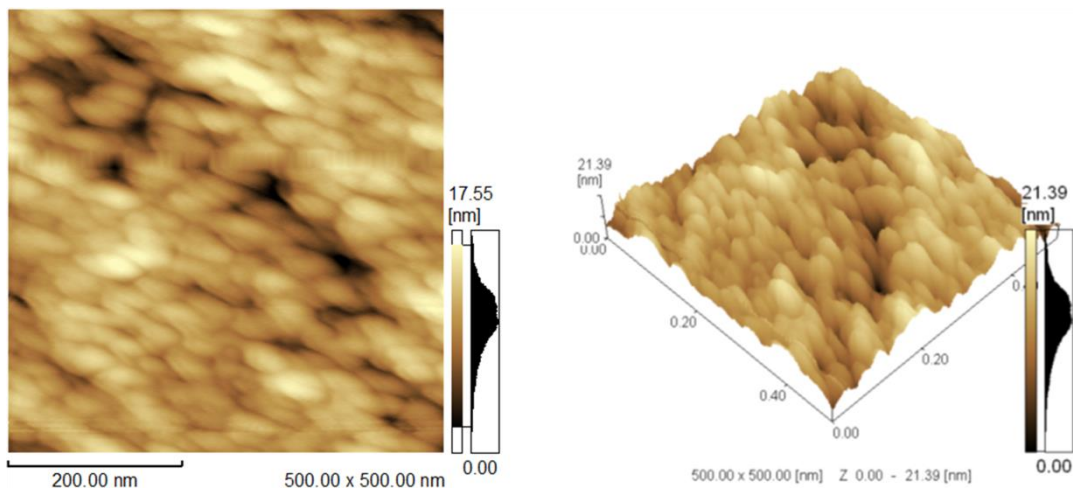


**Figure 5.20: AFM image of  $\text{Ta}_2\text{O}_5$  thin film.**

AFM results of Ta<sub>2</sub>O<sub>5</sub> thin film are seemed quite uniform. Table 5.7 shows AFM results of Ta<sub>2</sub>O<sub>5</sub> sample.

**Table 5.7:** AFM results of Ta<sub>2</sub>O<sub>5</sub> thin film.

All Area	Ry:20.704 [nm]
X:500.000 [nm]	Rz:10.169 [nm]
Y:500.000 [nm]	Rms:3.092 [nm]
Area:250000.000 [(nm) <sup>2</sup> ]	Rp:8.478 [nm]
Ra:2.451 [nm]	Rv:12.226 [nm]

Figure 5.21 and table 5.8 show the AFM image and results of TiO<sub>2</sub> – SiO<sub>2</sub> sample, respectively.

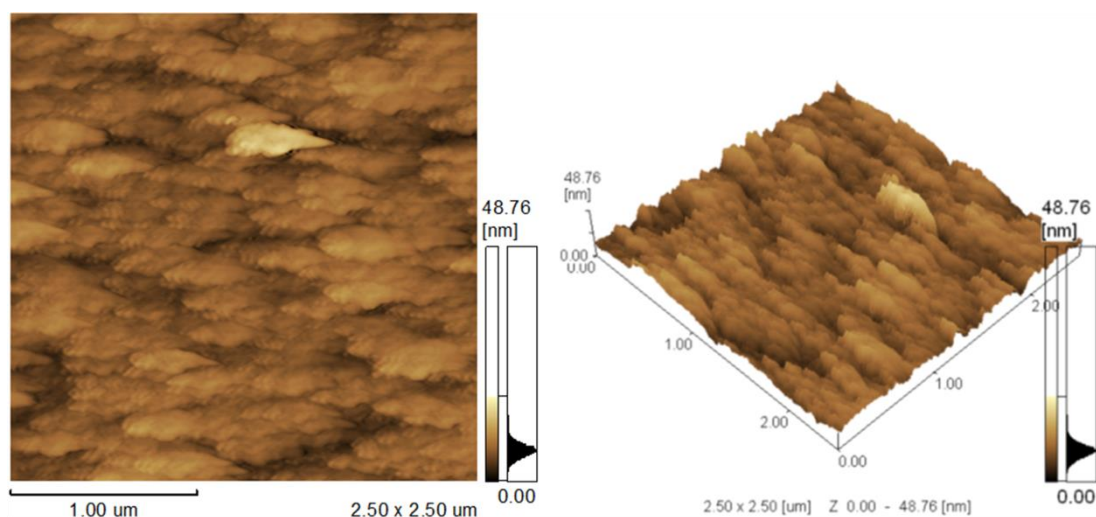


**Figure 5.21:** AFM images of TiO<sub>2</sub> - SiO<sub>2</sub> film.

TiO<sub>2</sub> – SiO<sub>2</sub> films are much thicker than tantalum oxide ones. However, average roughness is quite well. This leads enhancement on both optical and mechanical properties.

**Table 5.8:** AFM results of TiO<sub>2</sub> - SiO<sub>2</sub> film.

All Area	Ry:41.933 [nm]
X:2.500 [μm]	Rz:19.546 [nm]
Y:2.500 [μm]	Rms:4.315 [nm]
Area:6.250 [(μm) <sup>2</sup> ]	Rp:24.013 [nm]
Ra:3.318 [nm]	Rv:17.920 [nm]



## 5.7. Profilometer Results

Film thicknesses were obtained by Veeco Dektak 150 Profilometer mechanically. The results for the thickness of the films were incomparable. The average thickness was  $90\text{ nm}$  and very uniform for tantalum pentoxide. However, the average thickness was  $2200\text{ nm}$  and slightly uniform for  $\text{TiO}_2 - \text{SiO}_2$  samples. That means, we need less material to coat  $\text{Ta}_2\text{O}_5$  on glass substrate. Figure 5.22 shows profilometer results of  $\text{Ta}_2\text{O}_5$  sample.

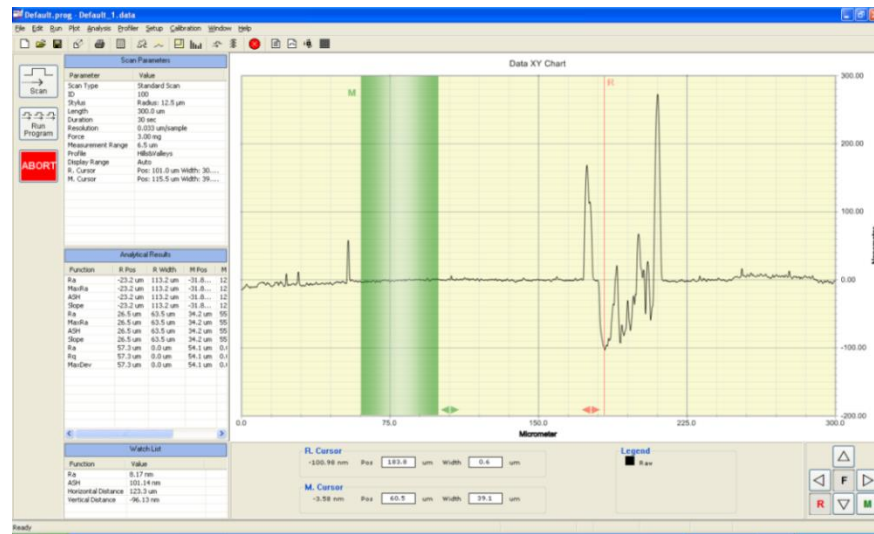


**Figure 5.22:** Profilometer result image of  $\text{Ta}_2\text{O}_5$  thin film.

Figure 5.22 and 5.23 show removing  $\text{Ta}_2\text{O}_5$  on glass substrate is harder than  $\text{TiO}_2 - \text{SiO}_2$  binary system. The step was created on the film surface in order to get uncoated and coated parts. Figure 5.23 shows profilometer results of  $\text{TiO}_2 - \text{SiO}_2$  sample.

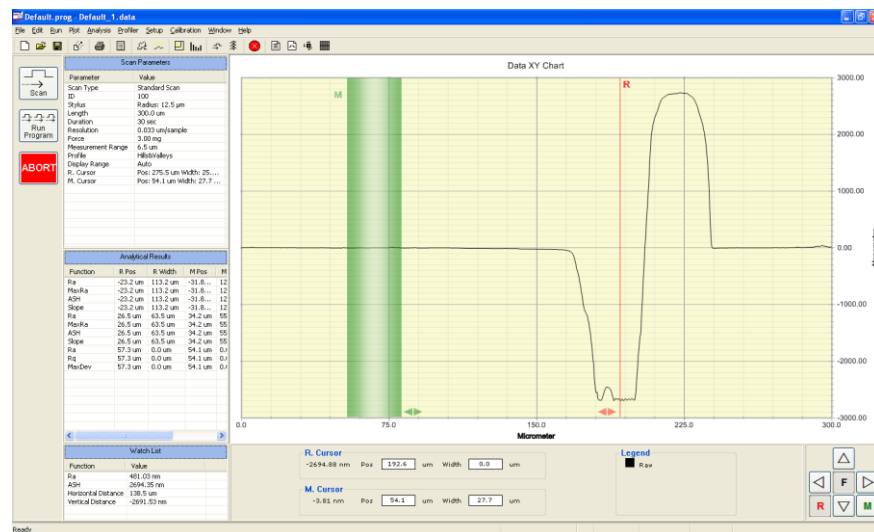


**Figure 5.23:** Profilometer result image of  $\text{TiO}_2 - \text{SiO}_2$  film.

## 5.8. Tensiometer Results

Contact angle determines the surface whether hydrophobic or hydrophilic. Table 5.9 shows the contact angle values for different coatings.

**Table 5.9:** Contact angle for different coatings.

Material	Contact Angle ( $\theta$ )
$\text{TiO}_2 - \text{SiO}_2$	$58 \pm 1$
94,5% $\text{TiO}_2 - \text{SiO}_2 - 5,5\% \text{Ta}_2\text{O}_5$	$47 \pm 1$
$\text{Ta}_2\text{O}_5$	$84 \pm 1$
50% $\text{TiO}_2 - \text{SiO}_2 - 50\% \text{Ta}_2\text{O}_5$	$52 \pm 1$
80% $\text{TiO}_2 - \text{SiO}_2 - 20\% \text{CeO}_2 \text{ NP}$	$71 \pm 1$
99% $\text{TiO}_2 - \text{SiO}_2 - 1\% \text{SWCNT}$	$51 \pm 1$

According to results,  $\text{Ta}_2\text{O}_5$  coating is the most hydrophobic surface and adding  $\text{CeO}_2$  nanoparticles reduces the contact angle. Beside, adding small amount of carbon nanotubes completely changes the behavior. Ternary system of  $\text{TiO}_2$ ,  $\text{SiO}_2$  and  $\text{Ta}_2\text{O}_5$  behaves like hydrophilic. Figure 5.24 shows the behavior of pure water droplet on different surfaces.

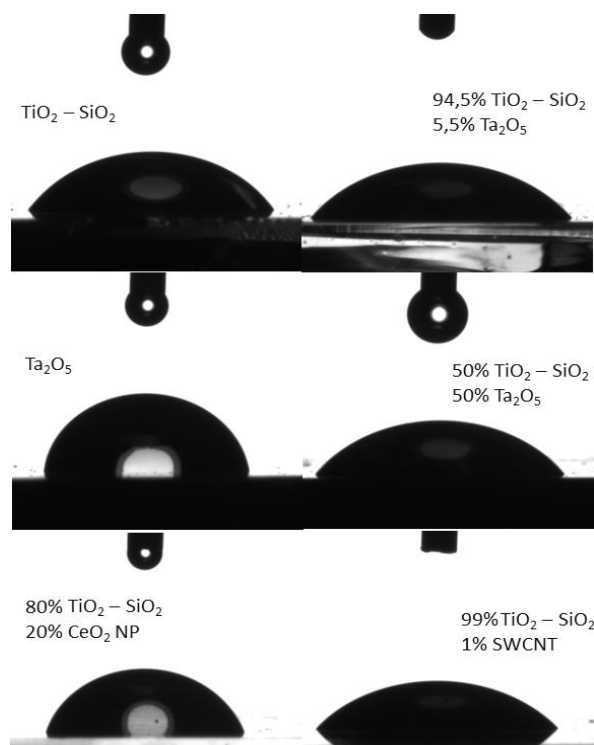


**Figure 5.24:** Tensiometer pictures of different coatings.

## 5.9. Ultraviolet-Visible Spectroscopy Results

UV-vis was used to investigate transmittance of the films. Since we have been working with glasses, optical transparency is crucial parameter. Figure 5.25 and 5.26 shows the transmittance values for different coatings against wavelength and energy, respectively.  $\text{TiO}_2 - \text{SiO}_2$  samples have the highest transmittance values despite the thicker film thicknesses. Adding  $\text{CeO}_2$  nanoparticles reduces transmittance dramatically.

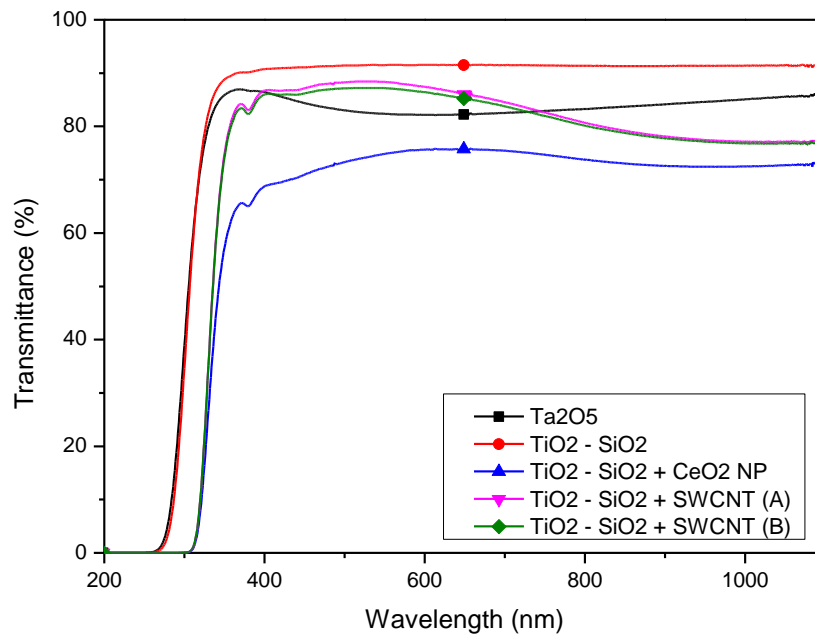


**Figure 5.25:** Transmittance for different coatings with respect to wavelength.

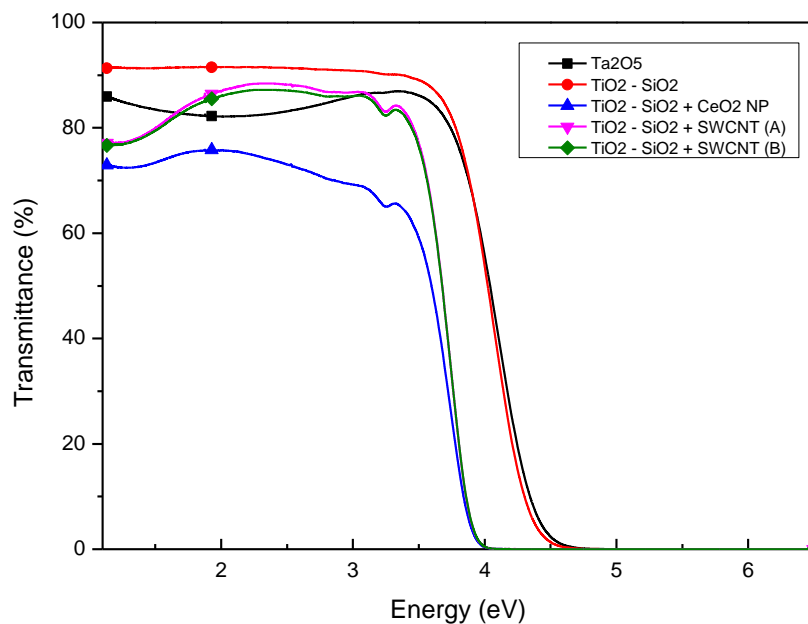


**Figure 5.26:** Transmittance for different coatings with respect to energy.

First derivation of transmittance values against energy are given in Figure 5.27 in order to define band gaps of the films.

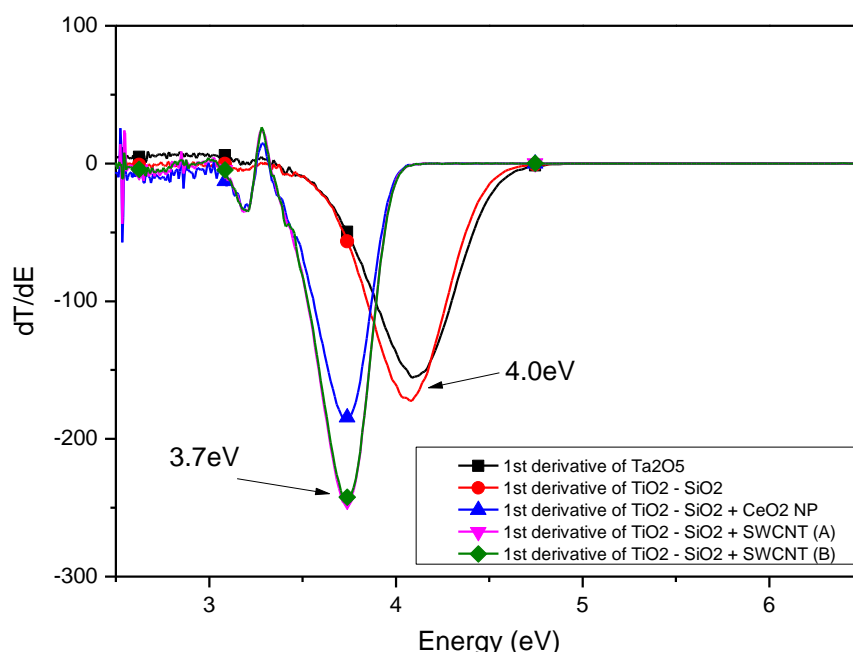


**Figure 5.27:** First derivation of transmittance with respect to photon energy.

A NKD 7000 model spectrophotometer (Aquila, UK) has been used to measure the optical transmittance and reflectance of the films over the spectral range from 280 to 1000 nm at 30° angle of incidence. The optical constants such as refractive indices and the extinction coefficients of the films were calculated using the Pro-Optix software. The s and p polarization of transmittance and reflectance values of the deposited films were measured by spectrophotometer analyses over the spectral range of 350-1000 nm. Results are shown in Figures 5.28-5.31. As can be seen from Figure 5.28-5.29, p and s polarization values of transmittance of the films are quite high values for all the films. Their transmittance values alter from 85 to 95 %. Although tantalum pentoxide films are transparent and reflect light well in all over the spectrum. Ta<sub>2</sub>O<sub>5</sub> has ~12.5% reflectance in the visible range. The transmittance values of Ta<sub>2</sub>O<sub>5</sub> thin film reaches about ~75% and 95 % in the all-region. Although Ta<sub>2</sub>O<sub>5</sub> film has a slightly low transmittance value in the visible range, the refractive indices of the films are higher. The average transmittance values of all films ranged from ~89% to ~95% in the visible range. It can be concluded that the film compositions and additives have no significant difference for the transmittance

values. Optical properties especially the transparency of the films obtained are in good agreement with the literature.

It is thus possible, in chosen conditions, to synthesize the films of optimal optical properties as reflective/antireflective and protective coatings for different applications. These films demonstrated excellent transparency, characteristic for wide band gap materials.

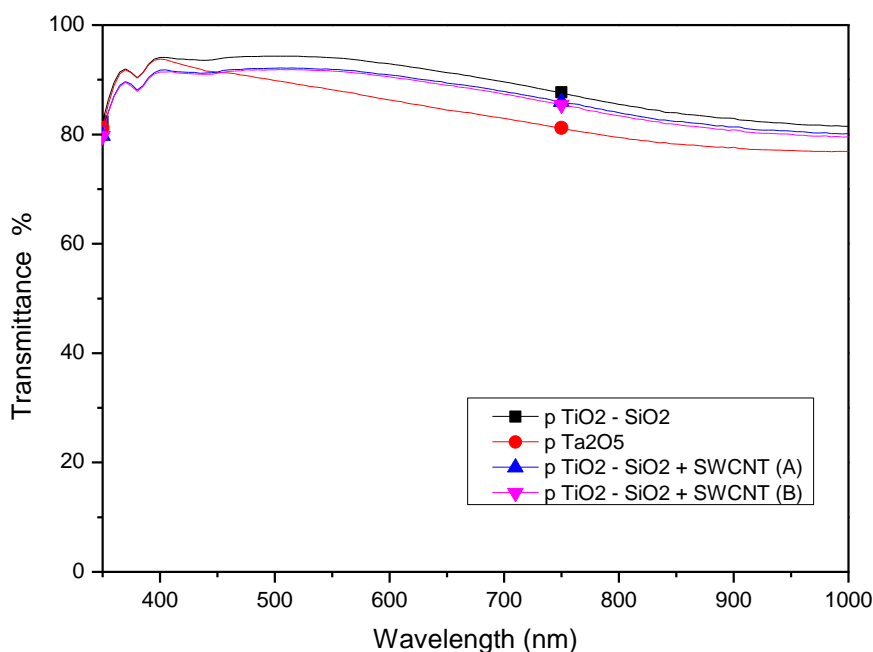


**Figure 5.28:** Transmittance of deposited films with respect to wavelength (p polarization).

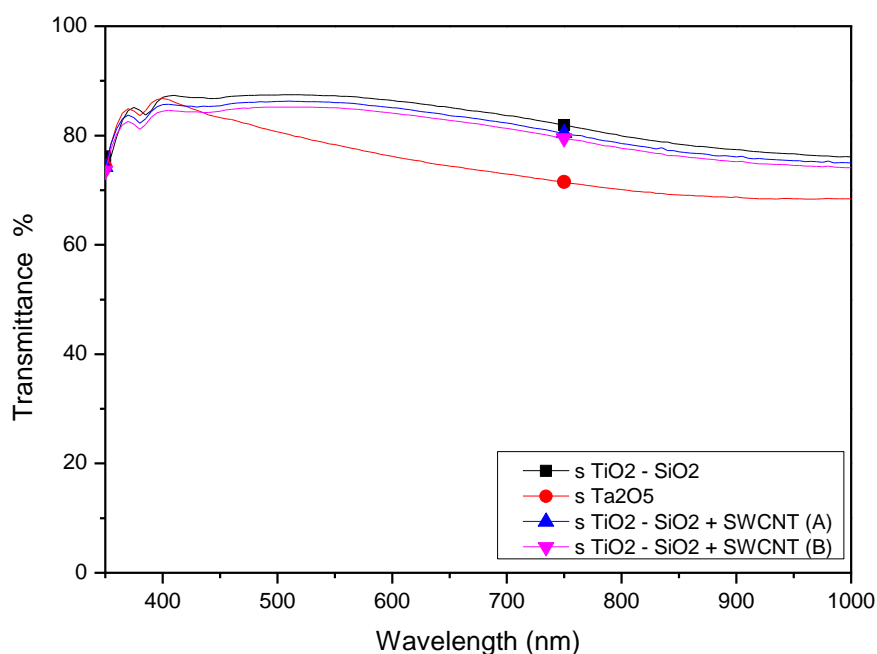


**Figure 5.29:** Transmittance of deposited films with respect to wavelength (s polarization).

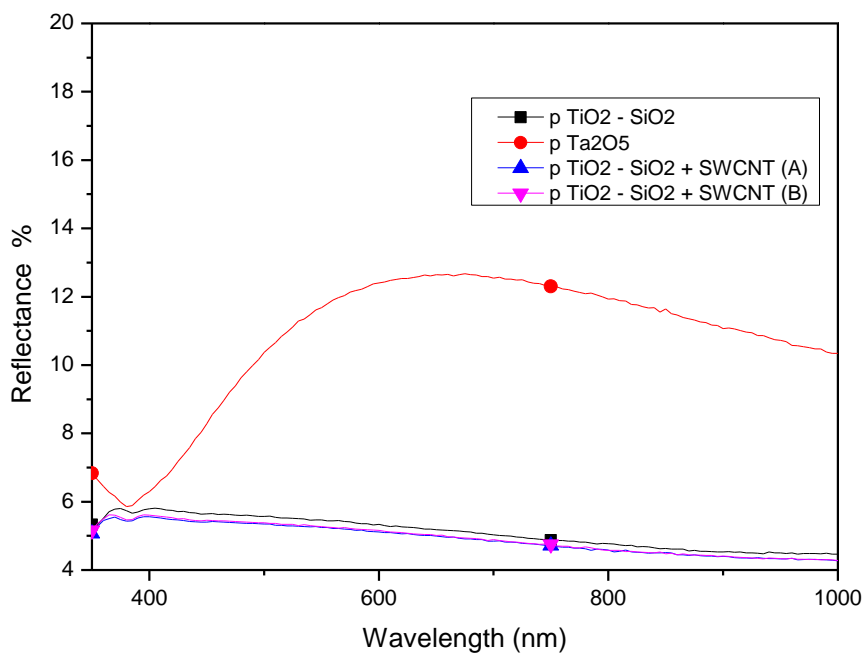


**Figure 5.30:** Reflectance of deposited films with respect to wavelength (p polarization).

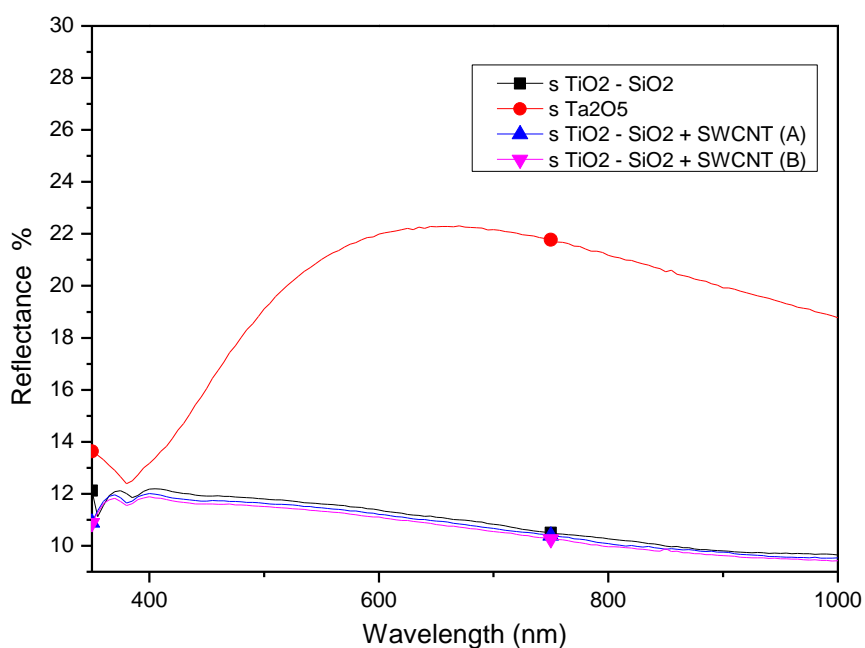


**Figure 5.31:** Reflectance of deposited films with respect to wavelength (s polarization).

## 5.10. X-ray Photoelectron Spectroscopy Results

Compositional elemental characterization of the deposited films carried out by X-Ray Photoelectron Spectroscopy (XPS) measurements. It was aimed to determine the constituents of the coatings, as well as binding structures. Figures 5.32-5.40 show the spectra of the coated films obtained from XPS where a general surface survey was performed.

There are visible peaks that belong to Si, Ti, Ta and C elements. Several windows (C1s, Si2p, O1s, Ta4f, Ti2p) were rescanned to get detailed information about elemental peaks. Carbon peaks may come from contaminations. Nevertheless, the peaks require further fitting analysis for exact determination of phase compositions and stoichiometry.

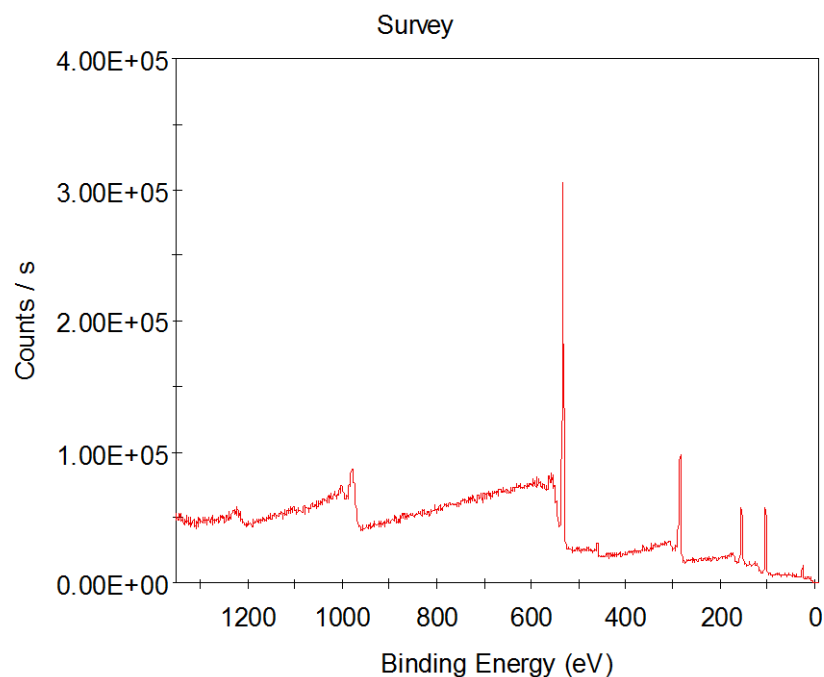


**Figure 5.32:** XPS survey scan spectra of calcined  $\text{TiO}_2$  -  $\text{SiO}_2$  film at 450 °C.

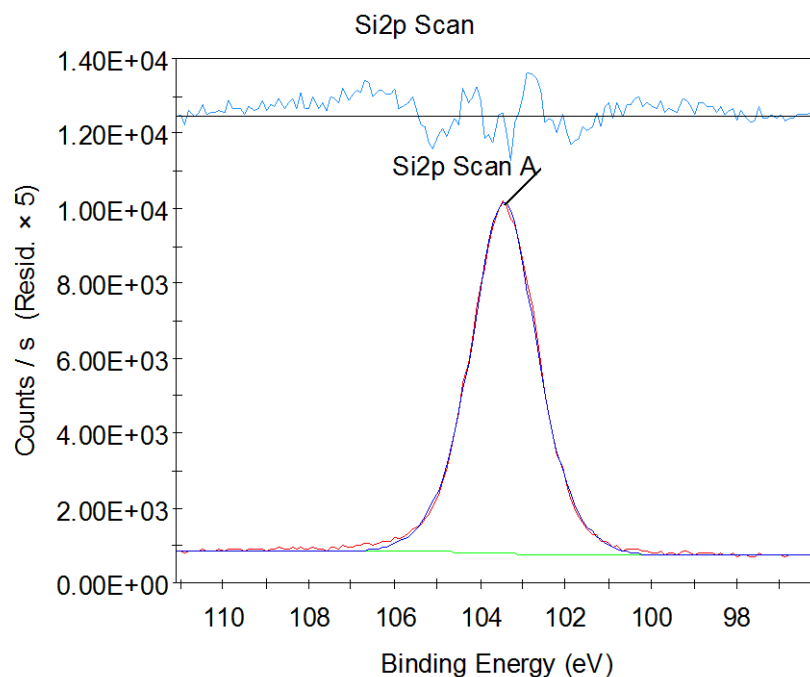


**Figure 5.33:** XPS Si2p scan spectra of calcined  $\text{TiO}_2$  -  $\text{SiO}_2$  film at 450 °C.

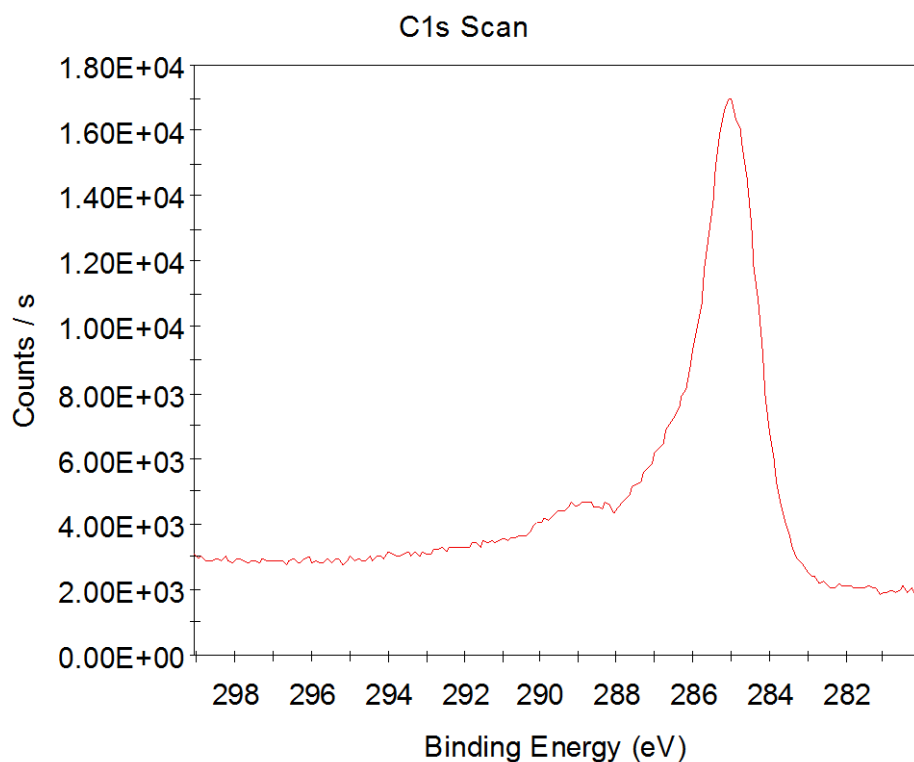


**Figure 5.34:** XPS C1s scan spectra of calcined  $\text{TiO}_2$  -  $\text{SiO}_2$  film at 450 °C.

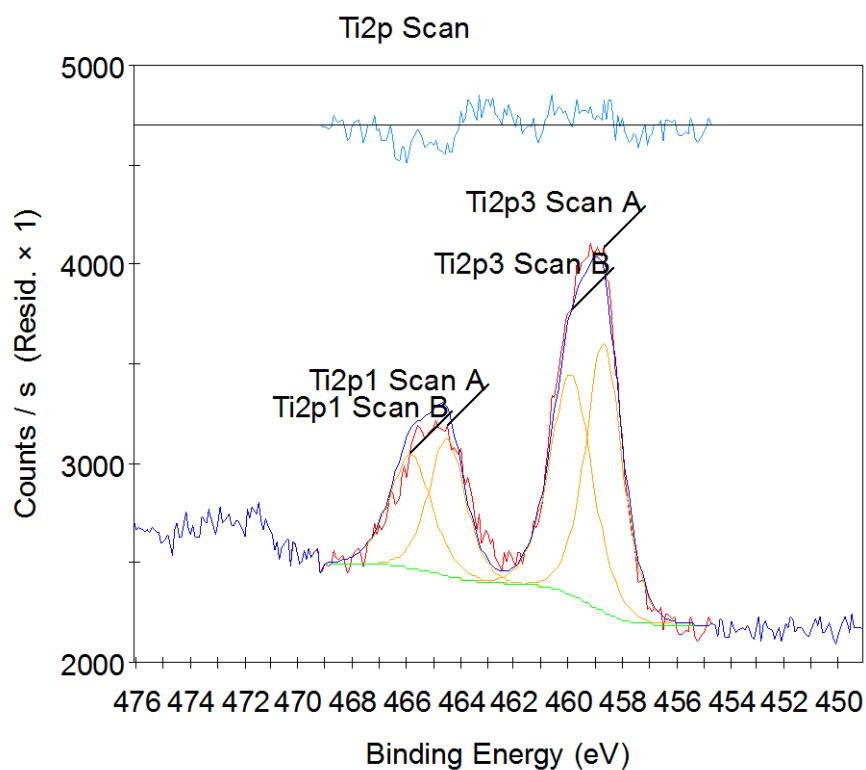


**Figure 5.35:** XPS Ti2p scan spectra of calcined  $\text{TiO}_2$  -  $\text{SiO}_2$  film at 450 °C.



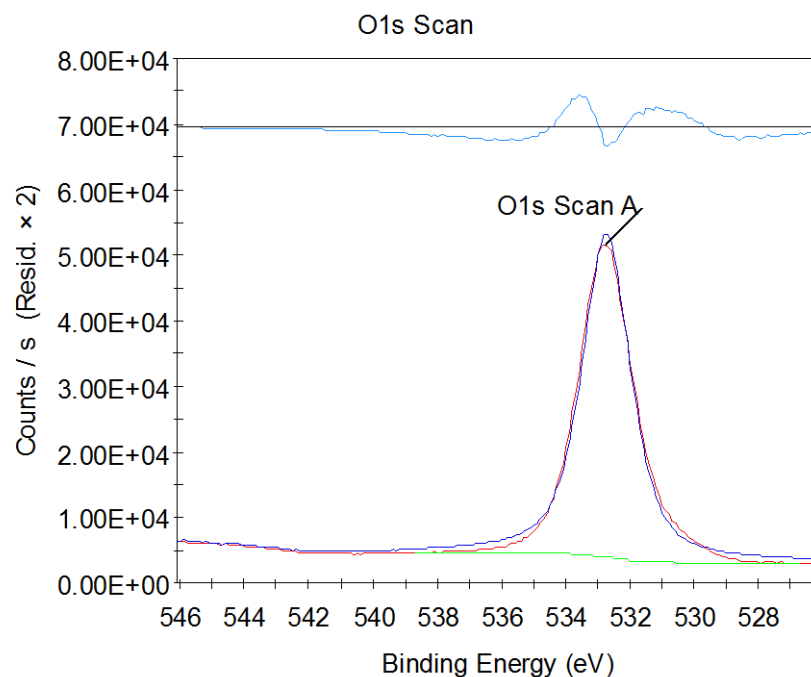


**Figure 5.36:** XPS O1s scan spectra of calcined  $\text{TiO}_2$  -  $\text{SiO}_2$  film at 450 °C.

**Table 5.10:** Detailed XPS spectra of calcined  $\text{TiO}_2$  -  $\text{SiO}_2$  film at 450 °C.

<i>Name</i>	<i>Peak BE</i>	<i>FWHM eV</i>	<i>Area (P) CPS.eV</i>	<i>Atomic %</i>	<i>Q</i>
Si2p Scan A	103.43	1.79	18964.17	31.66	1
Ti2p3 Scan A	458.68	1.59	2429.09	0.76	1
Ti2p3 Scan B	459.89	1.84	2299.72	0.72	1
O1s Scan A	532.72	1.80	114916.78	66.86	1

Figure 5.37-5.40 and table 5.11 show the XPS scans for  $\text{Ta}_2\text{O}_5$  samples.

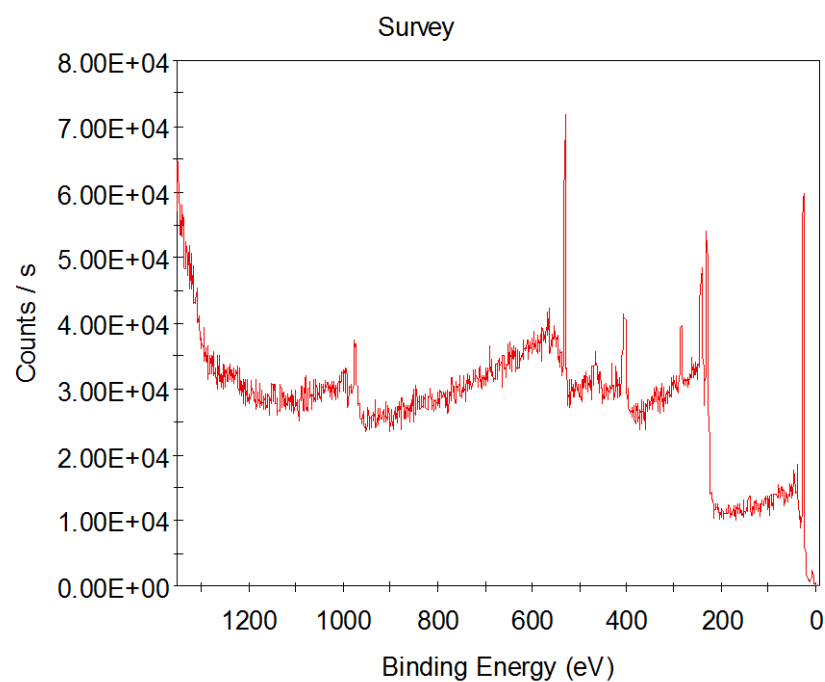


**Figure 5.37:** XPS survey scan spectra of calcined  $\text{Ta}_2\text{O}_5$  film at 450 °C.

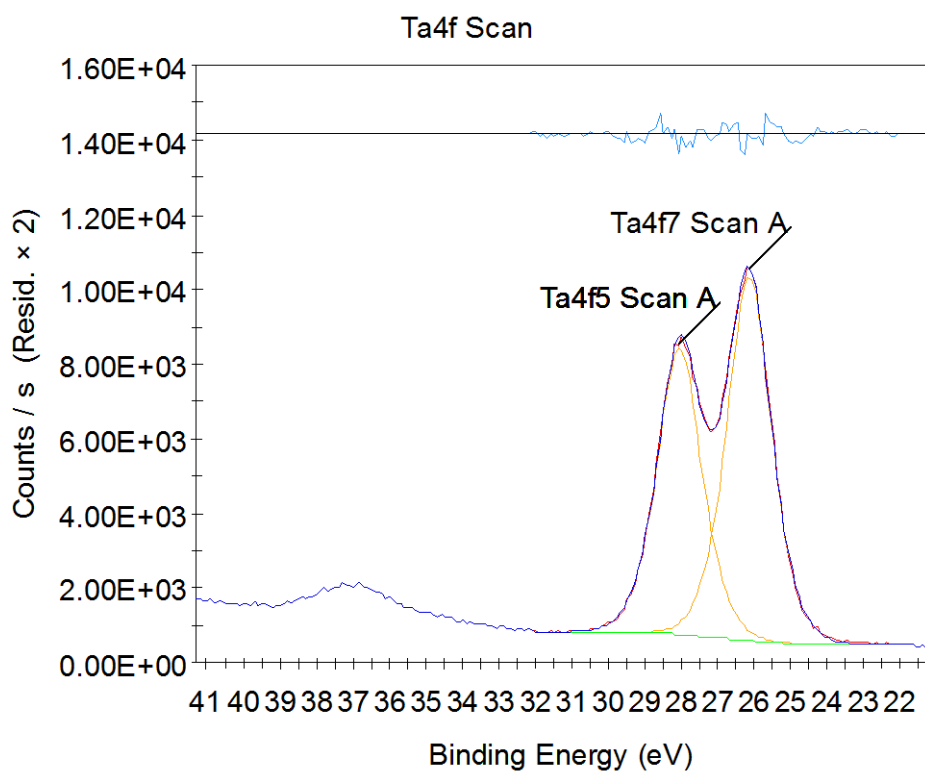


**Figure 5.38:** XPS Ta4f scan spectra of calcined Ta<sub>2</sub>O<sub>5</sub> film at 450 °C.

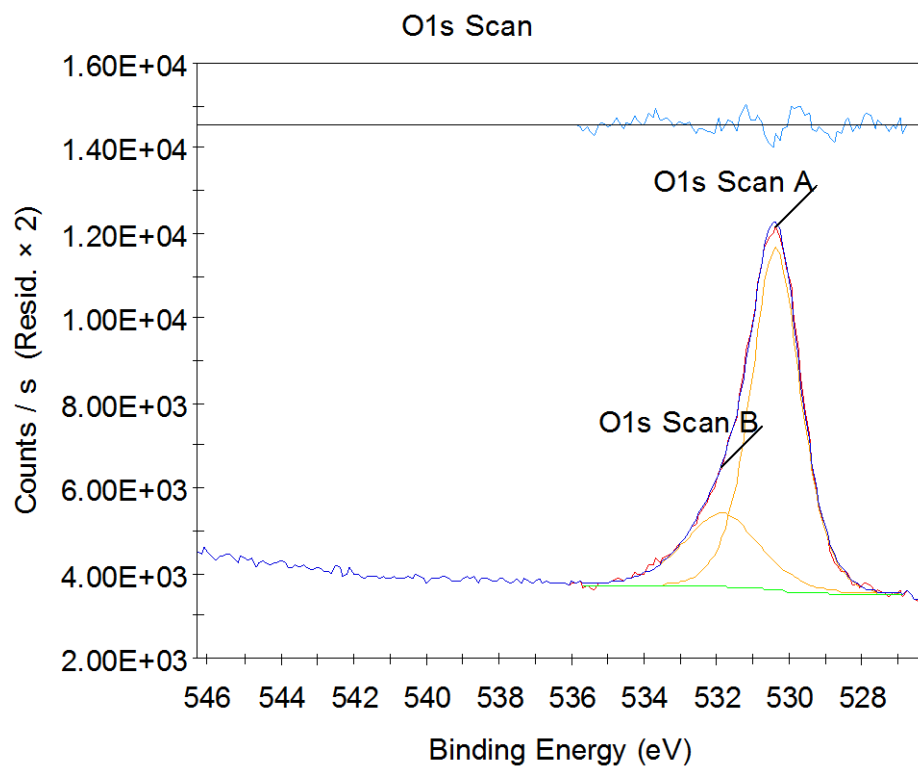


**Figure 5.39:** XPS O1s scan spectra of calcined Ta<sub>2</sub>O<sub>5</sub> film at 450 °C.

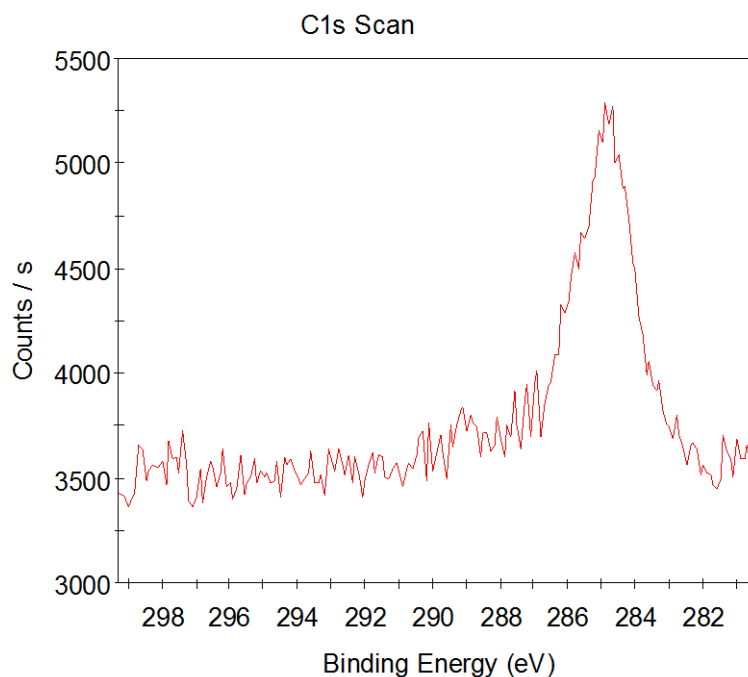


**Figure 5.40:** XPS C1s scan spectra of calcined Ta<sub>2</sub>O<sub>5</sub> film at 450 °C.

**Table 5.11:** Detailed XPS spectra of calcined Ta<sub>2</sub>O<sub>5</sub> film at 450 °C.

<b>Name</b>	<b>Peak BE</b>	<b>FWHM eV</b>	<b>Area (P) CPS.eV</b>	<b>Atomic %</b>	<b>Q</b>
Ta4f7 Scan A	26,19	1.24	15724.66	27.75	1
O1s Scan A	530,40	1.43	14487.96	53.94	1
O1s Scan B	531,87	2.40	4689.88	18.31	1

### 5.11. X-ray Diffractometer Results

Additionally chemical and structural analysis of the samples were done with Cu source (CuKalpha: 1.5418 Angstrom) by X-ray diffractometer (XRD) device. To obtain this structural and physical information from nanostructures and thin films, XRD instruments and techniques are designed to maximize the diffracted X-ray intensities, since the diffracting power of thin films is small. Also as mentioned before, the crystal structure Ta<sub>2</sub>O<sub>5</sub> is little bit complicated. Disordered bulk material can be either amorphous or polycrystalline, however it is difficult to grow single crystals. Generally, it is hard to get crystal information via X-rays but powder diffraction.

XRD results show powder forms of calcined Ta<sub>2</sub>O<sub>5</sub> and TiO<sub>2</sub> – SiO<sub>2</sub> binary systems are amorphous and do not represent any characteristic peaks as shown in Figure 5.41 and 5.42.

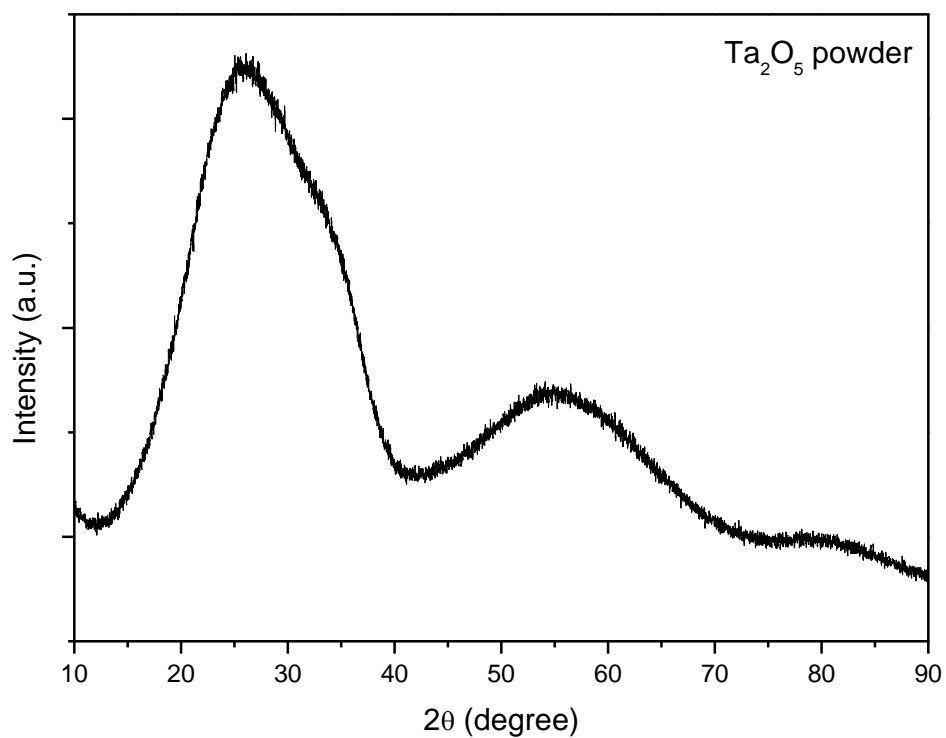


**Figure 5.41:** XRD pattern of  $\text{Ta}_2\text{O}_5$  thin film on glass substrate.

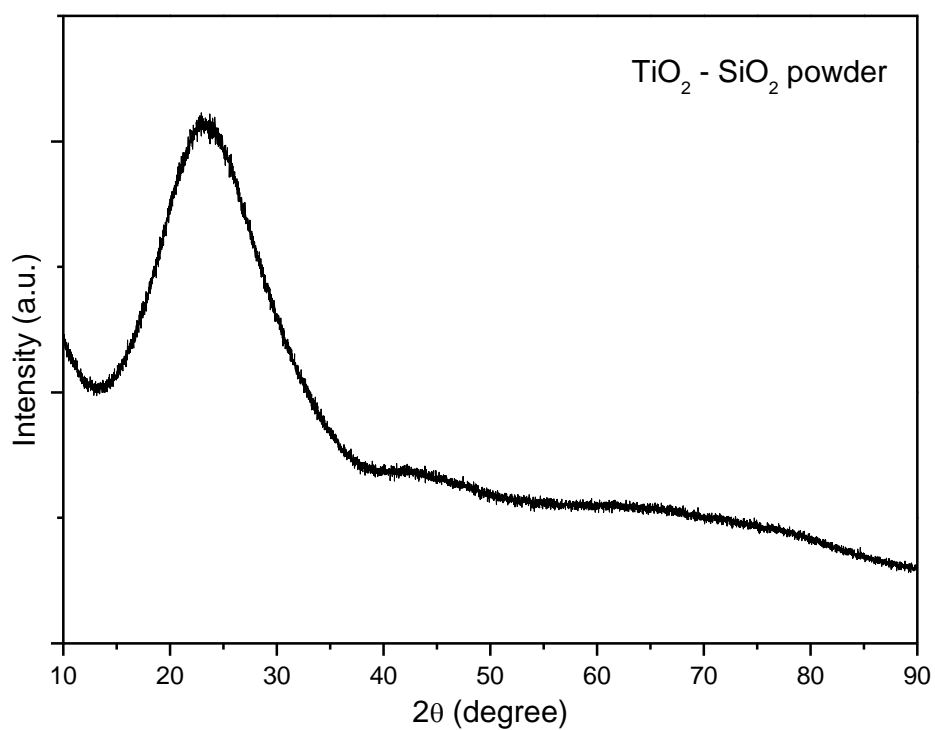


**Figure 5.42:** XRD pattern of  $\text{TiO}_2 - \text{SiO}_2$  film on glass substrate.

## 6. CONCLUSIONS

TiO<sub>2</sub>, Ta<sub>2</sub>O<sub>5</sub>, SiO<sub>2</sub>, their binary and ternary systems are extensively used oxide thin film for optical interference coatings. They are stiff and chemically resistant, transparent in the visible range and have a stability refractive index, and shows excellent mechanical and environmental stability and non-toxicity. Thin film structures find very wide applications in microelectronics, optics, semiconductor multi-layer, superconducting systems, data storage systems, projection display and solar cell.

All films are deposited by sol-gel techniques on the glass substrates. Dense, well adherent and homogenous oxide films were successfully deposited onto the substrates.

Almost every system is affected by external loads even more than one direction. There are main two parameters, which can be adjust, design and material selection. Design is so important because of stress concentration that damages your complete system. Therefore, scientists have to avoid designs causing stress concentration. After the optimum design processes, selecting proper materials is another crucial step. Cost and performance both affect selecting criteria. Individual materials has been investigated for a long times. Their composites systems are often preferred to examine the superior properties depending on the application areas. Nevertheless, the respond of material under specific loads has to be known in any situation because of reliability of the systems.

Stress analysis for thin-film structures can be performed using analytical methods. However, with the development of computing technology, more researchers are using numerical methods. The finite element analysis is a very powerful technique to model thin-film structures and to carry out processing, static, and dynamic analyses. The film materials used often have properties that are quite different from those of bulk materials, and they even vary from component to component. The main purpose

of this thesis was to use analytical solution and finite element method to analyze the ultimate tensile stress in the oxide films ( $\text{TiO}_2$ ,  $\text{Ta}_2\text{O}_5$  and  $\text{SiO}_2$ ) with different compositions. The use of FEM design and analytical solution could reduce the total number of experimental trials, while still maintaining high accuracy of analysis. Later, Obtained results from theoretical calculations were compared to the experimental tests. FEM gave nearly perfect results for all samples. It is obvious that, Ansys could easily apply to analyze bilayer or multilayer materials. Theoretical and experimental results of uncoated glass substrates are matched well to each other. However, there is a reasonable difference between theoretical and experimental results of the deposited films up to 30%. As it is impossible to experience each material individually or in a composite system, also in nano or macro scale, we need computers to analyze and predict responds of materials. Section 5 shows that Ansys gives almost perfect results. Experiments have to be applied on to most promising candidates to save money and time. Beside, repetition of experiments improves success rates, especially on brittle materials like glass.

Traditional recipe of  $\text{TiO}_2$  -  $\text{SiO}_2$  in the literature leads very frustrating results. Şişecam's recipe shows promising results, although the ratio of  $\text{TiO}_2$  to  $\text{SiO}_2$  is 5:95 in volume.  $\text{Ta}_2\text{O}_5$  thin films represent the best results. They demonstrated around 200% improvement for ultimate strength and huge increase in scratch resistance. Adding  $\text{CeO}_2$  nano particles to  $\text{TiO}_2$  –  $\text{SiO}_2$  binary sol gave poor results in terms of the mechanical properties. SWCNT shows some improvement especially on hardness. Very small amount of SWCNT leads 7% improvement on ultimate strength and 100% on hardness. Nevertheless, the positive effects of SWCNT decreases by increasing content.

The mechanical improvement of thin films has not been drawn so much attention like as optical properties. However, thin films showed incredible improvement on both tensile strength and scratch resistance, especially  $\text{Ta}_2\text{O}_5$  ones.  $\text{Ta}_2\text{O}_5$  are nearly transparent and chemically extremely stable with these unique properties, it is valuable coating material for transparent substrates in rough environmental conditions. Many application areas can be suitable like solar cell technology. In addition, it is not toxic, so it can be used in biomedical industry more frequently.

SWCNTs and CeO<sub>2</sub> nanoparticles were not very effective as expected. More studies can be done on solving dispersion problems of CNTs. CNTs are the most amazing materials but extremely toxic as well. Solving toxicity and dispersion problem will make CNTs indispensable material for high tech industries.

Ta<sub>2</sub>O<sub>5</sub> coating is the most hydrophobic surface within the samples. Ternary system of TiO<sub>2</sub>, SiO<sub>2</sub> and Ta<sub>2</sub>O<sub>5</sub> behaves like hydrophilic.

These films demonstrated excellent transparency, characteristic for wide band gap materials.





## REFERENCES

- [1] **L. Eckertova'** (1986). *Physics of Thin Films*, 2nd Ed., Plenum Press, New York and London, pp. 11–16.
- [2] **J. Matsuoka, R. Naruse, H. Nasu, K. Kamiya** (1997). Preparation of gold microcrystal-doped oxide optical coatings through adsorption of tetrachloroaurate ions on gel films, *J. Non-Cryst. Solids* 218 151–155.
- [3] **H. Kozuka, S. Sakka** (1993). Preparation of gold colloid-dispersed silica coating films by the sol–gel method, *Chem. Mater.* 5 222–228.
- [4] **E. Breval, et al.** (1992). Sol–gel prepared Ni–alumina composite materials. Part I. Microstructure and mechanical properties, *J. Mater. Sci.* 27 1464–1468.
- [5] **T. Yazawa, et al.** (1994). Preparation and optical property of monolithic silica gel uniformly dispersed with gold colloid from aqueous solution, *J. Non-Cryst. Solids* 170 105–108.
- [6] **A. Santos, et al.** (1998). Synthesis of granular Fe–Al<sub>2</sub>O<sub>3</sub> by sol–gel method, *J. Magn. Mater.* 177–181 247–248.
- [7] **J.C.S. Wu, C.Y. Yeh** (2001). Sol–gel-derived photosensitive TiO<sub>2</sub> and Cu/TiO<sub>2</sub> using homogeneous hydrolysis technique, *J. Mater. Res.* 16 (2) 615–620.
- [8] **Y.L. Shi, X.G. Zhang, H.L. Li** (2001). Enhanced photoluminescence of Eu, Ag-doped SiO<sub>2</sub> gel based on AAO, *J. Chin. Univ.* 22 (5) 321–323.
- [9] **M. Epifani, et al.** (2000). Sol–gel synthesis and characterization of Ag and Au nanoparticles in SiO<sub>2</sub>, TiO<sub>2</sub> and ZrO<sub>2</sub> thin films, *J. Am. Ceram. Soc.* 83 (10) 2385–2393.
- [10] **William D. Nix** (2005). *Mechanical Properties of Thin Films*, Department of Materials Science and Engineering Stanford University.
- [11] **Maissel LI, Reinhard G.** (1983). *Handbook of thin film technology*. New York: McGraw-Hill.
- [12] **Brinker, C.J.; G.W. Scherer** (1990). *Sol-Gel Science: The Physics and Chemistry of Sol-Gel Processing*. Academic Press. ISBN 0-12-134970-5.
- [13] **Maryanne M. Couinson** (1999). *Structure, chemistry, and applications of sol-gel derived materials*, Department of Chemistry Kansas State University, Manhattan, Kansas
- [14] **Y.X. Chen, W.M. Liu** (2001). Tribological properties of sol–gel ZrO<sub>2</sub> thin films, *Tribology (Chinese)* 21 (4) 274–278.

- [15] **Y.X. Chen, J.F. Zhou, W.M. Liu** (2001). Preparation, characterization and tribological properties of sol–gel TiO<sub>2</sub>–ZrO<sub>2</sub> thin films, *Sci. China, Ser. A* 44 (Suppl.) 381–386.
- [16] **W.G. Zhang, W.M. Liu, B. Li, G.X. Mai** (2002). Characterization and tribological investigation of sol–gel TiO<sub>2</sub> and doped TiO<sub>2</sub> thin films, *J. Am. Ceram. Soc.* 85 1770–1776.
- [17] **J. Binker and G. Scherer** (1989). *Sol-Gel Science*, Academic Press, New York.
- [18] **C. J. Binker, C. J. Binker and G. W. Scherer** (1988). *Ultrastructure Processing of Ceramics, Glasses, and Composites*, pp. 43-49. Wiley, New York.
- [19] **D. Avnir, L. C. Klein, D. Levy, U. Schubert, and A. B. Wojcik** (1998). *The Chemistry of Organic Silicon Compounds*, Vol. 2, Chap. 40, pp. 2317-2362.
- [20] **L. L. Hench and J. K. West** (1990). *Chem. Rev.* 90, 33.
- [21] **C. J. Brinker, A. J. Kurd, P R. Schunk, G C. Frye, and C. S. Ashley** (1992). *Non-Cryst. Solids* 147/148, 424.
- [22] **D. Avnir, S. Braun, O. Lev, and M. Ottolenghi** (1994). *Chem. Mater.* 6, 1605.
- [23] **O. S. Wolfbeis, R. Reisfeld, and L Oehme** (1996). *Structure and Bonding* 85, 51.
- [24] **O. Lev, M. Tsionsky, L. Rabinovich, V. Glezer, S. Sampath, I. Pankratov, and J. Gun** (1995). *Anal Chem.* 67, 22A.
- [25] **M. M. Collinson** (1998). *Mikrochim. Acta* 129, 149.
- [26] **Dirk W. Schubert, Thomas Dunkel** (2003). Spin coating from a molecular point of view: its concentration regimes, influence of molar mass and distribution; *Materials Research Innovations* Vol. 7, p. 314.
- [27] **M.J. Madou** (2002). *Fundamentals of Microfabrication: The Science of Miniaturization*, 2<sup>nd</sup> ed., CRC Press, Boca Raton, FL.
- [28] **B. D. MacCraith, C McDonagh, A. K. Mcevoy, T. Butler, G. O'Keeffe, and V Murphy** (1997). *Sol-Gel Sci. Technol*, 8, 1063.
- [29] **Antonella Macagnano** (n.d.). *New Applications of Nanoheterogeneous Systems* Institute of Atmospheric Pollution Research, National Research Council (IIA-CNR), Rome, Italy.
- [30] **Aegerter MA** (2004). *Menning M. Sol-Gel technologies for glass producers and users*. Boston/Dordrecht/New York/London: Kluwer Academic Publishers.
- [31] **Matsunami N, Hosono H.** (1993). Colloid formation effects on depth profile of implanted Ag in SiO<sub>2</sub> glass. *Appl Phys Lett*, 63:2050–2.
- [32] **Su W, Wei SS, Hu SQ, Tang JX.** (2009). Preparation of TiO<sub>2</sub>/Ag colloids with ultraviolet resistance and antibacterial property using short chain polyethylene glycol. *J Hazard Mater*, 172:716–20.

- [33] **Yao Y, Ohko Y, Sekiguchi Y, Fujishima A, Kubota Y.** (2008). Self-sterilization using silicone catheters coated with Ag and TiO<sub>2</sub> nanocomposite thin film. *J Biomed Mater Res B Appl Biomater*, 85:453–60.
- [34] **Fonseca SM, Barker AL, Ahmed S, Kemp TJ, Unwin PR.** (2003). Direct observation of oxygen depletion and product formation during photocatalysis at a TiO<sub>2</sub> surface using scanning electrochemical microscopy. *Chem Commun (Camb)*, 21:1002–3.
- [35] **Byun HS, Park MH, Lim GT, Yoon SD.** (2011). Physical properties and characterization of biodegradable films using nano-sized TiO<sub>2</sub>/poly(acrylamide-co-methyl methacrylate) composite. *J Nanosci Nanotechnol*, 11: 1701–5.
- [36] **Fujishima M, Takatori H, Tada H.** (2011). Interfacial chemical bonding effect on the photocatalytic activity of TiO<sub>2</sub>-SiO<sub>2</sub> nanocoupling systems. *J Colloid Interface Sci*, 361:628–31.
- [37] **W.H. Wollaston, Philos. Trans. R.** (n.d.). Soc. Lond. 1, 1809, 246.
- [38] **F. Macionczyk, B. Gerold, R. Thull** (2001). *Surf. Coat. Technol.* 142–144, 1084.
- [39] **G.L. Duveneck, M.A. Bopp, M. Ehrat, M. Haiml, U. Keller, M.A. Bader, G. Marowsky, S. Soria** (2001). *Appl. Phys. B-Lasers Opt.* 73, 869.
- [40] **Z. Zou, J. Ye, K. Sayama, H. Arakawa** (2001). *Nature* 414, 625.
- [41] **Y. Nakagawa, M. Yawata, S. Kakio** (2001). *Electron. Commun. Jpn., Part II: Electron.* 84, 46.
- [42] **G.B. Alers, D.J. Werder, Y. Chabal, H.C. Lu, E.P. Gusev, E. Garfunkel, T. Gustafsson, R.S. Urdahl** (1998). *Appl. Phys. Lett.* 73, 1517.
- [43] **Wang, X.; Li, Qunqing; Xie, Jing; Jin, Zhong; Wang, Jinyong; Li, Yan; Jiang, Kaili; Fan, Shoushan** (2009). Fabrication of Ultralong and Electrically Uniform Single-Walled Carbon Nanotubes on Clean Substrates, *Nano Letters* 9 (9): 3137–3141.
- [44] **Kim, K.S.; Cota-Sanchez, German; Kingston, Chris; Imris, M.; Simard, Benoît; Soucy, Gervais** (2007). "Large-scale production of single-wall carbon nanotubes by induction thermal plasma". *Journal of Physics D: Applied Physics* 40: 2375.
- [45] **X. Feng, D.C. Sayle, Z.L. Wang, M.S. Paras, B. Santora, A.C. Sutorik, T.X.T. Sayle, Y. Yang, Y. Ding, X.D. Wang** (2006). Converting ceria polyhedral nanoparticles into single-crystal nanospheres, *Science* 312, 1504–1508.
- [46] **J.P. Nair, E. Wachtel, I. Lubomirsky, J. Fleig, Maier** (2003). Anomalous expansion of CeO<sub>2</sub> nanocrystalline membranes, *J. Adv. Mater.* 15, 2077–2081.
- [47] **P. Jasinski, T. Suzuki, H.U. Anderson** (2003). Nanocrystalline undoped ceria oxygen Sensor, *Sens. Actuators B* 95, 73–77.

- [48] **M. Lunderg, B. Skaerman, F. Cesar, L.R. Wallenberg, Mesoporous** (2002). Thin films of high-surface-area crystalline cerium dioxide, *Microporous Mesoporous Mater.* 54, 97–103.
- [49] **Y. Zhang, R. Si, C. Liao, C. Yan** (2003). Facile alcohol thermal synthesis, size-dependent ultraviolet absorption and enhanced CO conversion activity of ceria nanocrystals, *J. Phys. Chem. B* 107, 10159–10167.
- [50] **Lord MS, Jung M, Teoh WY, Gunawan C, Vassie J, Amal R, et al.** (2012). Cellular uptake and reactive oxygen species modulation of cerium oxide nanoparticles in human monocyte cell line U937. *Biomaterials*, 33:7915e24.
- [51] **Asati A, Santra S, Kaittanis C, Perez JM** (2010). Surface-charge-dependent cell localization and cytotoxicity of cerium oxide nanoparticles. *ACS Nano*, 4:5321e31.
- [52] **Celardo I, De Nicola M, Mandoli C, Pedersen JZ, Traversa E, Ghibelli L** (2011). CeO<sub>2</sub> ions determine redox-dependent anti-apoptotic effect of cerium oxide nanoparticles. *ACS Nano*, 5:4537e49.
- [53] **Pirmohamed T, Dowding JM, Singh S, Wasserman B, Heckert E, Karakoti AS, et al.** (2010). Nanoceria exhibit redox state-dependent catalase mimetic activity. *Chem Commun*, 46:2736e8.
- [54] **Ting SRS, Whitelock JM, Tomic R, Gunawan C, Teoh WY, Amal R, et al.** (2013). Cellular uptake and activity of heparin functionalized cerium oxide nanoparticles in monocytes. *Biomaterials*, 34:4377e86.
- [55] **Schubert D, Dargusch R, Raitano J, Chan SW.** (2006). Cerium and yttrium oxide nanoparticles are neuroprotective. *Biochem Biophys Res Commun*, 342:86e91.
- [56] **Tarnuzzer RW, Colon J, Patil S, Seal S.** (2005). Vacancy engineered ceria nanostructures for protection from radiation-induced cellular damage. *Nano Lett*, 5:2573e7.
- [57] **R.W.G. Wyckoff** (1964). *Crystal Structures*, 2nd ed., Wiley, New York.
- [58] **A.M. Thompson** (1978). *Oxides of the Rare Earths*, Wiley, New York.
- [59] **V.E. Henrich, P.A. Cox** (1994). *The Surface Chemistry of Metal Oxides*, Cambridge University Press, Cambridge, UK.
- [60] **F. Bezati, V. Massardier, J. Balcaen, D. Froelich** (2011). A study on the dispersion, preparation, characterization and photo-degradation of polypropylene traced with rare earth oxides, *Polym. Degrad. Stab.* 96, 51–59.
- [61] **Wredenberg, Fredrik; PL Larsson** (2009). Scratch testing of metals and polymers: Experiments and numeric, *Wear* 266, 1-2.
- [62] **L.I. Malssel, R. Glang,** (1970). *Handbook of Thin Film Technology*, McGraw Hill Book Company, New York.
- [63] **M. Dhanam, P.K. Manoj, Rajeev R. Prabhu, J. Cryst** (2005). *Growth* 280, 425.

- [64] **Dr. H. “Jerry” Qi** (2006). Finite Element Analysis, Colorado University, MCEN 4173/5173.
- [65] **Syed Ali Ashter** (2014). Thermoforming of Single and Multilayer Laminates Plastic Films Technologies, Testing, and Applications, 123–145.
- [66] **E.J. Hearn** (1997). Mechanics of Materials Volume 1, 978-0-7506-3265-2.
- [67] **Julia R. Weertman** (1999). Mechanical Behavior of Nanocrystalline Metals, Northwestern University, Evanston, IL, USA.
- [68] **Gleiter, H.** (1989). Progress in Mats. Sci., 33:223.
- [69] **Nieman, G.W., Weertman, J.R., and Siegel, R.W., J. Mats.** (1991). Res., 6:1012.
- [70] **Sanders, P.G., Weertman, J.R., Barker, J.G., and Siegel, R.W.** (1993). Scripta Met. Mat., 29:91.
- [71] **Ichim I, Li Q, Li W, Swain MV, Kieser J.** (2007). Modelling of fracture behaviour in biomaterials. Biomaterials, 28:1317–26.
- [72] **Culha O, Zor M, Gungor MA, Arman Y, Toparli M.** (2009). Evaluating the bond strength of opaque material on porcelain fused to metal restorations (PFM) alloys by scratch test method. Mater Des, 30:3225–8.
- [73] **Dapeng Zhang, Jianqiu Zhou, Shu Zhang, Lu Wang, Shuhong Dong** (2013). Theoretical analyses and numerical simulations on the mechanical strength of multilayers subjected to ring-on-ring tests.
- [74] **ISO 6872** (2006). Dentistry-ceramic materials. Case Postale, Geneva: International Organization for Standardization.
- [75] **Ritter JE, Jakus K, Batakis A, Bandyopadhyay N.** (1980). Appraisal of biaxial strength testing. J Non-Cryst Solids, 38(39):419–24.
- [76] **Timoshenko S, Woinowsky-Krieger S.** (1959). Theory of Plates and Shells. New York: McGraw-Hill.
- [77] **Vitman FF, Pukh VP.** (1963). A method for determining the strength of sheet glass. Zavod Lab, 29:863–7.
- [78] **Shetty DK, Rosenfield AR, McGuire P, Bansal GK, Duckworth WH.** (1980). Biaxial flexure tests for ceramics. Am Ceram Soc Bull, 59:1193–7.
- [79] **Hsi-Chao Chen, Chen-Yu Huang** (2010). Residual Stress Analysis for Oxide Thin Films with Different Substrate and Temperature by Finite Element Method, Graduate School of Optoelectronics, National Yun-Lin University of Science and Technology, Taiwan 64002, 310.0310, 310.4925 and 310.6870.



## **CURRICULUM VITAE**

**Name Surname: İsmail Hakkı Cengizhan KARBAY**

**Place and Date of Birth: Aydın / 1989**

**Address: İstanbul / TURKEY**

**E-Mail: karbay@itu.edu.tr**

**B.Sc.: Trakya University / Mechanical Engineering**

**M.Sc.: Istanbul Technical University / Nano Science & Nano Engineering**

**Professional Experience and Rewards: Mechanics of thin films and composites, finite element analysis, computer simulations, failure analysis, marketing, basketball, scuba diving.**

**List of Publications and Patents:**



## **PUBLICATIONS/PRESENTATIONS ON THE THESIS**